Development and Validation of the Human Rosette Array for Neural Tube Defect Risk Screening

By

Brady F. Lundin

A dissertation submitted in partial fulfillment of

the requirements for the degree of

Doctor of Philosophy

(Biomedical Engineering)

at the

UNVIERSITY OF WISCONSIN-MADISON

2024

Date of final oral examination: 04/15/2024

The dissertation is approved by the following members of the Final Oral Committee:

Randolph S. Ashton, Associate Professor, Biomedical Engineering
Bermans J. Iskandar, Professor, Neurosurgery
Krishanu Saha, Associate Professor, Biomedical Engineering
Eric V. Shusta, Professor, Chemical and Biological Engineering
John-Paul J. Yu, Assistant Professor, Radiology

Table of Contents

List of Figures

Abstract

Neural tube defects are the second most common congenital malformation and inflict significant morbidity and mortality upon affected patients. The mechanisms by with they form are unclear and traditional methods of studying the nascent central nervous system have significant limitations. Neural organoids have revolutionized how human neurodevelopmental disorders are studied. Yet, their utility for screening complex neural tube defect etiologies and potential prophylactics is limited by a lack of scalable and quantifiable derivation formats. Here, a brief introduction to neural tube formation and an overview of the known causes of neural tube defects is presented. Then a survey of the rapidly developing field of neural organoids is provided. After which, we describe the Rosette Array platform's ability to be used as an off-the-shelf, 96-well plate assay that standardizes incipient forebrain and spinal cord organoid morphogenesis as micropatterned, 3-D, singularly polarized neural rosette tissues. Rosette Arrays are seeded from cryopreserved human pluripotent stem cells, cultured over 6-8 days, and immunostained images can be quantified using artificial intelligence-based software. We demonstrate the platform's suitability for screening genetic and environmental factors known to cause neural tube defect risk. Lastly, the discussion closes by considering the implications of the platform's development and screening results and future research directions regarding understanding and preventing neural tube defect formation.

Acknowledgments

Ten years ago in the summer of 2014, after missing my first three emails, Dr. Randolph Ashton extended me an invitation to interview for a position as an undergraduate researcher. Despite having no prior research experience, Randy, and his senior graduate student Gavin Knight, offered me the exciting opportunity to aid their research focused on creating biomaterials that could one day help us better understand how the spinal cord develops. Over a decade later, I lack the ability to adequately express the immense gratitude I have for their collective teaching, mentorship, professional development, and friendship. Their influence has taken me across the world and allowed me to reach goals my undergraduate self would never have dreamed possible. I am certain that without it, I would not be the scientist, future physician, or person that I am today. It's been one of the greatest pleasures of my professional and academic life to assist them on their journey developing the technology presented here. As I finish my graduate training, I sincerely hope that our greatest collaborations have yet to occur.

Of course, my time in the Ashton Lab would not have been nearly as enjoyable were it not for the wonderful colleagues and friends that made up each day. Nikolai, Frank, Britney, Nisha, Carlos, Jack, Nick, Madeline, and Abi not only provided valuable contributions to the work, but more importantly, made each day something to look forward to. Leaving the daily camaraderie of WID 4th floor behind makes my time ending bittersweet.

Next, I would like to thank each member of my thesis committee, not only for their collective academic insights, but for their induvial contributions to my professional development. Dr. Iskandar, for being an invaluable mentor in both my scientific and clinical lives and giving me the guidance and confidence to pursue my next professional venture. Dr. Saha, for his consistently valuable project insights dating back to my days as an undergraduate BME design student. Dr. Shusta, for the opportunity to spend a month in his lab and differentiate stem cells into something other than neuroectoderm. And Dr. Yu, for his mentorship within the UW MSTP and for inviting me to the neuroradiology reading room.

I would also like to thank the patients and families of Dr. Iskandar's spina bifida clinic for graciously allowing me to observe as part of their healthcare team. Especially, I would like to recognize one young man, and by extension his family, for his commitment to providing a skin sample that will allow for the important progression of this project. His enthusiasm about the donation was instrumental in making it happen. I will think of his passion for sled hockey each time I put my own hockey stick on the ice.

Next, I raise a symbolic toast to the countless friends that have made Madison home since 2012. The many Badger sporting events, dinners, spontaneous celebrations, pond hockey weekends, and hours spent on the terrace and Chasers' patio provided the energy and encouragement to consistently give my best throughout this long training process.

Todd, Susie, Ben and Jacquline, and Eve have been there for me every step of the way, always making sure I find time to relax and enjoy life. I am so thankful I decided to stay near my family to complete my MD/PhD training. I would like to make special mention of my parents' lifelong sacrifices and innate generosity, because of which I was able to spend my formative college summers and in-semester free time focusing on being a student and prospective scientist.

Lastly, I would like to thank Sam for bringing daily joy to my life, no matter the trial of the day. I imagine starting graduate training in the middle of a pandemic, daily trips to the cell culture room for hours, or watching another Match Day pass by was supposed to feel isolating at some point, yet her encouraging presence at the end of each day spared me from such a fate. To do this all while applying, matriculating, and completing her own first two years of medical school truly means the world.

Clearly, lifelong scientific and medical training takes a village, and I am undoubtedly fortunate for the people that make up mine.

Chapter 1 – Introduction

Significance and Background

Neural Tube Defects (NTDs) are the second most common developmental malformation, affecting ~3000 births per year in the United States (US) with an estimated lifetime disease cost of at least $560,000 per person, and an even greater incidence and burden of disease worldwide[1,2]. Defects occur during the first 4 weeks of pregnancy, often before a mother is aware of conception. For cases that do not experience early intrauterine demise or choose therapeutic abortions, children born with NTDs present with a wide spectrum of disability depending on the location and severity of their deficit[2,3]. Patients with the most common clinical NTD, spina bifida, can experience a plethora of lifelong medical problems including, but not limited to, motor impairment, hydrocephalus requiring shunting, neurogenic bladder and bowel, later sexual incontinence, and psychosocial maladjustment[1,4,5].

The neural tube is the developmental origin of the entire central nervous system (CNS) and forms via the process of neurulation (**Figure 1A**)[6,7]. During the processes of convergent extension (CE), neural plate bending/hinging, and fusion, neuroepithelial cells (NECs) of the neural plate proliferate and invaginate upon themselves to form a tube via primary neurulation. The tube is comprised of polarized expression of adherens and tight junction proteins at the apical lumen, and extracellular matrix proteins at the basal surface (**Figure 1B**)[6,8]. Polarized NECs comprising the neural tube exhibit discrete regional phenotypes along the embryo's rostrocaudal (R/C) axis as determined by patterning of differential HOX gene transcription factor expression profiles[9,10] (**Figure 1B**). This diversification of NEC regional identity results in differing R/C closure mechanisms along the length of the developing tube, and later enables development of the myriad CNS tissue types found along the axis.

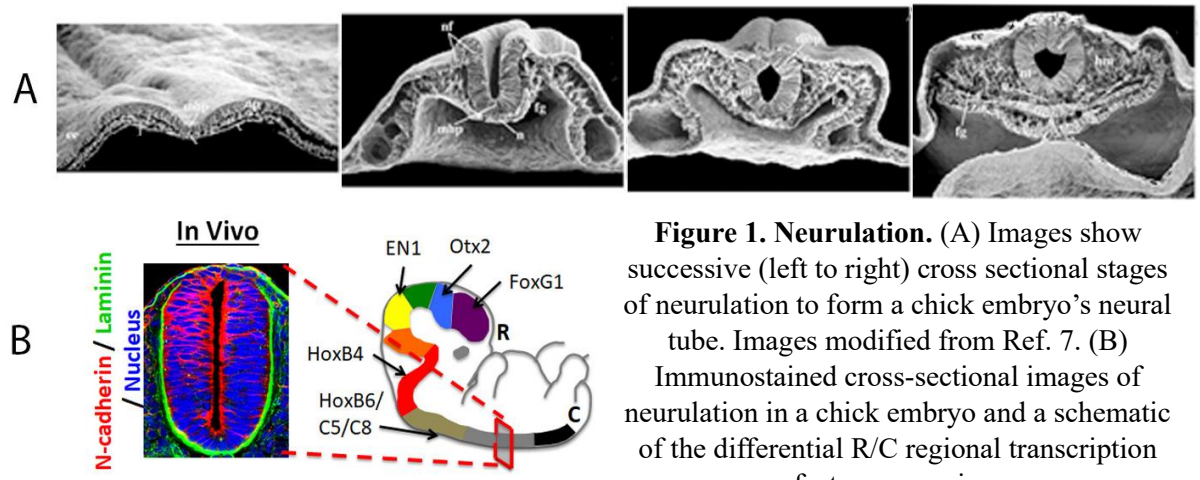

Figure 1. Neurulation. (A) Images show successive (left to right) cross sectional stages of neurulation to form a chick embryo's neural tube. Images modified from Ref. 7. (B) Immunostained cross-sectional images of neurulation in a chick embryo and a schematic of the differential R/C regional transcription factor expression.

After the formation of the neural plate (NP), primary neurulation begins through the process of convergent extension (CE). CE shapes the NP for eventual closure by converging the axial neuroectoderm mediolaterally (ML) and driving anterior-posterior (AP) extension, i.e., narrowing transversely, and elongating rostrocaudally. Early tissue isolation experiments demonstrated that the neuroectoderm undergoes shaping when removed from the surrounding mesoderm and epidermal ectoderm[11].

The polarized cellular movements that are characteristic of CE are known to be driven by the non-canonical WNT/planar cell polarity pathway, and this pathway's disruption is known to contribute to NTDs[12,13]. First identified in the process of *Drosophila* wing hair positioning and since demonstrated as highly conserved in vertebrate CE, Wnt/PCP signaling leads to the core PCP proteins (*Disheveled, Scrib, Frizzled)* demonstrating a highly polarized cellular distribution in both the AP and ML axes. Across species, these polarized expressions appear to be regulated by the phosphorylation of myosin light chain (pMLC)[14,15]. While many animal models have demonstrated NTD development due to disruptions in the PCP, it is difficult to place this only as a failure of CE, as much of the Wnt/PCP signaling cascade is involved in the process of neural

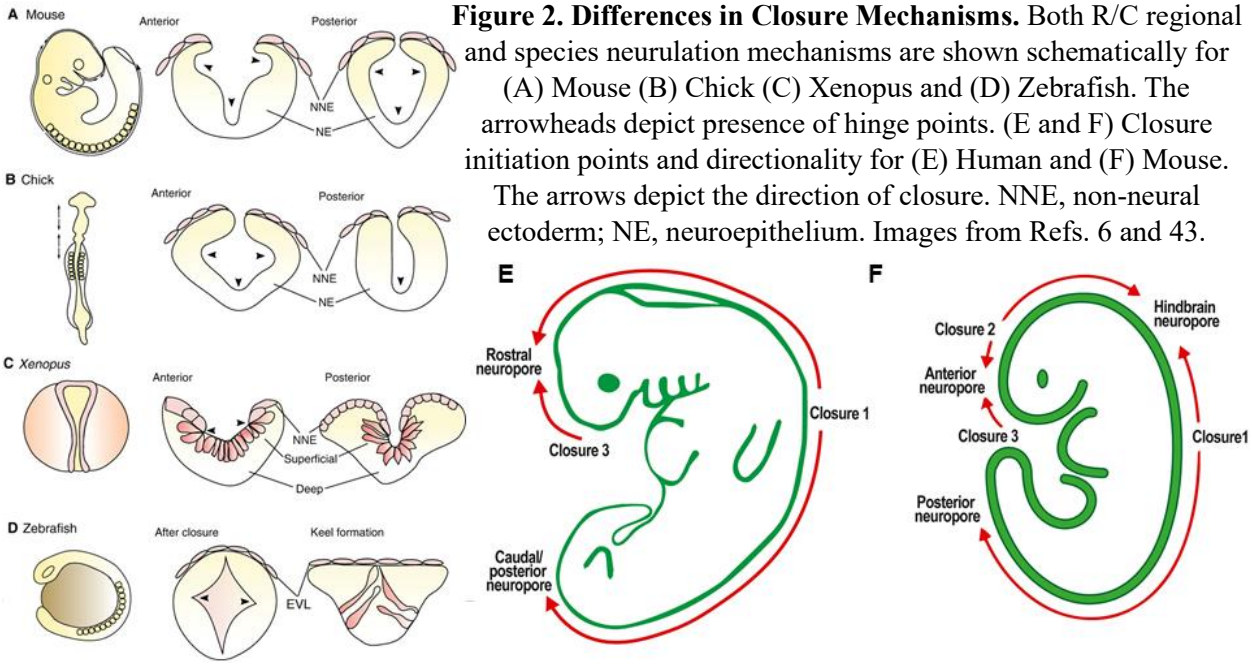

Figure 2. Differences in Closure Mechanisms. Both R/C regional and species neurulation mechanisms are shown schematically for (A) Mouse (B) Chick (C) Xenopus and (D) Zebrafish. The arrowheads depict presence of hinge points. (E and F) Closure initiation points and directionality for (E) Human and (F) Mouse. The arrows depict the direction of closure. NNE, non-neural ectoderm; NE, neuroepithelium. Images from Refs. 6 and 43.

plate bending and fusion, as well as actomyosin/cytoskeletal-driven events. Additionally other pathways such as the Rho/Rock kinase pathways also contribute to both CE and neural plate bending[16,17].

While the tissue undergoes shaping via CE, the lateral margins of the NP begin to bend and elevate, forming neural folds, which eventually fuse at the dorsal midline to form the resultant tube. In the mammalian neural tube, these folds are formed largely by two distinct types of hinge points formation, a singular medial hinge point (MHP), “Mode 1”, and the appearance of a pair of dorsolateral located hinge points (DLHP), “Mode 2”[18,19]. The MHP forms as NP NECs undergo apical to basal interkinetic nuclear migration (IKNM), to localize the nuclei basally, forming a “wedge” shape for the cell, and driving fold elevation[18]. This elevation forms the trough like neural groove, which forms the lumen of the neural tube after closure. After elevation, a BMP signaling gradient drives the formation of the paired DLHPs[20], allowing for convergence of the neural folds, aligning them for closure/fusion.

This provided description is intentionally overly simplified as the bending mechanism is highly regionally, and species, dependent (**Figure 2 A-D**). The contribution of the MHP and DHLPs to fold bending differs along the AP axis of the forming tube[19]. The dynamics of the Shh and BMP signaling systems result in areas of the tube where MHPs or DHLPs do not form and the other compensates[21]. Additionally, it has been demonstrated in mice that an apically located actomyosin ring is necessary for cranial tube closure, however it is not required where IKNM occurs more caudally[16,17], and a failure of ROCK-pathway dependent actin turnover can actually be NTD causative[6]. The exact interplay between actin/pMLC organization and cell cycle-dependent morphogenetic processes remains an outstanding question of the field and likely differs among organisms[6].

Once the two neural folds are brought within proximity due to NP bending, they must finally fuse to create the neural tube. Before fusion occurs in embryos, the neural folds are comprised of both neural and non-neural surface ectoderm[22]. From these cells, finger like projections extend the midline gap and are the first points of attachment of the two separate neural folds[23]. These protrusions include sheet-like lamellipodia and spike-like filopodia. However, it remains a point of debate from which cell type these protrusions originate and where regionally they are required for closure. Again, it appears that differences in species contribute to the uncertainty as well. The protrusions make contact at specific closure initiation sites along the embryo axis, leaving space between the closure sites known as neuropores[24]. Once the initial closure sites have formed, fusion or “zippering” occurs bidirectionally, shortening the neuropores. As the neuropores close, the neural and non-neural ectodermal cells segregate to form two separate layers, the neural comprising the completed tube, and the non-neural forming the surface ectoderm which goes on to form the covering epidermis[25]. It appears this separation

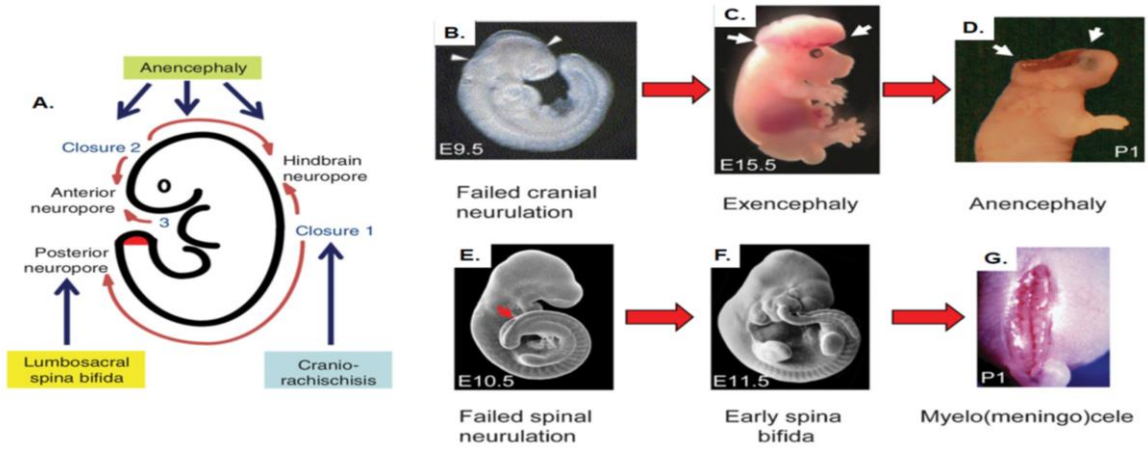

Figure 3. Formation of NTDs. (A) Depicts different rostrocaudal (R/C) neural tube closure locations that lead to NTDs. Progression in mouse embryos: Anencephaly (B-D); Spina bifida aperta (E-G). Images from Ref. 2.

is integrin/ECM mediated and produces force that allows for the actomyosin contraction-led zippering to occur[26]. How the cellular protrusions recognize the proper attachment point to initiate adhesion is not understood, however the Eph/Ephrin system has been implicated in this process[27].

Disruption of the orchestrated neurulation process anywhere along the neuraxis can lead to a regionally distinct NTD[2]. For example, failed closure can occur in the forebrain, midbrain, or hindbrain (anencephaly), the midbrain through spinal cord (craniorachischisis), or the cervical, thoracic, or lumbosacral spinal cord (spina bifida) (**Figure 3**). As gestation proceeds with failed neural tube closure, herniation and exposure of CNS tissues to amniotic fluid causes tissue degeneration, compromised axonal connections, loss of brain and spinal tissue function, leading to the aforementioned clinical sequalae (**Figure 3 B-G**)[1,2]. Despite a vast body of knowledge investigating this crucial neurodevelopmental event throughout hundreds of years, a complete understanding of why defects occur and how to prevent them remains elusive.

For over 40 years it has been recognized that maternal folate status is critical for the prevention of NTDs[28]. The 1998 US government mandate to fortify grain products with folic

acid is estimated to avert ~1,300 NTD-affected pregnancies annually, and this reduction is mirrored by other nations' supplementation efforts, stressing the importance of striving for a folate healthy status in every woman of childbearing age worldwide. Yet, this only accounts for an ~28% reduction in total NTDs, leaving a baseline "folate resistant" NTD rate of every 1 per 2000 pregnancies[1,4,29]. The persistent prevalence of "folate resistant" NTDs suggests additional contributing risk factors. Indeed, exposures to FDA-approved pharmaceuticals[30–32], EPA-approved pesticides[33,34] and abnormal pregnancy conditions (e.g. maternal hyperglycemia[35–37]) have been discovered to increase NTD risk despite proper folate supplementation[2,38]. Additionally, while evidence for a genetic factor is demonstrated in the high recurrence risk for siblings, multi-generational recurrence within families is rare. This suggests that the NTD etiology is not based on a single dominant or recessive mutation or fit a standard Mendelian genetic model, and indeed no single gene has been identified that causes isolated NTDs in humans[2,5]. Therefore, it is widely believed that the continued prevalence of NTDs is a multifactorial interplay between genetic and environmental risk factors[1,2,39,40]. However, the mechanisms by which many of these factors contribute to NTDs remain unknown and are difficult to study using historical models[1].

Existing animal models of NTDs have revealed over 400 candidate genes involved in the process of neural tube closure. However, clinically these candidates are rarely observed to correlate with a human disease phenotype except for mutations affecting the aforementioned planar cell polarity and the folate metabolism pathways[14,40,41]. Furthermore, the vast majority of rodent models, the most widely used model organisms, result exclusively in the rostral defect exencephaly, in contrast to the more clinically common human defect of caudal spina bifida[42]. This discordance likely stems in part from the significant mechanical differences that exist

between interspecies vertebral neurulation[38] (**Figure 2**). For example, one of the most well characterized differences involves the number of closure initiation sites from human to model organism (**Figure 2 E and F**)[43]. Mice and other small rodents exhibit three closure initiation sites at the hindbrain/cervical, forebrain/midbrain, and anterior most boundaries. By comparison, human embryos have only two initiation sites at the most anterior point and the hindbrain/cervical boundary[44]. While the importance of closure initiation sites to the formation of NTDs is debated[40], this gross morphologic difference is certain to stem from critical differences in molecular and cellular mechanisms orchestrated by a human specific genome and its epigenomic regulation[6,29,45].

In addition to key morphogenetic differences between animal and human neural tube closure, rodents rely on highly penetrant gene knockouts that cause loss of function of a gene and have a very small number of inbred strain backgrounds with essentially no genetic variation between individuals[38,40]. This, and the logistics of colony inception and maintenance result in low experimental throughput, and thereby possess both limited efficiency and efficacy when screening for NTD disease factors. Thus, development of a NTD model able to quantitively compare genetic risk contribution within a NTD patient versus isogeneic control background would facilitate elucidation of associated disease mechanisms and screening of environmental factors that contribute to a multifactorial disease etiology. Recently, the development of organoid culture systems derived from human pluripotent stem cells have allowed for the creation of embryo-like structures *in vitro*, with the potential to advance the study of neural tube closure via new models termed “neural tube organoids”[43]. Thus, we set out to bioengineer and validate the first scalable human pluripotent stem cell (hPSC)-derived NTD disease modeling platform suitable for screening clinically relevant genetic and environmental NTD risk factors. The

following details an approximately decade-long effort to conceptualize and translate this platform, a journey for which I am fortunate and grateful to have been able to contribute to during multiple stages of training.

Bibliography

1. Wallingford, J. B., Niswander, L. A., Shaw, G. M. & Finnell, R. H. The Continuing Challenge of Understanding, Preventing, and Treating Neural Tube Defects. *Science* **339**, (2013).

2. Copp, A. J. & Greene, N. D. E. Neural tube defects – disorders of neurulation and related embryonic processes. *Wiley Interdiscip Rev Dev Biol* **2**, 213–227 (2013).

3. Dolk, H., Loane, M. & Garne, E. The Prevalence of Congenital Anomalies in Europe. in *Rare Diseases Epidemiology* (eds. Posada de la Paz, M. & Groft, S. C.) 349–364 (Springer Netherlands, Dordrecht, 2010). doi:10.1007/978-90-481-9485-8_20.

4. Williams, J. *et al.* Updated Estimates of Neural Tube Defects Prevented by Mandatory Folic Acid Fortification — United States, 1995–2011. *MMWR Morb Mortal Wkly Rep* **64**, 1–5 (2015).

5. Iskandar, B. J. & Finnell, R. H. Spina Bifida. *New England Journal of Medicine* **387**, 444–450 (2022).

6. Nikolopoulou, E., Galea, G. L., Rolo, A., Greene, N. D. E. & Copp, A. J. Neural tube closure: cellular, molecular and biomechanical mechanisms. *Development* **144**, 552–566 (2017).

7. Colas, J.-F. & Schoenwolf, G. C. Towards a cellular and molecular understanding of neurulation. *Developmental Dynamics* **221**, 117–145 (2001).

8. Dady, A., Blavet, C. & Duband, J.-L. Timing and kinetics of E- to N-cadherin switch during neurulation in the avian embryo. *Developmental Dynamics* **241**, 1333–1349 (2012).

9. Lippmann, E. S. *et al.* Deterministic HOX Patterning in Human Pluripotent Stem Cell-Derived Neuroectoderm. *Stem Cell Reports* **4**, 632–644 (2015).

10. Cutts, J., Brookhouser, N. & Brafman, D. A. Generation of Regionally Specific Neural Progenitor Cells (NPCs) and Neurons from Human Pluripotent Stem Cells (hPSCs). in *Stem Cell Heterogeneity: Methods and Protocols* (ed. Turksen, K.) 121–144 (Springer, New York, NY, 2016). doi:10.1007/7651_2016_357.

11. Schoenwolf, G. C. & Alvarez, I. S. Roles of neuroepithelial cell rearrangement and division in shaping of the avian neural plate. *Development* **106**, 427–439 (1989).

12. Wallingford, J. B. & Harland, R. M. Xenopus Dishevelled signaling regulates both neural and mesodermal convergent extension: parallel forces elongating the body axis. *Development* **128**, 2581–2592 (2001).

13. Juriloff, D. M. & Harris, M. J. A consideration of the evidence that genetic defects in planar cell polarity contribute to the etiology of human neural tube defects. *Birth Defects Research Part A: Clinical and Molecular Teratology* **94**, 824–840 (2012).

14. Nishimura, T., Honda, H. & Takeichi, M. Planar Cell Polarity Links Axes of Spatial Dynamics in Neural-Tube Closure. *Cell* **149**, 1084–1097 (2012).

15. Rolo, A., Skoglund, P. & Keller, R. Morphogenetic movements driving neural tube closure in Xenopus require myosin IIB. *Developmental Biology* **327**, 327–338 (2009).

16. Butler, M. B. *et al.* Rho kinase-dependent apical constriction counteracts M-phase apical expansion to enable mouse neural tube closure. *J Cell Sci* **132**, (2019).

17. Escuin, S. *et al.* Rho-kinase-dependent actin turnover and actomyosin disassembly are necessary for mouse spinal neural tube closure. *J Cell Sci* **128**, 2468–2481 (2015).

18. McShane, S. G. *et al.* Cellular basis of neuroepithelial bending during mouse spinal neural tube closure. *Dev Biol* **404**, 113–124 (2015).

19. Shum, AlisaS. W. & Copp, AndrewJ. Regional differences in morphogenesis of the neuroepithelium suggest multiple mechanisms of spinal neurulation in the mouse. *Anat Embryol* **194**, (1996).

20. Ybot-Gonzalez, P. *et al.* Neural plate morphogenesis during mouse neurulation is regulated by antagonism of Bmp signalling. *Development* **134**, 3203–3211 (2007).

21. Ybot-Gonzalez, P., Cogram, P., Gerrelli, D. & Copp, A. J. Sonic hedgehog and the molecular regulation of mouse neural tube closure. *Development* **129**, 2507–2517 (2002).

22. Ray, H. J. & Niswander, L. A. Dynamic behaviors of the non-neural ectoderm during mammalian cranial neural tube closure. *Dev Biol* **416**, 279–285 (2016).

23. Massarwa, R. & Niswander, L. In toto live imaging of mouse morphogenesis and new insights into neural tube closure. *Development* **140**, 226–236 (2013).

24. Greene, N. D. E. & Copp, A. J. Neural Tube Defects. *Annu. Rev. Neurosci.* **37**, 221–242 (2014).

25. Pai, Y.-J. *et al.* Epithelial fusion during neural tube morphogenesis. *Birth Defects Research Part A: Clinical and Molecular Teratology* **94**, 817–823 (2012).

26. Molè, M. A. *et al.* Integrin-Mediated Focal Anchorage Drives Epithelial Zippering during Mouse Neural Tube Closure. *Developmental Cell* **52**, 321-334.e6 (2020).

27. Turmaine, M., Abdul-Aziz, N. M., Greene, N. D. E. & Copp, A. J. EphrinA-EphA receptor interactions in mouse spinal neurulation: implications for neural fold fusion. *Int. J. Dev. Biol.* **53**, 559–568 (2004).

28. Smithells, R. W., Sheppard, S. & Schorah, C. J. Vitamin deficiencies and neural tube defects. *Arch Dis Child* **51**, 944–950 (1976).

29. Wolujewicz, P., Steele, J. W., Kaltschmidt, J. A., Finnell, R. H. & Ross, M. E. Unraveling the complex genetics of neural tube defects: From biological models to human genomics and back. *genesis* **59**, e23459 (2021).

30. Lammer, E. J., Sever, L. E. & Oakley, G. P. Valproic acid. *Teratology* **35**, 465–473 (1987).

31. Warkany, J. Aminopterin and methotrexate: Folic acid deficiency. *Teratology* **17**, 353–357 (1978).

32. Spina Bifida in Infants of Women Treated with Carbamazepine during Pregnancy | NEJM. https://www.nejm.org/doi/full/10.1056/NEJM199103073241006.

33. Missmer Stacey A. *et al.* Exposure to Fumonisins and the Occurrence of Neural Tube Defects along the Texas–Mexico Border. *Environmental Health Perspectives* **114**, 237–241 (2006).

34. Rull, R. P., Ritz, B. & Shaw, G. M. Neural Tube Defects and Maternal Residential Proximity to Agricultural Pesticide Applications. *American Journal of Epidemiology* **163**, 743–753 (2006).

35. Sheffield, J. S., Butler-Koster, E. L., Casey, B. M., McIntire, D. D. & Leveno, K. J. Maternal diabetes mellitus and infant malformations. *Obstetrics & Gynecology* **100**, 925–930 (2002).

36. McLeod, L. & Ray, J. G. Prevention and Detection of Diabetic Embryopathy. *PHG* **5**, 33–39 (2002).

37. Shaw, G. M. *et al.* Neural tube defects associated with maternal periconceptional dietary intake of simple sugars and glycemic index. *Am. J. Clin. Nutr.* **78**, 972–978 (2003).

38. Mohd-Zin, S. W., Marwan, A. I., Abou Chaar, M. K., Ahmad-Annuar, A. & Abdul-Aziz, N. M. Spina Bifida: Pathogenesis, Mechanisms, and Genes in Mice and Humans. *Scientifica* **2017**, 1–29 (2017).

39. Chen, Z. *et al.* Threshold for neural tube defect risk by accumulated singleton loss-of-function variants. *Cell Research* **28**, 1039–1041 (2018).

40. Juriloff, D. M. & Harris, M. J. Insights into the Etiology of Mammalian Neural Tube Closure Defects from Developmental, Genetic and Evolutionary Studies. *Journal of Developmental Biology* **6**, 22 (2018).

41. Molloy, A. M., Brody, L. C., Mills, J. L., Scott, J. M. & Kirke, P. N. The search for genetic polymorphisms in the homocysteine/folate pathway that contribute to the etiology of human neural tube defects. *Birth Defects Research Part A: Clinical and Molecular Teratology* **85**, 285–294 (2009).

42. Harris, M. J. & Juriloff, D. M. An update to the list of mouse mutants with neural tube closure defects and advances toward a complete genetic perspective of neural tube closure. *Birth Defects Research Part A: Clinical and Molecular Teratology* **88**, 653–669 (2010).

43. Y, W., S, P., Rh, F. & Y, Z. Organoids as a new model system to study neural tube defects. *FASEB journal : official publication of the Federation of American Societies for Experimental Biology* **35**, (2021).

44. O'Rahilly, R. & Müller, F. The two sites of fusion of the neural folds and the two neuropores in the human embryo. *Teratology* **65**, 162–170 (2002).

45. V, R. P., Finnell, R. H., Ross, M. E., Alarcón, P. & Suazo, J. Neural tube defects and epigenetics: role of histone post-translational histone modifications. *Epigenomics* (2024) doi:10.2217/epi-2023-0357.

Chapter 2 – The Human Rosette Array as a Model for Studying Early Neural Development

Introduction

Since the isolation of human embryonic stem cells in 1998[1], the field of stem cell biology has promised to bring revolutionary changes to our understanding and treatment of human health and disease. While the initial excitement about the potential of stem cells to create transplantable tissues for off the shelf use has been tempered, the field has pivoted to developing *in vitro* models of use to developmental biology and disease modeling alike. These models, better known as organoids, are 3D cell aggregates generated from pluripotent stem cells that self-organize to recognizable tissue constructs through the use of engineered extracellular scaffolding and culture cues[2,3]. By utilizing human embryonic or induced pluripotent stem cells, these models can study critical developmental events within a human genetic background. Through the combination of neural directed differentiation[4,5] and the self-assembly inherent to organoids, the field has begun to generate models *in vitro* with features representative of the developing human nervous system[6–11]. By studying these formations in a human context, the field has begun to refine the vast knowledge of development and maldevelopment gained from animal models.

While organoids representative of multiple organ systems throughout the body have been produced for over a decade, the ability to generate neural tube organoids is a technique still early in its development curve[12]. This has resulted in an assortment of culture methods that produce a variety of neural tube-like structures. The first such structure, published in 2014, utilized mouse embryonic stem cells in Matrigel to create D/V patternable neuroepithelial cyst like structures with a polarized central lumen[13]. In 2016, hPSCs were similarly encapsulated in Matrigel and exposed to a microfluidic device to create a D/V patterned spinal-like organoid[14]. Additionally, hPSCs have been grown in 3D suspension to create similarly patterned structures[15,16]. These

patterned organoids are generated by introducing Shh and BMP activity to NECs that is present during neurulation. More recently, groups have attempted to grow or extend these cystic structures caudally by exposing rostral identity structures to WNT gradients at varying time points in an effort to turn on the more caudally expressed Hox transcription factors[17–19].

The central technology utilized to create such models of the developing CNS stems from the innate attributes of human PSC-derived NECs, a.k.a. apical radial glial cells, that spontaneously form polarized neural rosettes/neuroepithelium in 2-and 3-D culture. These neural rosettes give rise to extensive levels of human brain[6,10,19–21] and spinal morphogenesis[15], and are the morphogenetic centers of neural organoids[21,22]. Once fully formed, rosettes recapitulate the cytoarchitecture and function of a transverse section of the developing neural tube (**Figures 1 and 4**) and are widely accepted as relevant models of early neural tube development[12,23]. In standard neural differentiation protocols, rosettes emerge in an uncontrolled manner, producing organoids with variable rosette number, size, and shape. This strays from *in vivo* development where the neural tube emerges from the planar neuroectodermal plate and forms a singular lumen. This disparity causes a breakdown in reproducibility of organoid structure.

Given their potential utility for investigating early human neural development, many groups, including us, have recently bioengineered models that utilize the self-organization properties of rosettes, while attempting to control the spontaneous and uncontrolled manner in which rosettes form in standard monolayer or cell-aggregate protocols[19,24–28]. Specifically, in our 2018 publication we integrated micropatterned culture substrates with regionally-defined NEC derivation protocols[29,30]. This enables enforcement of a prescribed 2-D monolayer morphology, which reproducibly instructs singular rosette emergence upon morphing into a 3-D tissue for

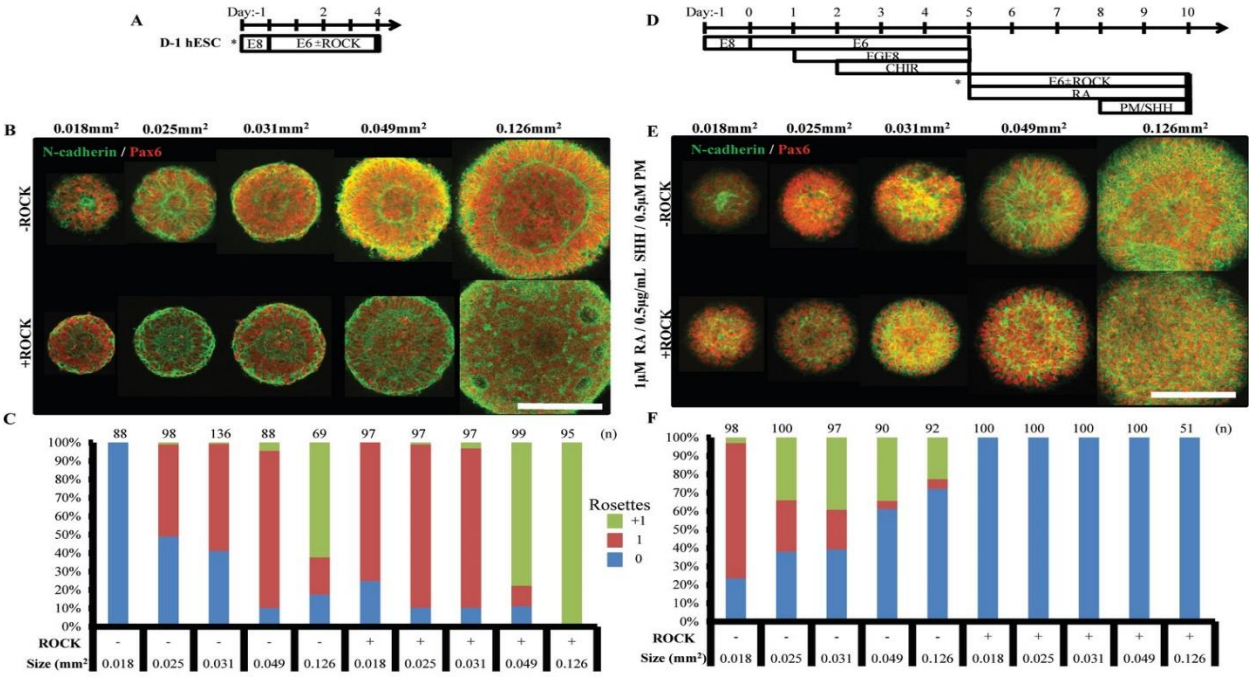

Figure 4. Controlled emergence of single neural rosettes with geometric confinement. (**A**) Schematic for derivation of micropatterned forebrain neuroepithelial tissues; subculture/seeding onto micropatterned substrates indicated by (*). (**B**) Representative images of neural rosette emergence in micropatterned, hESC-derived forebrain neuroepithelial tissues of various areas with and without ROCK inhibitor. (**C**) Quantification of polarization foci/rosettes per forebrain tissue with the number of tissues analyzed per condition above each bar. (**D**) Schematic for derivation of micropatterned spinal neuroepithelial tissues; sub-culture/seeding onto micropatterned substrates indicated by (*). (**E**) Representative images of neural rosette emergence in micropatterned, hESC-derived spinal cord neuroepithelial tissues of various areas with and without ROCK inhibitor. (**F**) Quantification of polarization foci/neural rosettes per spinal tissue with the number of tissue (technical replicates) analyzed per condition above each bar. Scale bars are (**B, F**) 200 μm.

both forebrain and cervical spinal identifying tissues (**Fig. 4 A,D**)[24]. Interestingly, in this early proof of concept, we had identified that the two disparate CNS regions required different culture and geometric confinement conditions to achieve acceptable single rosette emergence and demonstrated differing sensitivity to inhibition of the Rho/Rock cytoskeletal pathway (**Fig. 4 B, C and E, F**). This eluded to the importance of considering the full CNS neuraxis for an effective model of neural tube development, especially given the diverse regional disease presentation within human patients[31]. Overall, this work enabled the ability to derive microarrays of nascent neural organoids with discrete R/C regionalization, reproducible singular rosette structure, and in

an adherent culture format that would allow for future scaling-up to higher throughput, permitting quantitative high throughput screening (qHTS) of early human CNS morphogenesis.

As an analogue to neural tube emergence, defects in neural rosette formation or perturbed behavior of its constituent cells can be predictive of factors that cause congenital NTDs[26,32,33], childhood-onset Autism Spectrum Disorders[22,34,35], Schizophrenia[36], and even adult-onset Huntington's disease[28] and frontotemporal dementia (FTD)/amyotrophic lateral sclerosis (ALS)[37]. Thus, since neural rosette formation requires 'normal' hPSC viability, proliferation, neural differentiation, and NEC physiology, *in vitro* neural rosette formation could be a predictive tool for broadly assessing risk factors for a variety of NDDs including NTDs, as well as general developmental neurotoxicity (DNT)[23]. Regarding NTDs specifically, several groups have published the use of *in vitro* neural rosette formation assays to screen for environmental and genetic risk factors. However, these assays have significant limitations. First, rosette emergence was not standardized in space and time decreasing the assays' sensitivity[32,33,38]. Second, rosette emergence was only assessed in forebrain NEC or neural organoid cultures, whereas NTDs can occur at any point along the neural tubes' R/C axis[26,27,32,33]. In fact, NTDs of the lower spinal cord, i.e., myelomeningocele/spina bifida, are the predominant human clinical scenario[39]. Third, none of the prior neural rosette assays were conducted using direct seeding of cryopreserved cells, which is required to enable the type of scalable, 'off-the-shelf' qHTS necessary to effectively investigate multifactorial NTD risk.

Throughout the body of this work, we present development and validation of a hPSC-derived Rosette Array platform for scalable, off-the-shelf, qHTS of factors known to cause NTD risk. In this chapter, reproducible derivation of forebrain (FB) and cervical spinal cord (SC) Rosette Arrays from direct seeding of cryopreserved hPSCs or neuromesodermal progenitors[30,40]

(NMPs), respectively, was demonstrated. Additionally, the Rosette Array platform's capability to detect a risk associated with pharmaceuticals and agrochemicals known to cause DNT/NTDs was shown. These studies revealed differential responses between forebrain and spinal Rosette Arrays to a well-known NTD-causing teratogen, further supporting the importance of including region-specific assays for more comprehensive coverage of CNS morphogenesis. The majority of these findings can be found in this submitted manuscript (**Brady F. Lundin** et al. RosetteArray® Platform for Quantitative High-Throughput Screening of Human Neurodevelopmental Risk. bioRxiv 2024.04.01.587605 (2024) doi:10.1101/2024.04.01.587605).

Experimental Methods

Experimental Contribution

Most experiments conducted in Chapter Two were completed at the beginning of my graduate training, including during 2020/the beginning of the Covid-19 pandemic. They entail experiments led by Gavin Knight (G.T.K.) during his efforts to validate and commercialize the Rosette Array for broad toxicology screening. As a nascent graduate student with a strong understanding of the project due to my 3+ years as an undergraduate researcher under G.T.K., I was able to significantly contribute to the data presented via experimental strategy/design, substrate fabrication, characterization, data analysis, and data curation and interpretation.

Culture Substrate Fabrication

12-well Rosette Array culture substrates were generated in accordance with our previously published protocol[24]. In brief, Polydimethylsiloxane (PDMS) stamps featuring rectangular arrays of circular recessions with 250 or 150 μm diameters were used to transfer and establish a self-assembled monolayer (SAM) of 2mM ω-mercaptoundecyl bromoizobutyrate onto gold-coated

No. 1 glass coverslips. Poly(ethylene) glycol methyl ether methacrylate (PEGMEMA) brushes were grafted from these SAMs using sodium ascorbate-initiated atom transfer radical polymerization (ATRP) under inert gas for 16 hours at room temperature. Trace copper ions and residual organic solvents were removed through subsequent washes with 70% ethanol. 96-well RosetteArray plates were obtained from Neurosetta LLC.

Cell Culture

WA09 (H9, XX) hESC were supplied by the WiCell Research Institute. WA09 hESCs were maintained at 37°C in 5% CO2 in E8 medium under feeder-free conditions on Matrigel (WiCell)-coated 6-well plates (Corning). For maintenance and expansion, the cells were subcultured in Versene every 5 days at a 1:12 ratio following ~85% confluency. For cell line authentication, cell lines were submitted to WiCell for karyotyping and mycoplasma testing and results returned validated.

NMP Derivation

WA09 hESCs were differentiated into cervical spinal NMPs as previously described[30,40] utilizing CHIR99021 and FGF8b. Briefly, hESCs were seeded at a density of 1.5×10^5 cells/cm^2 in E8 medium with 10 μM ROCK inhibitor for 24 hours. The medium was replaced with E6 medium on day 0 and then changed to E6 supplemented with FGF8b (200 ng/ml) 24 hours later (day 1). On day 2, cells were subcultured at a 2:3 ratio by washing once with PBS, incubating in Accutase for ~2 minutes, and removing them from the surface with gentle pipetting. After centrifugation, cells were gently resuspended in NMP medium, i.e., E6 medium with FGF8b (200 ng/ml) and 3 μM CHIR99021, containing 10 μM Y27632 and seeded on Matrigel-coated plates. This initiates *HOX* colinear and combinatorial expression and is referred to as ‘Hox0’, with 0 representing the hours of CHIR exposure. NMP medium was replenished on day 4

(Hox48). On day 5 (Hox72), cervical spinal cells were collected for cryopreservation (see next section).

Cryopreservation and Thaw of hESC and NMPs

Confluent monolayers of WA09 hESCs in 6-well plates were prepared for cryopreservation through enzymatic dissociation in Accutase (ThermoFisher) and resuspend at ~6,000,000 cells/mL in E8 medium with 10 μM ROCK inhibitor Y-27632 and 10% DMSO. WA09-derived NMPs were similarly dissociated in Accutase and resuspended in E6 medium at ~6,000,000 cells/mL with 10 μM ROCK inhibitor and 10% DMSO. Cryopreservation was performed in Cryovials (Wheaton, Ref#: W985922) at 1mL/vial using a Thermo Scientific CryoMed Controlled-Rate Freezer (7450) set to lower temperature at the following rates; -10°C/min to 4°C, -1°C/min to -60°C, and -10°C/min to -100°C. Cryopreserved vials of cells were placed in liquid nitrogen dewars for extended storage. Cells were thawed at 37°C for 3-5 mins and resuspended in E8 medium with 10 μM ROCK inhibitor for hESC seeding or E6 medium with 10 μM ROCK inhibitor and 1 μM RA for NMP seeding.

Forebrain and Spinal Cord Rosette Array Derivation

FB Rosette Array derivation was initiated by thawing and seeding cryopreserved hESCs at ~200,000 cells/cm^2 onto Matrigel-coated micropatterned arrays with 250 μm diameter circular regions in E8 medium with 10 μM ROCK inhibitor Y-27632. After 1 day, they were cultured in E6 medium for 5 subsequent days using daily 50% media changes. SC Rosette Array derivation was initiated by thawing and seeding cryopreserved hNMPs[40] at ~150,000 cells/cm^2 onto Matrigel-coated micropatterned arrays with 150 μm diameter circular regions in E6 medium, 10 μM ROCK inhibitor Y-27632, and 1 μM Retinoic Acid. After 1 day, they were cultured in E6 medium with 1 μM RA for 5 subsequent days using daily 50% media changes. All culture was

performed in tissue culture polystyrene plates (Corning) in medium supplemented with Penicillin/Streptomycin (ThermoFisher). Standard derivation experiments required E6 medium supplementation with DMSO (Sigma-Aldrich) at 0.01% and 0.1% v/v.

Dose-Response Developmental Neurotoxicity Testing

All cell culture was performed as initially described. Use of the culture platform for DNT screen validation involved supplementation of the culture medium with the compound of interest upon removal of ROCK inhibitor after 1 day of seeding. Chemical compounds stocks were solubilized in DMSO or water and prepared from dry stock fresh for each experiment. Dose-response medium formulations were prepared through serial dilutions in culture medium. Compound concentrations were doubled to account for 50% medium changes. Compounds solubilized in DMSO were controlled to medium conditions containing DMSO supplementation matching the highest tested concentration of DMSO in the treatment groups.

Immunocytochemistry

On the last day of culture, Rosette Arrays were fixed in 4% paraformaldehyde (PFA) in PBS for ~15 minutes. Micropatterned tissues were permeabilized and blocked with 0.1% Triton-X and 5% Donkey serum in PBS (PBS-DT) for 1 hour at room temperature. Primary antibodies listed in the Key Resource Table were incubated on the substrates at 4°C overnight and at a 1:200 dilution in PBS-DT. This was followed by 3 x 20-minute washes with PBS-DT. Next, secondary antibodies listed in Key Resources Table were incubated on the substrates at 4°C overnight and at a 1:500 dilution in PBS-DT. This was followed by 2 x 20-minute washes with PBS-DT, and cell nuclei were stained with DAPI for 10 minutes in the last PBS wash.

Image Acquisition

A Nikon AR-1 Scanning Confocal Microscope with an HD upgrade, Nikon DUG with GaAsP detectors, and a JOBS module software upgrade was used to acquire all fluorescent images. The JOBS module enables semi-automated image acquisitions. In each well, a 10x image was used to randomly selected tissues from the array. High definition, resonance or Galvano scanning image acquisition was performed using a 10, 20, or 60X objective (Nikon) at 512x512 (resonance) or 4096 x 4096 (Galvano) pixels to create Z-stacks with 5-7 image planes at 1.5 µm Z-axis spacing.

Image Analysis of Tissue Viability and Neural Induction

Image segmentation (CellProfiler, Harvard) was used to quantify the number of $DAPI^+$ and $Pax6^+$ cells per vertical image plane for each rosette. To minimize double counting of cells between vertical planes, a single, middle image plane was used to generate a relative number of cells (# of $DAPI^+$ cells) per tissue and $\%Pax6^+$ (# of $Pax6^+$ cells / # of $DAPI^+$ cells).

Manual Characterization of Neural Rosette Emergence and Morphology

Rosette emergence was quantified through manual image analysis. For each of the tissues randomly imaged per array, a binary determination of singular rosette or failed single rosette emergence (i.e., no rosette or 2+ polarization foci present) was made. Neural rosettes in micropatterned tissues were identified by the presence of a coherent N-cadherin ring structure. Percent neural rosette emergence was calculated as # singular rosette/tissues per array. In single rosette tissue, rosette morphological characteristics were measured by outlining the boundary of the N-cadherin ring.

Non-linear Regression of Dose-Response

GraphPad Prism was used to calculate the parameters associated with the Logistic Regression Model, plot sigmoidal dose-response curves, and analyze curve-fit for the different parameters, inspection of the 95% CIs, and R^2 quantification.

Statistical Analysis

GraphPad Prism (V10.2.1) was used for all statistical analysis. Error bars represent mean ± SD; * for $p<0.05$, ** for $p<0.01$, *** for $p<0.001$, **** for $p<0.0001$. Neural rosette emergence for single dose experiments were analyzed with t-tests and all other metrics were analyzed with One-way ANOVAs. Non-linear regression was performed to generate three (Hill Slope =1) or four (Hill Slope not restrained) parameter dose-response curves depending on whether data points were present at the curve's inflection point. Comparison of dose-response curves for different metrics analyzing the same compound were compared using a hypothetical dose-response curve for all metrics. The explanation of "n" and the number of technical or biological replicates completed per experiment, as well as tests done to determine if data met assumptions of statistical approaches, can be found in the figure legends and text.

Results and Interpretation

Validation of an 'off-the-shelf" Rosette Array assay.

Previously, we demonstrated that seeding hESCs or cervical spinal NMP progeny from culture onto micropatterned substrates could be used to generate FB and cervical SC Rosette Arrays (**Figure 4**)[24]. However, for scalable applications, an off-the-shelf protocol that uses direct seeding of cryopreserved cells is required to avoid errors caused by either genetic drift during long-term cell culture[41] and/or differences in hPSC culturing or NMP derivation between experiments. Thus, we cryo-preserved banks of early passage number WA09 hESCs and cervical spinal NMP progeny and assessed whether their direct seeding onto micropatterned substrates could also generate FB and SC Rosette Arrays in a 12-well format (**Figure 5A, B**). After 24-hrs post seeding in E8 media with 10 μm Rock inhibitor (R), prospective FB and SC Rosette Arrays were cultured for an additional 5 days in E6 media without[29] or with retinoic acid (RA)[30,40], respectively, to permit differentiation into $Pax6^+$/N-$cadherin^+$ NECs with subsequent rosette emergence (**Figure 5C**). As previously optimized[24], FB and SC Rosette Arrays were derived using micropatterned culture substrates presenting an array of 250 μm and 150 μm diameter circles, respectively, to preferentially induce singular rosette emergence with regionally distinct tissue morphologies (**Figure 5D**). Post fixation and immunostaining, confocal Z-stacks of arrayed rosette tissues were collected and assessed for the number of $DAPI^+$ cells and the percentage of $Pax6^+$ NECs in the stack's middle slice using CellProfiler as previously described[24]. The percentage of rosette tissues displaying a singularly polarized structure was quantified manually. Retrospective analysis of FB Rosette Array data was used to determine that quantification of ~40-50 rosette tissues per array is sufficient to estimate accurate and precise results for the entire array (**Figure 6A-C**). Using this threshold, it was determined that FB and

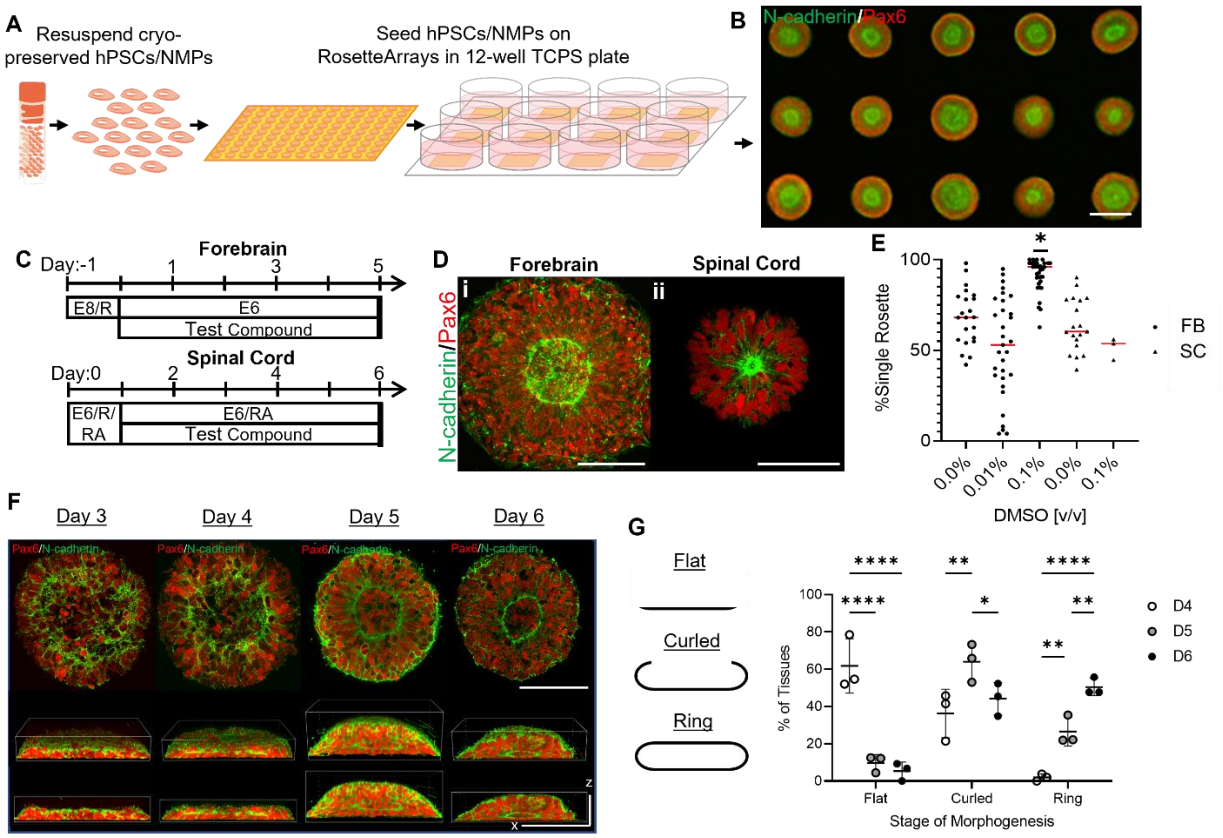

Figure 5. FB and SC Rosette Arrays derived from cryopreserved cell banks. (A) Schematic of 12-well plate format used for direct seeding of cryopreserved hPSCs and cervical spinal NMPs onto micropatterned substrates. (B) Image of resultant immunostained FB Rosette Array showing singularly polarized (N-cadherin+) neural rosette formation. (C) Culture schema for FB and SC RosetteArrays derivation with (D) images showing distinct FB (i) and SC (ii) rosette tissue morphologies. (E) Dot plot of Rosette Array derivation in E6 media supplemented with up to 0.1% v/v DMSO. Each data point is the average of a single experiment (n=50 tissues per well). (F) Time course images of micropatterned rosette tissue morphogenesis at Day (D) 3-6 of FB Rosette Array derivation. Scale bars: x = 125 µm; z = 45 µm. (G) Plot tracking polarized N-cadherin ring's profile (xz-plane) shape, i.e., 'Flat' vs. 'Curled' vs. 'Ring', to document 2- to 3-D rosette tissue morphogenesis. Each data point is the average of a single experiment, n = 40 tissues per well. Scale bars are (b) 250 and (d)100 µm. 1-way ANOVA with Tukey-Kramer post-hoc analysis; *p ≤ 0.05, **p ≤ 0.01, *** p ≤0.001, **** p ≤0.0001.

SC Rosette Arrays derived using direct seeding of cryopreserved cells and culture in E8/R plus E6 or E6/RA media yielded single neural rosette efficiencies of 68.35 ± 15.35% and 63.89 ± 14.62%, respectively (**Figure 6E**). Both values are lower than the 80-85% and 73.5% efficiencies observed previously for FB and SC Rosette Arrays, respectively[24].

While concerned about the decrease in singular rosette efficiency, we continued exploring the platform's utility for chemical screening by assessing its performance in media supplemented

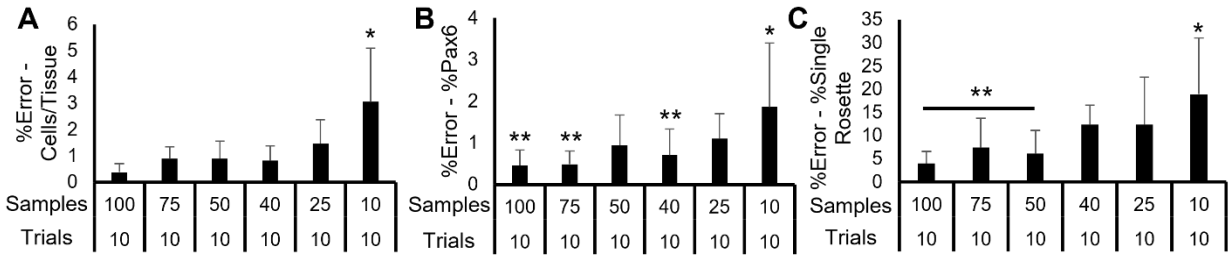

Figure 6. Analysis of required Rosette Array tissue sample size. Sampling different numbers of randomly selected tissues from a FB Rosette Array image dataset to determine %error when calculating (A) cell viability, (B) neural induction, and (C) single rosette emergence. Error was calculated from 10 separate trials per sample number; stats conducted using a One-way ANOVA with Tukey-Kramer post-hoc analysis, * $p \leq 0.05$, ** $p \leq 0.01$.

with dimethyl sulfoxide (DMSO), a common chemical library solvent for both polar and non-polar compounds. DMSO dose-response experiments using FB and cervical SC Rosette Arrays were conducted to investigate the solvent's effect on cell viability/proliferation (Cells/Tissue), neural induction[42] (%Pax6$^+$), and singular rosette emergence (% Single Rosettes). Both FB- and SC-Rosette Arrays only showed cytotoxicity and inhibition of neural induction effects at DMSO levels exceeding 1.0% v/v. However, rosette emergence was inhibited at >0.1% DMSO v/v, representing its upper limit for use in Rosette Array assays (**Figure 7**). Interestingly, 0.1% DMSO media supplementation corresponded with a significant increase in FB Rosette Array singular rosette emergence (91.69 ± 8.94%) but not in SC Rosette Arrays (51.45 ± 6.00%), (**Figure 5E**). We attribute this region-specific effect to DMSO's known capacity for reversibly arresting hPSCs, but not necessarily NMPs, in the early G1 cell cycle phase thereby facilitating differentiation[43,44]. The SC Rosette Array's persistently lower singular rosette emergence efficiency remained a concern, but collectively, these results support the feasibility of deriving Rosette Arrays by direct seeding of cryopreserved hPSCs and NMPs. Moreover, as demonstrated in other publications describing micropatterned morphogenesis of NEC-containing tissues[26–28], the hPSCs are seeded as a monolayer, and coincident with neural induction (Pax6$^+$/N-cadherin$^+$),

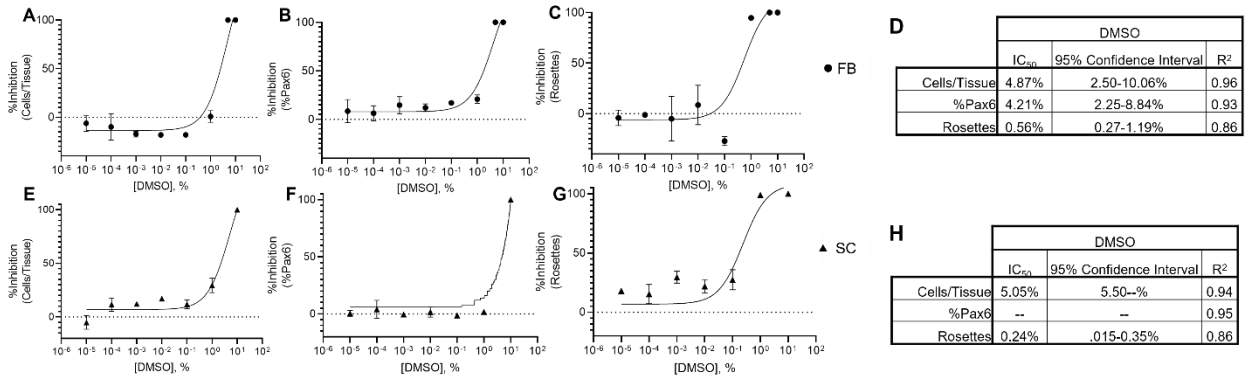

Figure 7. DMSO solvent effects on FB and SC Rosette Arrays. DMSO dose-response (v/v%) for (A-D) FB and (E-H) SC Rosette arrays detailing %inhibition for (A, E) cells/tissue, (B, F) %pax6, and (C, G) rosettes with (D, H) descriptive stats for the non-linear regression, respectively. Each data point is the average of technical triplicate, n=50 tissues analyzed per well. Three-parameter non-linear regression used to model and compare each metric.

morph into 3-D hemispherical forebrain tissues with a central N-cadherin+, polarized rosette structure by Day 5/6 of E6 media culture (**Figure 5F, G**).

FB Rosette Arrays detect risk of NTD-associated teratogens

NEC rosette emergence is an *in vitro* morphogenic analogue to *in vivo* neurulation. As such, we investigated whether FB Rosette Arrays could detect compounds associated with clinically or epidemiologically based NTD risk (**Figure 8**). Glycolic acid (GA) was used as a negative control[45], and benomyl (BNM), valproic acid (VPA), methotrexate (MTX), and novobiocin (NVB) were used as positive controls. BNM has been epidemiologically correlated with NTDs and reported to antagonize the planar cell polarity (PCP) pathway, which is critical for neurulation[46,47]. VPA is an antiepileptic drug and well-known teratogen associated with NTD risk[48,49]. MTX is a chemotherapeutic and potent antagonist of the folate metabolic pathway, which is the best known NTD risk pathway[50,51]. Lastly, NVB is an antibiotic and potential chemotherapeutic that decreases the presence of extracellular matrix (ECM) protein fibronectin through inhibition of HSP-90[52]. Fibronectin plays a critical ECM role in early development and neurulation, and its NVB-mediated reduction at the neural/surface ectoderm interface was recently demonstrated to inhibit *in vitro* neural tube morphogenesis[27].

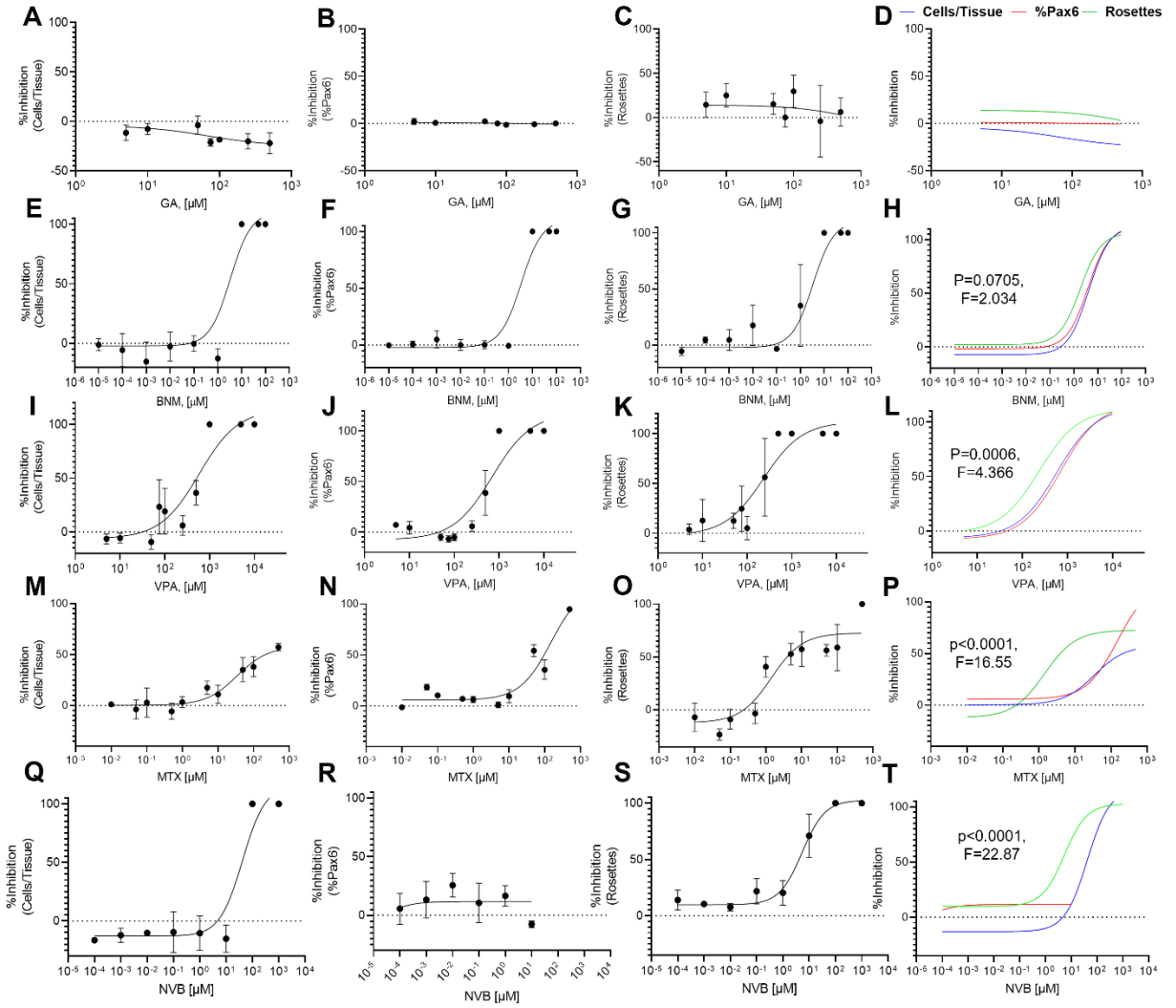

Figure 8. Dose-response of FB Rosette Arrays exposed to Glycolic Acid, Benomyl, Valproic Acid, Methotrexate, and Novobiocin. Glycolic acid dose-response graphs display percent inhibition of (A) Cells/Tissue, (B) %Pax6 expression, and (C) single rosette emergence (Rosettes) plus (D) a composite dose-response curve overlay (Blue-Cells/Tissue, Red-%Pax6, and Green-Rosettes). This is repeated for Benomyl (E-H), Valproic Acid (I-L), Methotrexate (M-P), and Novobiocin (Q-T). Each dose point is the average of a technical triplicate, n=50 tissues per well. Three-parameter non-linear regression used to model and compare each metric.

NTD-risk associated chemical exposures were initiated on the first day of FB Rosette Array neural induction (Day 0) and maintained for the assay's remaining 5 days (**Figure 5C**). Juxtaposition of dose-response curves for the Rosette Array's three primary metrics showed distinct profiles for each NTD risk compound. As expected[45], GA did not inhibit cell viability/proliferation, neural induction, or singular rosette emergence at the levels tested (**Figure**

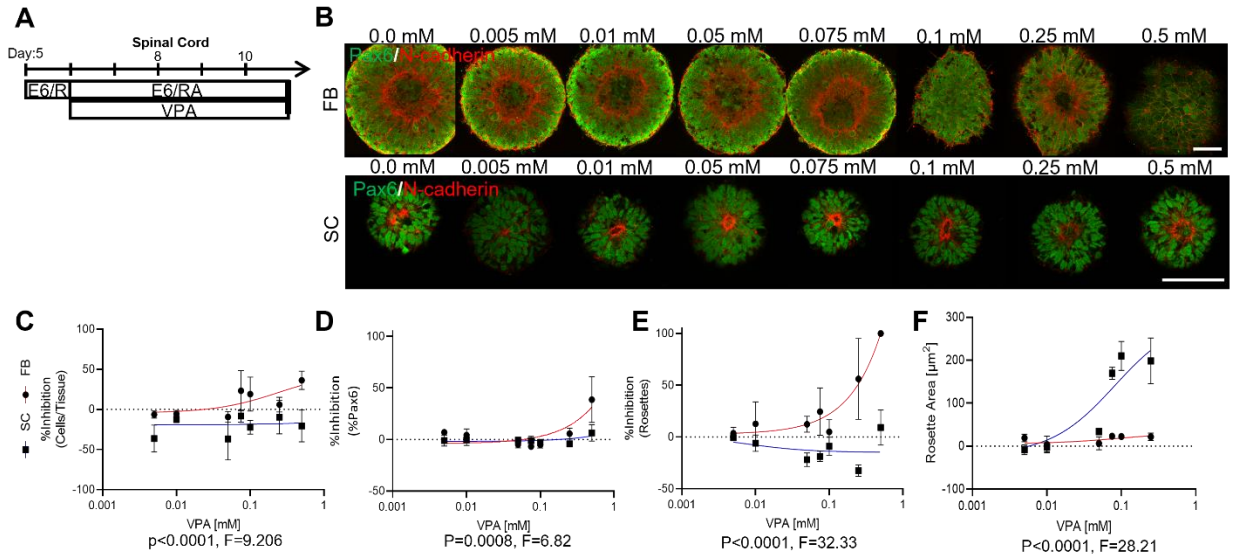

Figure 9. Rosette Arrays display region-specific responses to VPA exposure. (A) Culture schema for SC Rosette Array VPA dose-response experiments with (B) representative images of immunostained FB and SC rosettes. Comparison of FB and SC Rosette Array dose-response curves for percent inhibition of (C) Cells/Tissue, (D) %Pax6 expression, and (E) single rosette emergence (Rosettes) as well as (F) measured N-cadherin^{+} polarized ring area. Technical triplicates for each dose, n=50 tissues/well. Three parameter non-linear regression used to model and compare each metric. Scale bars are 100 µm.

8A-D). However, BNM exhibited cytotoxic (Cells/Tissue) effects along with inhibition of neural induction and rosette emergence at >1 µM (**Figures 8E-H**). Similarly, VPA and MTX exhibited cytotoxicity at the highest tested concentrations (**Figure 8I, M**), but at non-cytotoxic concentrations, they also displayed inhibition of singular rosette emergence (**Figure 8I-L, M-P**). For example, MTX's rosette emergence IC_{50} was ~25-fold and ~108-fold less than those noted for cytotoxicity and inhibition of Pax6 neural induction, respectively **(Figures 8P**). MTX's selective effect on rosette emergence is indicative of its targeted inhibition of the NTD-associated folate metabolic pathway[53]. Similarly, novobiocin also inhibited rosette emergence at concentrations showing no effects on cell viability/proliferation or neural induction metrics (**Figures 8Q-T**). Interestingly, the FB Rosette Array assay detected novobiocin's NTD risk despite not having non-neural ectodermal cells, i.e., the purported source of fibronectin matrix production in other *in vitro* neural tube models[27]. Overall, the sensitivity of the neural rosette morphogenic metric highlights the Rosette Array assay's ability to detect perturbations to

pathways known to orchestrate *in vivo* neural tube genesis and whose disruption causes NTD risk.

Rosette Array platform shows regional differences in VPA's NTD risk

FB Rosette Array assays detect the NTD risk associated with VPA exposure showing complete inhibition of rosette emergence at ≥0.5 mM concentrations (**Figure 8I-L**). However clinically, VPA exposures are observed to predominantly cause NTDs in the spinal cord[54,55]. Thus, the effect of VPA exposure on cervical SC Rosette Arrays was evaluated for comparison (**Figure 9A**). In contrast to FB Rosette Arrays, VPA did not significantly inhibit cervical SC Rosette Array cell viability/proliferation, neural induction, or rosette emergence up to 0.5 mM (**Figure 9C-E**). Yet, the N-cadherin+ polarized ring area, i.e., 'Rosette Area', in cervical SC rosettes increased in a dose-responsive manner, which was a phenomenon not observed in VPA-exposed FB rosettes (**Figure 8B, F**). This indicates a region-specific response to VPA exposure captured by the Rosette Array platform, aligning with clinical data[54,55]and mouse embryo studies, in which VPA exposure biomechanically disrupts closure of the posterior neural tube[49]. Concordantly, we previously showed that biomechanical differences between FB and SC rosette tissues were responsible for needing different micropattern dimensions (i.e., 250 vs. 150 μm, respectively) to preferentially induce singular polarize rosette emergence (**Figure 4**)[24]. The ability to interrogate hPSC-derived neural rosette morphogenesis across the neuraxis is unique to the Rosette Array platform and potentially enables discrimination between adverse effects in rostral and caudal NTD mechanisms.

Discussion and Conclusions

These results demonstrated the potential of the Rosette Array to be used as a tool for NTD risk factor assessment. By validating the first known rosette screening workflow that

allows for the use of cryopreserved hPSCs[26,27,42], is completed in a relatively short period of time compared to other organoid cultures (**Figure 5**)[6,42], and is sensitive to perturbations from historical NTD causing pharmaceuticals (**Figures 8 and 9**), we established a proof-of-concept NTD assessment platform within a human genetic background. Furthermore, the inclusion of a caudalized, cervical spinal-identifying tissue increased the physiological relevance of the model given the variable regional localities of NTDs within the human population[56,57], in stark contrast to the majority of alternative hPSC[26,27,33] and animal models[57]. The importance of considering multiple regions of the developing neuraxis is displayed not only in the differing required culture conditions between forebrain and spinal (**Figure 5**), but the disparate response between identities seen with perturbation from Rho/Rock pathway inhibition (**Figure 4**)[24] or valproic acid (**Figure 9**).

While these early results were promising, several limitations and/or gaps in the assay's capabilities had yet to be addressed. Most importantly, the ability of the assay to detect genetic or multifactorial, i.e., genetic and pharmacologic combinatorial scenarios, NTD risk factors remained unexplored. Additionally, while the 12-well format of the assay enabled the opportunity to conduct pharmacologic dose-response experiments **(Figures 8 and 9**), this required a significant amount of effort and cost to repeatedly conduct. Transitioning the assay to the 96-well plate platform to reach the experimental scale necessary for multi-variable dose-response experiments would better allow for quantitative comparison. Finally, while the capability of exploring the cervical spinal region was available, the relatively low single neural rosette emergence (~50%) seen in the presence of DMSO (**Figure 5E**) potentially limited the utility to draw comparisons. Moreover, while the cervical region is representative of the rostral spinal cord, the assay did not represent the more caudal lumbar region that is most represented in

spina bifida, the most common human NTD presentation[39]. Given the substantial relevance of our early findings, we set out to explore and engineer solutions to these identified limitations.

Bibliography

1. Thomson, J. A. *et al.* Embryonic Stem Cell Lines Derived from Human Blastocysts. *Science* **282**, 1145–1147 (1998).

2. Clevers, H. Modeling Development and Disease with Organoids. *Cell* **165**, 1586–1597 (2016).

3. Lancaster, M. A. & Knoblich, J. A. Organogenesis in a dish: Modeling development and disease using organoid technologies. *Science* **345**, (2014).

4. Ring, K. L. *et al.* Direct Reprogramming of Mouse and Human Fibroblasts into Multipotent Neural Stem Cells with a Single Factor. *Cell Stem Cell* **11**, 100–109 (2012).

5. Zhang, S.-C., Wernig, M., Duncan, I. D., Brüstle, O. & Thomson, J. A. In vitro differentiation of transplantable neural precursors from human embryonic stem cells. *Nature Biotechnology* **19**, 1129–1133 (2001).

6. Lancaster, M. A. *et al.* Cerebral organoids model human brain development and microcephaly. *Nature* **501**, 373–379 (2013).

7. Eze, U. C., Bhaduri, A., Haeussler, M., Nowakowski, T. J. & Kriegstein, A. R. Single-cell atlas of early human brain development highlights heterogeneity of human neuroepithelial cells and early radial glia. *Nat Neurosci* **24**, 584–594 (2021).

8. Atamian, A. *et al.* Human cerebellar organoids with functional Purkinje cells. *Cell Stem Cell* **31**, 39-51.e6 (2024).

9. Phillips, M. J. *et al.* Blood-derived human iPS cells generate optic vesicle-like structures with the capacity to form retinal laminae and develop synapses. *Invest Ophthalmol Vis Sci* **53**, 2007–2019 (2012).

10. Jo, J. *et al.* Midbrain-like Organoids from Human Pluripotent Stem Cells Contain Functional Dopaminergic and Neuromelanin-Producing Neurons. *Cell Stem Cell* **19**, 248–257 (2016).

11. Fedorchak, N. J., Iyer, N. & Ashton, R. S. Bioengineering tissue morphogenesis and function in human neural organoids. *Seminars in Cell & Developmental Biology* **111**, 52–59 (2021).

12. Y, W., S, P., Rh, F. & Y, Z. Organoids as a new model system to study neural tube defects. *FASEB journal : official publication of the Federation of American Societies for Experimental Biology* **35**, (2021).

13. Meinhardt, A. *et al.* 3D Reconstitution of the Patterned Neural Tube from Embryonic Stem Cells. *Stem Cell Reports* **3**, 987–999 (2014).

14. Demers, C. J. *et al.* Development-on-chip: in vitro neural tube patterning with a microfluidic device. *Development* **143**, 1884–1892 (2016).

15. Ogura, T., Sakaguchi, H., Miyamoto, S. & Takahashi, J. Three-dimensional induction of dorsal, intermediate and ventral spinal cord tissues from human pluripotent stem cells. *Development* **145**, (2018).

16. Duval, N. *et al.* BMP4 patterns Smad activity and generates stereotyped cell fate organization in spinal organoids. *Development* **146**, (2019).

17. Libby, A. R. G. *et al.* Axial elongation of caudalized human organoids mimics aspects of neural tube development. *Development* **148**, dev198275 (2021).

18. Rifes, P. *et al.* Modeling neural tube development by differentiation of human embryonic stem cells in a microfluidic WNT gradient. *Nature Biotechnology* **38**, 1265–1273 (2020).

19. Xue, X. *et al.* A Patterned Human Neural Tube Model Using Microfluidic Gradients. *Nature* 1–3 (2024) doi:10.1038/s41586-024-07204-7.

20. Shi, Y., Kirwan, P., Smith, J., Robinson, H. P. C. & Livesey, F. J. Human cerebral cortex development from pluripotent stem cells to functional excitatory synapses. *Nature Neuroscience* **15**, 477–486 (2012).

21. Eiraku, M. *et al.* Self-Organized Formation of Polarized Cortical Tissues from ESCs and Its Active Manipulation by Extrinsic Signals. *Cell Stem Cell* **3**, 519–532 (2008).

22. Birtele, M. *et al.* Non-synaptic function of the autism spectrum disorder-associated gene SYNGAP1 in cortical neurogenesis. *Nat Neurosci* **26**, 2090–2103 (2023).

23. Miotto, M. *et al.* Collective behavior and self-organization in neural rosette morphogenesis. *Front Cell Dev Biol* **11**, 1134091 (2023).

24. Knight, G. T., **Lundin, B. F.,** *et al.* Engineering induction of singular neural rosette emergence within hPSC-derived tissues. *eLife* **7**, e37549 (2018).

25. Wang, Y. *et al.* Modeling human telencephalic development and autism-associated SHANK3 deficiency using organoids generated from single neural rosettes. *Nat Commun* **13**, 5688 (2022).

26. Tidball, A. M. *et al.* Deriving early single-rosette brain organoids from human pluripotent stem cells. *Stem Cell Reports* **18**, 2498–2514 (2023).

27. Karzbrun, E. *et al.* Human neural tube morphogenesis in vitro by geometric constraints. *Nature* **599**, 268–272 (2021).

28. Haremaki, T. *et al.* Self-organizing neuruloids model developmental aspects of Huntington's disease in the ectodermal compartment. *Nat Biotechnol* **37**, 1198–1208 (2019).

29. Lippmann, E. S., Estevez-Silva, M. C. & Ashton, R. S. Defined Human Pluripotent Stem Cell Culture Enables Highly Efficient Neuroepithelium Derivation Without Small Molecule Inhibitors. *STEM CELLS* 1032–1042 (2017) doi:10.1002/stem.1622@10.1002/(ISSN)1549-4918.SpecialNeuralStemCellsVirtualIssue.

30. Lippmann, E. S. *et al.* Deterministic HOX Patterning in Human Pluripotent Stem Cell-Derived Neuroectoderm. *Stem Cell Reports* **4**, 632–644 (2015).

31. Botto, L. D., Moore, C. A., Khoury, M. J. & Erickson, J. D. Neural-Tube Defects. *New England Journal of Medicine* **341**, 1509–1519 (1999).

32. Dreser, N. *et al.* Development of a neural rosette formation assay (RoFA) to identify neurodevelopmental toxicants and to characterize their transcriptome disturbances. *Arch Toxicol* **94**, 151–171 (2020).

33. Miranda, C. C. *et al.* A scale out approach towards neural induction of human induced pluripotent stem cells for neurodevelopmental toxicity studies. *Toxicology Letters* **294**, 51–60 (2018).

34. Paulsen, B. *et al.* Autism genes converge on asynchronous development of shared neuron classes. *Nature* **602**, 268–273 (2022).

35. Jourdon, A. *et al.* Modeling idiopathic autism in forebrain organoids reveals an imbalance of excitatory cortical neuron subtypes during early neurogenesis. *Nat Neurosci* **26**, 1505–1515 (2023).

36. Notaras, M. *et al.* Schizophrenia is defined by cell-specific neuropathology and multiple neurodevelopmental mechanisms in patient-derived cerebral organoids. *Mol Psychiatry* **27**, 1416–1434 (2022).

37. Hendricks, E. *et al.* The C9ORF72 repeat expansion alters neurodevelopment. *Cell Rep* **42**, 112983 (2023).

38. Lee, J.-H. *et al.* Production of human spinal-cord organoids recapitulating neural-tube morphogenesis. *Nat. Biomed. Eng* 1–14 (2022) doi:10.1038/s41551-022-00868-4.

39. Iskandar, B. J. & Finnell, R. H. Spina Bifida. *New England Journal of Medicine* **387**, 444–450 (2022).

40. Iyer, N. R. *et al.* Modular derivation of diverse, regionally discrete human posterior CNS neurons enables discovery of transcriptomic patterns. *Sci. Adv.* **8**, eabn7430 (2022).

41. Hanson, C. & Caisander, G. Human embryonic stem cells and chromosome stability. *APMIS* **113**, 751–755 (2005).

42. Zhang, X. *et al.* Pax6 is a human neuroectoderm cell fate determinant. *Cell Stem Cell* **7**, 90–100 (2010).

43. Chetty, S. *et al.* A simple tool to improve pluripotent stem cell differentiation. *Nat Methods* **10**, 553–556 (2013).

44. Li, J. *et al.* A transient DMSO treatment increases the differentiation potential of human pluripotent stem cells through the Rb family. *PLoS One* **13**, e0208110 (2018).

45. Daston, G. P. *et al.* Exposure-Based Validation List for Developmental Toxicity Screening Assays. *Birth Defects Research Part B: Developmental and Reproductive Toxicology* **101**, 423–428 (2014).

46. Rull, R. P., Ritz, B. & Shaw, G. M. Neural Tube Defects and Maternal Residential Proximity to Agricultural Pesticide Applications. *American Journal of Epidemiology* **163**, 743–753 (2006).

47. Nishimura, T., Honda, H. & Takeichi, M. Planar Cell Polarity Links Axes of Spatial Dynamics in Neural-Tube Closure. *Cell* **149**, 1084–1097 (2012).

48. Lammer, E. J., Sever, L. E. & Oakley, G. P. Valproic acid. *Teratology* **35**, 465–473 (1987).

49. Hughes, A., Greene, N. D. E., Copp, A. J. & Galea, G. L. Valproic acid disrupts the biomechanics of late spinal neural tube closure in mouse embryos. *Mechanisms of Development* **149**, 20–26 (2018).

50. Fleming, A. & Copp, A. J. Embryonic folate metabolism and mouse neural tube defects. *Science* **280**, 2107–2109 (1998).

51. Warkany, J. Aminopterin and methotrexate: Folic acid deficiency. *Teratology* **17**, 353–357 (1978).

52. Hunter, M. C. *et al.* Hsp90 binds directly to fibronectin (FN) and inhibition reduces the extracellular fibronectin matrix in breast cancer cells. *PLoS One* **9**, e86842 (2014).

53. Balashova, O. A. *et al.* Noncanonical function of folate through folate receptor 1 during neural tube formation. *Nat Commun* **15**, 1642 (2024).

54. Robert, E. & Guibaud, P. MATERNAL VALPROIC ACID AND CONGENITAL NEURAL TUBE DEFECTS. *The Lancet* **320**, 937 (1982).

55. Lindhout, D. & Meinardi, H. Spina bifida and in-utero exposure to valproate. *Lancet* **2**, 396 (1984).

56. Nikolopoulou, E., Galea, G. L., Rolo, A., Greene, N. D. E. & Copp, A. J. Neural tube closure: cellular, molecular and biomechanical mechanisms. *Development* **144**, 552–566 (2017).

57. Juriloff, D. M. & Harris, M. J. Insights into the Etiology of Mammalian Neural Tube Closure Defects from Developmental, Genetic and Evolutionary Studies. *Journal of Developmental Biology* **6**, 22 (2018).

58. **Brady F. Lundin** et al. RosetteArray® Platform for Quantitative High-Throughput Screening of Human Neurodevelopmental Risk. bioRxiv 2024.04.01.587605 (2024) doi:10.1101/2024.04.01.587605

Chapter 3 - Enabling Clinically Relevant NTD Screening within the Rosette Array

Introduction

The high prevalence and complicated multifactorial etiology of NTDs in the human population, coupled with the great burden imposed on the lives of affected patients and their families, presents a call to action for science and medicine for further study and understanding of their cause and treatment[1]. Fortunately, many have answered the call through both clinical innovation[2] and the creation of a vast library of animal[3], and more recently, stem cell-based[4] models. Collectively, these have aided in a greater understanding of NTD formation and improved treatment outcomes, yet work remains. For example, despite the successful reduction of folate-sensitive NTDs[5], folate-resistant NTDs occur regularly despite proper supplementation[6–8]. Furthermore, while some level of folate supplementation is undoubtedly beneficial, a clear understanding of how supplementation contributes to case reduction is elusive[5], nor is there consensus on proper dosing[9] despite government mandated fortification, ubiquitous recommendation to women of child bearing age, and known cross-generation effects[2,10]. With arising questions of NTD risk caused by newly introduced life-saving pharmaceuticals[11–14], evolving disease mechanism hypotheses[15–18], and a rapidly increasing prevalence of known NTD risk factors[19–21], the need for model platforms that have physiologic relevance and the ability to be adapted for a variety of investigative questions is clear.

Indeed, already many groups have realized the potential of hPSCs and organoid technology to create platforms with the goal of addressing such questions[22–28], and contributed to a greater understanding of development[29] and the collection of NTD disease[30]. This includes the demonstration that NTD patient-derived induced PSC (iPSC) neural rosette cultures demonstrate a disease phenotype[27,28,31], in addition to other diseases of neurodevelopment[32], suggesting that a

neural rosette array should be capable of genetic risk factor prediction and quantification. However, these studies, as well as the aforementioned organoid platforms, have several limitations. First, the NTD genetic risk factors that demonstrated a NTD disease phenotype were not compared to isogenic controls, limiting their ability to quantify risk contribution[27,28,31]. Second, these same experimental culture platforms rely on spontaneous neural rosette formation in space and time, thereby inhibiting their standardization as a sensitive, high-throughput screening platform with predetermined morphogenetic endpoints. Finally, the studies that did demonstrate a relatively improved experimental scale were limited to rostral forebrain NEC derivation[22–24], failing to account for the more caudal regions traditionally involved in NTD disease presentation. Collectively, even with the introduction of this new wave of stem cell biology, the current disease model landscape presents a limited ability to conduct multifactorial risk screens most pertinent to human disease while accounting for the most physiologically relevant variables of a human genetic background and the morphogenetic variation of the R/C neuraxis[33].

As such, we set out to scale-up the Rosette Array assay to a 96-well plate format while maintaining both the demonstrated reproducible and efficient singular rosette emergence seen in 12-well cultures, as well as the ability to characterize and analyze the increased amount of data generated from the increased experimental throughput. Next, we targeted optimization of the derivation of SC regional assays, including the introduction of the more caudal lumbar region most relevant to clinical spina bifida[2]. Lastly, to explore the ability of the Rosette Array to predict genetic risk factors, gene-edited stem cell lines with clinically identified mutations that perturb the folate metabolic and planar cell polarity pathways, the two pathways known to impact human disease with certainty[1], were created. With these goals achieved, we next aim to

demonstrate the utility of the Rosette Array for conducting clinically relevant quantitative high throughput screening of NTD risk factors.

Experimental Methods

Experimental Contribution

Brady Lundin (B.F.L), Gavin Knight (G.T.K.), and Randolph Ashton (R.S.A.) took part in conception and design of all Rosette Array experiments and jointly interpreted all data. Kevin Krucki (K.K.) and Rebecca Willett (R.W.) conceived and designed all RosetteDetect experiments and jointly interpreted all related data. **B.F.L.** and G.T.K. performed all Rosette Array experimentation unless otherwise noted. Nikolai Fedorchak (N.J.K.) performed all Rosette Array assays whose control data was included in Z-factor analysis. Nisha Iyer (N.R.I.) aided in derivation of WA09 and SCRIB mutant cell banks. **B.F.L.**, G.T.K., N.J.F., Jack Maher (J.E.M.), and Madeline Cicero (M.R.C.) assisted with data acquisition and data analysis. Nicholas Izban (N.R.Iz.) and J.E.M. assisted with platform manufacturing, immunostaining, and imaging. Joshua Robinson (J.F.R.) and Bermans Iskandar (B.J.I.) assisted with design and interpretation of DNT and NTD experiments. The majority of these findings can be found in this submitted manuscript (**Brady F. Lundin** et al. RosetteArray® Platform for Quantitative High-Throughput Screening of Human Neurodevelopmental Risk. bioRxiv 2024.04.01.587605 (2024) doi:10.1101/2024.04.01.587605).

Culture Substrate Fabrication

12-well Rosette Array culture substrates were generated as previously described in Chapter 2. To optimize the culture substrate for spinal Rosette Array tissues, a custom PDMS stamp featuring rectangular arrays of circular recessions with 200, 175, 150, 125 and 100 μm diameters was

created and used to transfer and establish a SAM of 2mM ω-mercaptoundecyl bromoizobutyrate onto gold-coated No. 1 glass coverslips. Onto which, PEGMEMA brushes were grafted using sodium ascorbate initiated ATRP under inert gas for 16 hours at room temperature. Trace copper ions and residual organic solvents were removed through subsequent washes with 70% ethanol in water. 96-well plate RosetteArrays were obtained from Neurosetta LLC.

Cell Culture

WA09 (H9, XX) hESC were supplied by the WiCell Research Institute. WA09 hESCs and the gene edited derivates were maintained at 37°C in 5% CO2 in E8 medium under feeder-free conditions on Matrigel (WiCell)-coated 6-well plates (Corning). For maintenance and expansion, the cells were subcultured in Versene every 5 days at a 1:12 ratio following ~85% confluency. For cell line authentication, each cell line (WA09 parent and 5 edited clones) was submitted to WiCell for karyotyping and mycoplasma testing and results returned validated.

NMP Derivation

WA09 hESCs and gene-edited mutants were differentiated into cervical and lumbar NMPs as previously described[34,35] utilizing CHIR99021, FGF8b, GDF11, and dorsomorphin. Briefly, hESCs were seeded at a density of 1.5×10^5 cells/cm^2 in E8 medium with 10 μM ROCK inhibitor for 24 hours. The medium was replaced with E6 medium on day 0 and then changed to E6 supplemented with FGF8b (200 ng/ml) 24 hours later (day 1). On day 2, cells were subcultured at a 2:3 ratio by washing once with PBS, incubating in Accutase for ~2 minutes, and removing them from the surface with gentle pipetting. After centrifugation, cells were gently resuspended in NMP medium, i.e., E6 medium with FGF8b (200 ng/ml) and 3 μM CHIR99021, containing 10 μM Y27632 and seeded on Matrigel-coated plates. This initiates *HOX* colinear and combinatorial expression and is referred to as ‘Hox0’, with 0 representing the hours of CHIR

exposure. NMP medium was replenished on day 4 (Hox48). On day 5 (Hox72), cervical spinal cells were collected for cryopreservation (see next section). Lumbar spinal cells used in the paper were taken directly from previously generated cryopreserved banks[34] but they can be derived by caudalizing past the Hox72 time point. On day 5, cells should be subcultured (2:3) as before using NMP media. On day 7-10, the media should be replenished daily but now supplemented with GDF11 (30 ng/ml) and 1 μM dorsomorphin to stimulate caudal NMP development. On day 9, the cultures should be subcultured at a 1:1 ratio. On day 11 (Hox216), lumbar cells can be collected for cryopreservation.

Cryopreservation and Thaw of hESC and NMPs

Confluent monolayers of WA09 hESCs in 6-well plates were prepared for cryopreservation through enzymatic dissociation in Accutase (ThermoFisher) and resuspend at ~6,000,000 cells/mL in E8 medium with 10 μM ROCK inhibitor Y-27632 and 10% DMSO. WA09-derived NMPs were similarly dissociated in Accutase and resuspended in E6 medium at ~6,000,000 cells/mL with 10 μM ROCK inhibitor and 10% DMSO. Cryopreservation was performed in Cryovials (Wheaton, Ref#: W985922) at 1mL/vial using a Thermo Scientific CryoMed Controlled-Rate Freezer (7450) set to lower temperature at the following rates; -10°C/min to 4°C, -1°C/min to -60°C, and -10°C/min to -100°C. Cryopreserved vials of cells were placed in liquid nitrogen dewars for extended storage. Cells were thawed at 37°C for 3-5 mins and resuspended in E8 medium with 10 μM ROCK inhibitor for hESC seeding or E6 medium with 10 μM ROCK inhibitor and 1 μM RA for NMP seeding.

Forebrain and Spinal Cord Rosette Array Derivation

FB Rosette Array derivation was initiated by thawing and seeding cryopreserved hESCs at ~200,000 cells/cm^2 onto Matrigel-coated micropatterned arrays with 250 μm diameter circular

regions in E8 medium with 10 μM ROCK inhibitor Y-27632. After 1 day, they were cultured in E6 medium for 5-7 subsequent days using daily 50% media changes. SC Rosette Array derivation was initiated by thawing and seeding cryopreserved hNMPs at ~150,000 cells/cm^2 onto Matrigel-coated micropatterned arrays with 100 or 150 μm diameter circular regions in E6 medium, 10 μM ROCK inhibitor Y-27632, and 1 μM Retinoic Acid. After 1 day, they were cultured in E6 medium with 1 μM RA for 5 subsequent days using daily 50% media changes. Neuroectoderm monolayers were generated analogously in Matrigel-coated 6 well plates, without the use of micropatterned substrates. All culture was performed in tissue culture polystyrene plates (Corning) in medium supplemented with Penicillin/Streptomycin (ThermoFisher). Standard derivation experiments required E6 medium supplementation with DMSO (Sigma-Aldrich) at 0.01% and 0.1% v/v.

Immunocytochemistry

On the last day of culture, tissues were fixed in 4% paraformaldehyde (PFA) in PBS for ~15 minutes. Micropatterned tissues were permeabilized and blocked with 0.1% Triton-X and 5% Donkey serum in PBS (PBS-DT) for 1 hour at room temperature. Primary antibodies listed in the Key Resource Table were incubated on the substrates at 4°C overnight and at a 1:200 dilution in PBS-DT. This was followed by 3 x 20-minute washes with PBS-DT. Next, secondary antibodies listed in Key Resources Table were incubated on the substrates at 4°C overnight and at a 1:500 dilution in PBS-DT. This was followed by 2 x 20-minute washes with PBS-DT, and cell nuclei were stained with DAPI for 10 minutes in the last PBS wash.

Image Acquisition

A Nikon AR-1 Scanning Confocal Microscope was used to acquire all fluorescent images. Tissues were randomly selected to be imaged from each rosette array. Image acquisition was

performed with a 10, 20, or 60X objective (Nikon) at 512x512 pixels, sampling 5-7 vertical image planes with 1.5 μm vertical spacing.

Image Analysis of Tissue Viability and Neural Induction

Image segmentation (CellProfiler, Harvard) was used to quantify the number of $DAPI^+$ and $Pax6^+$ cells per vertical image plane for each rosette. To minimize double counting of cells between vertical planes, a single, middle image plane was used to generate a relative number of cells (# of $DAPI^+$ cells) per tissue and $\%Pax6^+$ (# of $Pax6^+$ cells / # of $DAPI^+$ cells).

Manual Characterization of Neural Rosette Emergence and Morphology

Rosette emergence was quantified through manual image analysis. For each of the tissues randomly imaged per array, a binary determination of singular rosette or failed single rosette emergence (i.e., no rosette or 2+ polarization foci present) was made. Neural rosettes in micropatterned tissues were identified by the presence of a coherent N-cadherin ring structure. Percent neural rosette emergence was calculated as # singular rosette/tissues per array. In single rosette tissue, rosette morphological characteristics were measured by outlining the boundary of the N-cadherin ring.

Calculation of Z' Factor

The Z' Factor was calculated via: $Z' = 1- (3(\sigma_{postive} + \sigma_{negative})/|\mu_{positive} - \mu_{positive}|)$. Where $\sigma_{postive}$ and $\sigma_{negative}$ represent the standard deviations of the positive (1.0 μM Methotrexate) and negative (E6/0.1% DMSO) controls, respectively, and $\mu_{positive} - \mu_{positive}$ are the means.

Non-linear Regression of Dose-response Curves

GraphPad Prism was used to calculate parameters associated with the Logistic Regression Model, plot sigmoidal dose-response curves, and analyze the curves' fit for different parameters plus calculation of the 95% CIs and R^2 values.

CRISPR/Cas9 gene editing

The UW-Madison Human Stem Cell Editing Core was used to create *MTHFR* and *SCRIB* gene-edited lines. sgRNA sequence identification for each editing site was completed using the CRISPOR design tool[36]. The sgRNAs were ordered from Synthego as a 1.5 nmol synthetic sgRNA with 2'-O-methyl 3' phosphorothioate modification at the first and last 3 nucleotides following the recommended suggestion. hPSCs were cultured in TeSR-PLUS media (StemCell Technologies) on Matrigel until ~80% confluency following standard cell culture protocols. Twenty-four hours before electroporation, cells were treated with CloneR (StemCell Technologies) following manufacturer protocol. Prior to the electroporation, the required sgRNA constructs were reconstituted following manufacturer protocols to a concentration of 150 pmole/µL. 1 µL of reconstituted sgRNA was pooled with 4 µg Cas9 Nuclease protein (TrueCut Cas9 Protein V2, Thermo Fisher Scientific) and 5 µL of Neon Buffer R (Invitrogen) to promote Cas9-RNP complex formation. After 15 minutes, 1.0 µL of ssODN primer (reconstituted to 1 µg/µL concentration, designed with homology overhangs of at least 40 base pairs) was added to the Cas9-RNP mix. Cells were singularized and lifted with a 1:1 mixture of 0.5 mM EDTA: Accutase for 3-4 minutes, resuspended in 1 mL PBS, and pelleted. Approximately 400,000 cells were resuspended in 35 µL Buffer R and mixed with 8 µL of the pre-prepared Cas9-RNP complex with repair ssODN. Cells were electroporated with a 10 µL NEON electroporation format using 1200V, 30 msec, 1x pulse settings. Cells were pooled following four rounds of electroporation and plated in TeSR-PLUS media with CloneR supplement at manufacturer-recommended concentrations following a serial dilution to promote single-cell clonal growth. Following expansion of 10-14 days, clones were identified and picked using standard techniques.

Genotyping

Bulk gDNA was collected from dissociated cells using QuickExtract DNA Extraction Solution 1.0 (Epicentre) to confirm editing efficiency prior to clonal selection. Single-cell clones were manually selected and mechanically disaggregated. Genomic DNA was isolated from a portion of these clones using QuickExtract DNA Extraction Solution 1.0. Genotyping primers were designed flanking the mutation site, allowing amplification of this region using Q5 polymerase-based PCR (NEB). PCR products were identified via agarose gel and purified using a Zymoclean Gel DNA Recovery Kit (Zymo Research). Clones were submitted to Quintara Biosciences for Sanger sequencing to identify clones with the proper genetic modification.

Off-target analysis

To identify whether the CRISPR-Cas9 system produced any non-specific genome editing, we analyzed suspected off-target sites for genome modification. Using the 5 highest-likelihood off-target sites for each sgRNA as predicted by the CRISPOR algorithms, we designed genotyping primers to amplify these regions via Q5-polymerase PCR. PCR products were identified via agarose gel, purified using a Zymoclean Gel DNA Recovery Kit, and submitted to Quintara Biosciences for Sanger sequencing.

Karyotyping

Live cells for all utilized cell lines and edited clones were submitted to WICell for karyotype analysis and returned normal.

Western Blot

SCRIB protein expression was qualitatively confirmed in the WA09 parent and P1043L mutant clones, and its absence was confirmed in the KO mutant clone via western blotting. Briefly, NEC monolayers derived in 6-well plates were pelleted and lysed in RIPA buffer (Thermo Fisher Scientific 89900) containing protease inhibitors (Thermo Fisher Scientific 78429) and stored at -

80 °C. Upon thaw, lysates were analyzed for total protein concentration using the Lowry protein assay (Biorad DC Protein Assay). 25 µg of protein was analyzed on a 4-20% Mini-PROTEAN® TGX™ Precast Gel (Bio-Rad, 4561094) and transferred to polyvinylidene fluoride (PVDF) membranes (Thermo Scientific 88518). The membranes were cut to separate the 215 kDa SCRIB protein from the 50 kDA B-tubulin housekeeping protein and blotted overnight at 4ºC with an anti-SCRIB antibody (1:500; Invitrogen PA5-54821) or Anti-β-tubulin (BioLegend 1:500), respectively. Washes were conducted the next day, and membranes were incubated in horseradish peroxidase-conjugated goat anti-rabbit at room temperature, followed by addition of enhanced chemiluminescence (ECL) substrate (made in-house). Membranes were visualized using a chemiluminescence imager (DNR Bio-Imaging Systems) at 10 second intervals, ~100s total exposure.

Statistical Analysis

GraphPad Prism (V10.2.1) was used for all statistical analysis. Error bars represent mean ± SD; * for $p<0.05$, ** for $p<0.01$, *** for $p<0.001$, **** for $p<0.0001$. Neural rosette emergence for single dose experiments were analyzed with t-tests and all other metrics were analyzed with one-way ANOVAs. Non-linear regression was performed to generate three (Hill Slope =1) or four (Hill Slope not restrained) parameter dose-response curves depending on whether data points were present at the curve's inflection point. Comparison of dose-response curves for different metrics analyzing the same compound were compared using a hypothetical dose-response curve for all metrics. The explanation of "n" and the number of technical or biological replicates completed per experiment, as well as tests done to determine if data met assumptions of statistical approaches, can be found in the figure legends and text.

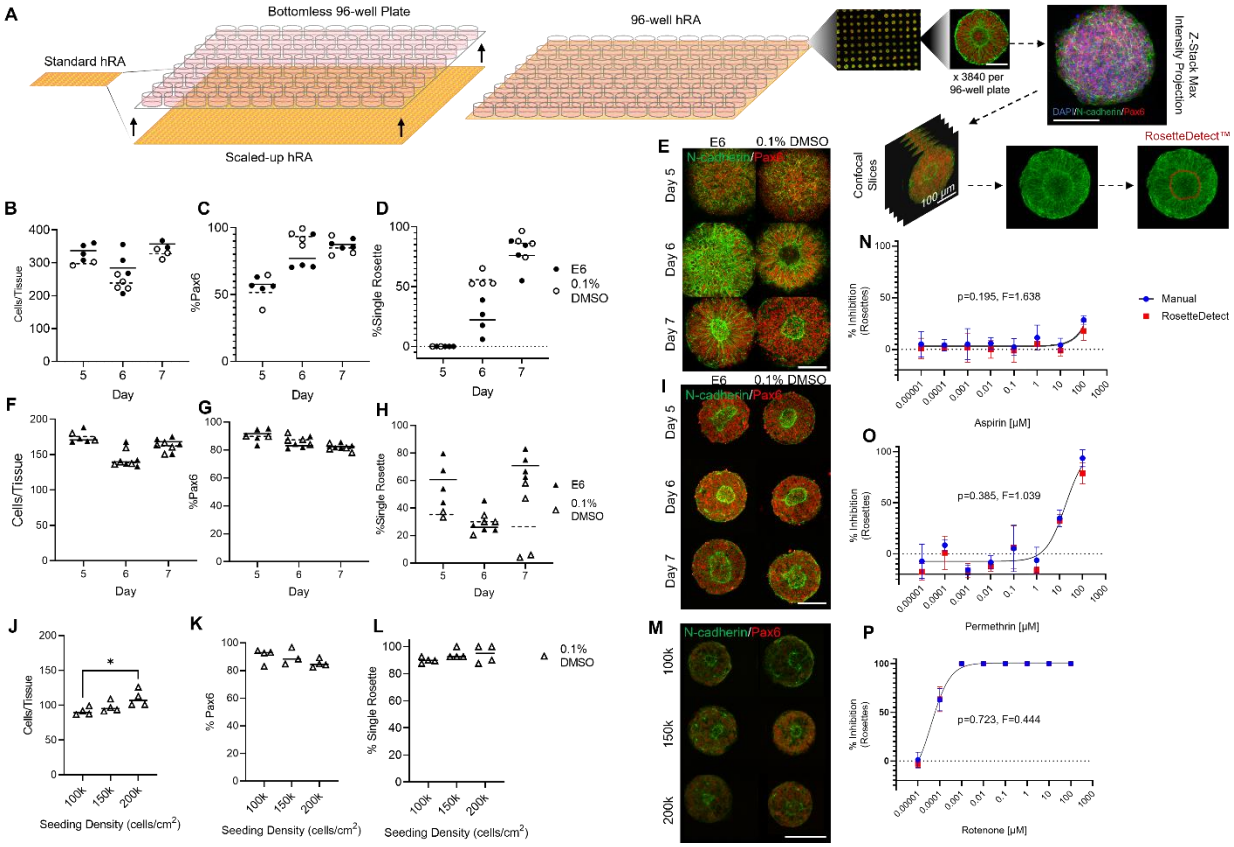

Figure 10. FB and SC Rosette Array assay and analysis scale-up to 96-well plate format. (A) Schematic of 96-well Rosette Array plate manufacture, image acquisition, and RosetteDetect image analysis. Quantification of (B-E) FB and (F-I) cervical spinal 96-well RosetteArrays with and without 0.1% DMSO across differentiation Days 5-7 for (B, F) cells/tissue, (C, G) neural induction, and (D, H) rosette emergence plus (E, I) representative immunostaining. Quantification of Day 5 lumbar spinal Rosette Arrays with 0.1% DMSO at varied seeding density for (J) cells/tissue, (K) neural induction, and (L) rosette emergence plus (M) representative immunostaining. Dose-response curves for manually and RosetteDetect quantified FB Rosette Array assays of (N) Aspirin, (O) Permethrin, and (P) Rotenone. Each data point represents an average across 2-4 technical replicates with n=40 analyzed tissues per well. Scale bars are 100 µm. Significance in dot plots assessed using 1-way ANOVA with Tukey-Kramer post-hoc analysis, * $p \leq 0.05$. Dose-response curves compared using three-parameter non-linear regression models. If curves are statistically equivalent, then only one curve is displayed.

Results and Analysis

Scale up of 96-well plate FB and SC Rosette Array assays

For scale up to a 96-well plate format, Willow® glass sheets were micropatterned and attached to bottomless 96-well plates using a double-sided adhesive as previously described by previous members of the Ashton lab and collaborators[37] (**Figure 10A**). FB Rosette Array scale up

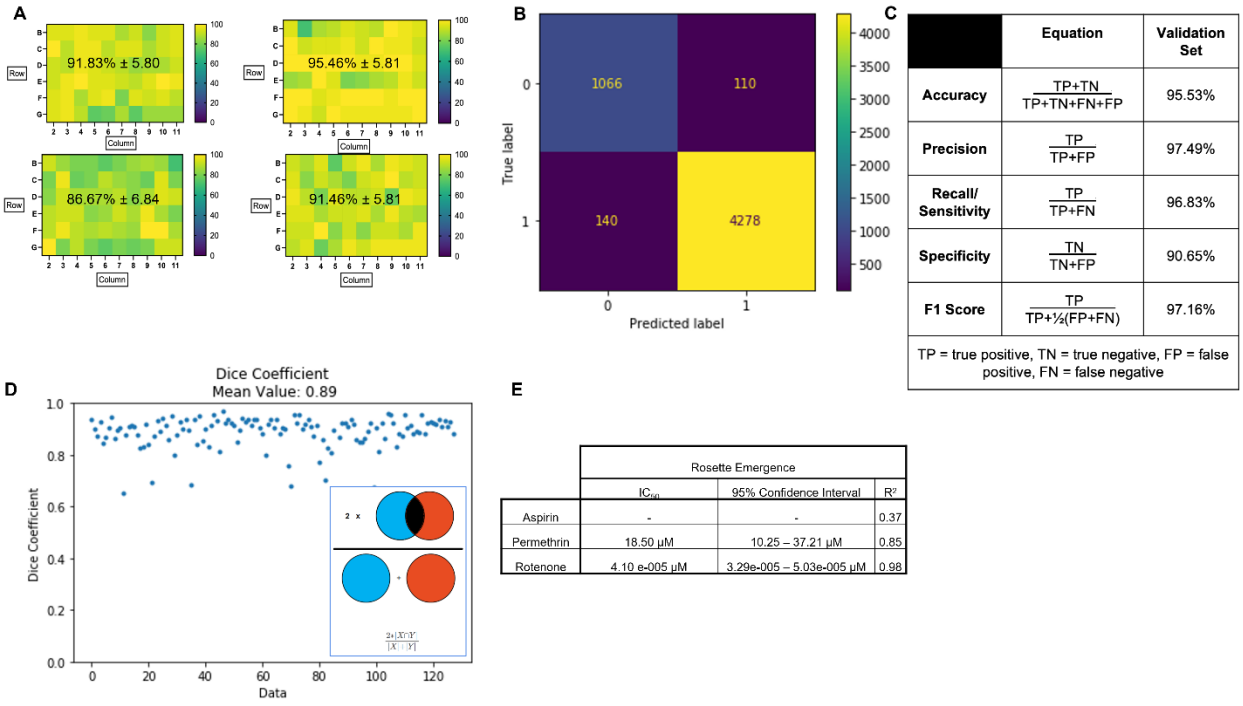

	Equation	Validation Set
Accuracy	$\frac{TP+TN}{TP+TN+FN+FP}$	95.53%
Precision	$\frac{TP}{TP+FP}$	97.49%
Recall/ Sensitivity	$\frac{TP}{TP+FN}$	96.83%
Specificity	$\frac{TN}{TN+FP}$	90.65%
F1 Score	$\frac{TP}{TP+½(FP+FN)}$	97.16%

TP = true positive, TN = true negative, FP = false positive, FN = false negative

	Rosette Emergence		
	IC_{50}	95% Confidence Interval	R^2
Aspirin	-	-	0.37
Permethrin	18.50 µM	10.25 – 37.21 µM	0.85
Rotenone	4.10 e-005 µM	3.29e-005 – 5.03e-005 µM	0.98

Figure 11. 96-well FB Rosette Array and RosetteDetect scale up validation.
(A) Heat map of single neural rosette emergence efficiency across the interior 60 wells for four biological replicates of 96-well FB Rosette Arrays using direct seeding of cryopreserved WA09 hESCs. (B) Confusion matrix determined from RosetteDetect test image dataset post training. (C) Table of RosetteDetect performance metrics across the test image dataset. (D) Dice coefficient graph showing concordance between manually vs. RosetteDetect curated segmentation of polarized N-cadherin$^+$ area across 128 test images. (F) Table of calculated IC_{50} doses, 95% confidence interval metrics, and R^2 for Aspirin, Permethrin, and Rotenone FB Rosette Array dose-response curves.

experiments demonstrated that the 12-well plate protocol did not directly translate to the 96-well format (**Figure 10B-E**). In both E6 and 0.1%DMSO supplemented media conditions, Day 7 vs. Day 5 of culture was required to reach acceptable singular rosette emergence efficiencies (i.e., 76.06 ± 14.94% and 86.27 ± 9.06%, respectively). Using Day 7 as the termination timepoint, the optimized 8-day FB Rosette Array protocol was reproducible across full 96-well plate screens. When conducted in biological quadruplicate, with 0.1% DMSO supplemented media, and using only the interior 60-wells, plate-wide averages for singular rosette emergence were 91.83 ± 5.80%, 95.46 ± 5.81%, 86.67 ± 6.84%, and 91.46 ± 5.81% (**Figure 11A**). Additionally, the FB Rosette Array's Z-prime value is 0.53 across seventeen independent DNT screens using 1µM MTX and E6/0.1% DMSO solvent as our positive and negative control conditions.

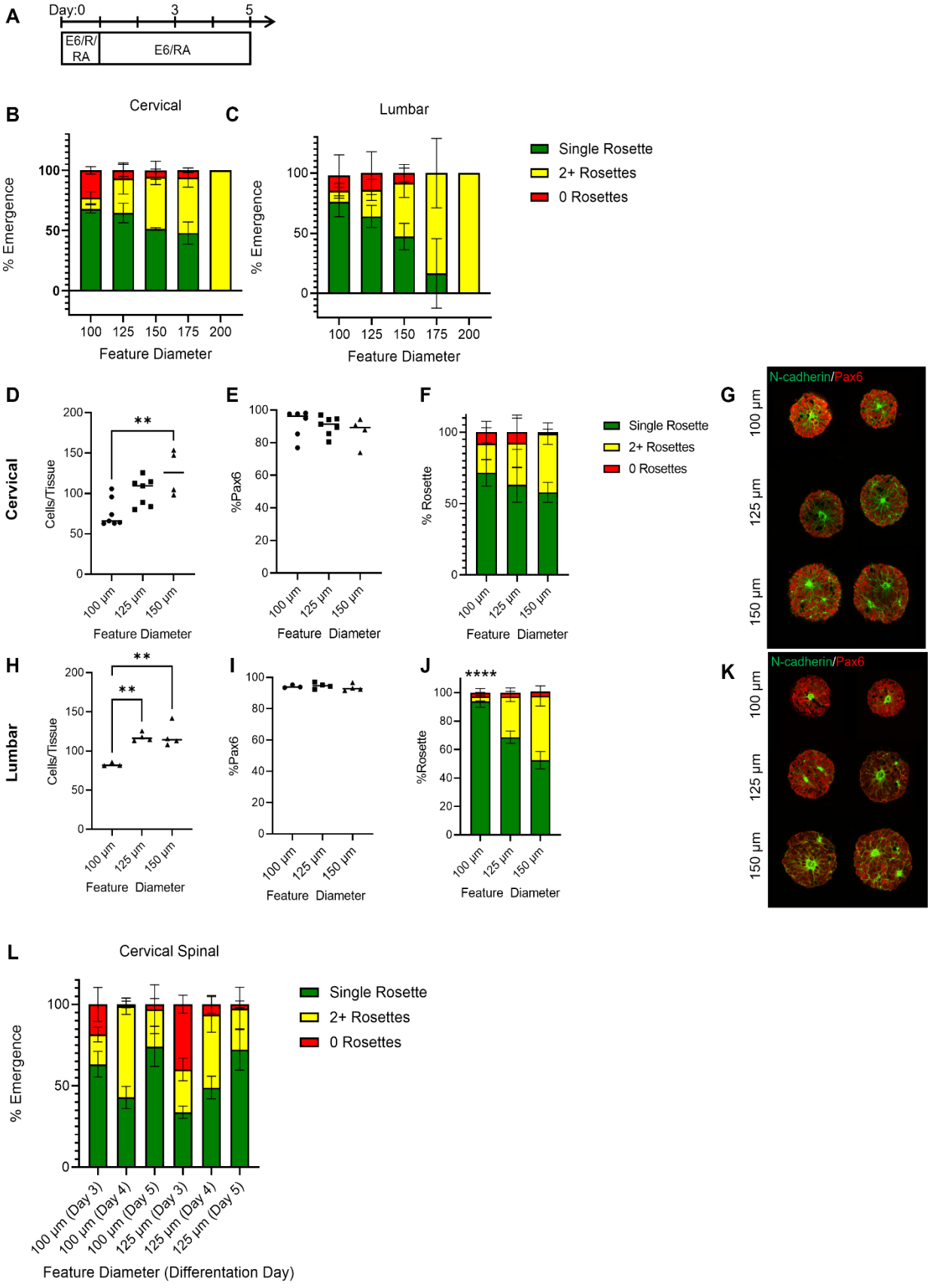
A
Day:0
3
5
E6/R/RA
E6/RA
B
Cervical
C
Lumbar
% Emergence
Feature Diameter
Single Rosette
2+ Rosettes
0 Rosettes
D
Cervical
Cells/Tissue
E
%Pax6
F
% Rosette
G
N-cadherin/Pax6
100 µm
125 µm
150 µm
H
Lumbar
I
J
%Rosette
K
L
Cervical Spinal
100 µm (Day 3)
100 µm (Day 4)
100 µm (Day 5)
125 µm (Day 3)
125 µm (Day 4)
125 µm (Day 5)
Feature Diameter (Differentation Day)

Figure 12. SC Rosette Array optimization.
(A) Culture schema of 12-well plate Rosette Array format used for direct seeding of cryopreserved cervical and lumbar spinal NMPs onto micropatterned substrates. Quantification of cells/tissue, %pax6, and %rosette emergence for tissues grown on a customized array containing increasing diameter features for (B) cervical and (C) lumbar spinal tissues. n=4 technical replicates with 50 tissues per n assessed for each feature diameter. Quantification with representative images for arrays with singular feature diameter for (D-G) cervical and (H-K) lumbar SC Rosette Arrays, respectively. (L) %Rosette emergence quantification for cervical spinal arrays stopped on days 3, 4, and 5 of the assay timeline. n=3-7 technical replicates with each data point representing n=50 analyzed tissues per well. (B, C, F, J, L) Bar graphs of rosette emergence quantification showing distribution of tissues with 0, 1, and 2+ rosette structures. Statistical significance determined using a one-way ANOVA with Tukey-Kramer post-hoc analysis ** $p \leq 0.01$, **** $p \leq 0.0001$.

For cervical SC Rosette Arrays, direct protocol translation yielded even worse singular rosette emergence results (**Figure 10F-I**). For 0.1% DMSO media conditions, the 12-well plate cervical SC Rosette Array's showed its best efficiencies at Day 5/7 of culture, but still much lower than FB Rosette Array efficiency, especially in 0.1% DMSO supplemented media (**Figure 10H**). Thus, to improve the overall utility of the SC assay, its R/C regionalization and micropattern dimension were revisited for optimization in the 12-well format.

To increase the biological relevance of the assay, both cervical and lumbar identifying NMPs[34] were seeded onto a single customized micropatterned array containing juxtaposed columns of features of 100, 125, 175, and 200 μm diameter circles, cultured in E6 media, and assessed for singular rosette emergence at Day 5 (**Figure 12A**). As expected given our previous spinal cord findings[38] and mirroring the shape of neuroectoderm that comprises an *in vivo* neural tube[39] , the general trend of the % single neural rosette emergence suggested that smaller feature diameters (100, 125, and 150 μm) allowed for an increase in singularly polarized tissues for both cervical and lumbar tissues (**Figure 12B, C, respectively**). To confirm this trend and offset any possibility of confounding effects from tissues of alternative feature diameter grown in the same well, the experiment was repeated with homogenous micropatterned arrays containing features of 100, 125, or 150 μm. While rosette emergence within cervical tissues was not significantly sensitive to micropattern dimension within this focused range (**Figure 12D-G**), lumbar-patterned

rosettes displayed robust (93.80 ± 4.10%) singular rosette emergence on 100 μm diameter micropatterns (**Figure 12H-K**). A last effort to better optimize the cervical spinal array was made by prematurely ending the assay on day 3 and 4 to assess if the number of 2+ polarizations seen could be reduced, however day 5 remained the highest % single neural rosette emergence for the two feature diameters tested (**Figure 12L**). Therefore, we elected to continue forward using 100 μm feature diameter array for both SC identities. When the lumbar SC Rosette Array protocol was directly translated to the 96-well plate format, similar singular rosette emergence efficiencies were observed in 0.1% DMSO supplemented media (**Figure 10J-M**).

With successful scale-up to 96-well plate formats, Rosette Array analysis now became a challenge. If automated confocal microscopy is used to acquire just 40 micropatterned tissues per well, then singular rosette emergence within 3840 Z-stack images per plate would need to be analyzed manually (**Figure 9A**). Therefore, we worked with an artificial intelligence (AI) vision analyst and developed RosetteDetect™ software based on convolutional neural networks[40] to automate rosette detection and segmentation within such images. The AI model was trained on 588 images and tested on a separate 5594 image set from DNT dose-response studies. Model validation studies on 'yes/no' identification of singular rosette emergence yielded accuracy, precision, recall/sensitivity, specificity, and F1 score yielded values all >90% (**Figure 11B, C**). Also, the model's ability to segment the singular rosette's polarized N-cadherin ring structure was tested across 128 images producing a Dice Coefficient of 88.64 ± 6.50%, indicating good agreement of the rosette's estimated area with manually curated ground truth data (**Figures 10A and 11D**). As a final demonstration of utility, RosetteDetect's performance in quantifying singular rosette emergence across 3 DNT Rosette Array assays, i.e., Aspirin, Permethrin, and Rotenone, was compared to manual analysis. Dose-response curves generated using either

manual or RosetteDetect analyses were statistically equivalent (**Figure 10N-P and 11E**). With inclusion of CellProfiler™ coding to quantify DAPI+ and Pax6+ cells/image slice, these results collectively demonstrate feasible scaling of Rosette Array assays and analysis for qHTS applications.

Generation of hPSC lines with clinically relevant NTD mutations

In addition to risk being caused by chemical exposures, genetic variants affecting folate metabolic and planar cell polarity (PCP) pathway machinery have also been shown to increase NTD risk[1]. To evaluate the Rosette Array's ability to detect such genetic risk factors, the WA09 hESC line was gene edited to generate clones with clinical gene variants $MTHFR^{C677T(p.A222V)}$[41] and $SCRIB^{C3128T\ (p.P1043L)}$[42]. In the folate metabolic pathway, Methyltetrahydrofolate Reductase (MTHFR) generates 5-methyltetrahydrofolate, which is the metabolized folate form found in blood plasma[41]. The c.C677T mutation decreases the enzymes activity by ~35% in heterozygotes and ~70% in homozygotes[43]. Interestingly, sequencing revealed that the WA09 hESC line was heterozygous for the c.C677T mutation. Therefore, gene editing was used to generate $MTHFR^{C677T(-/-)}$ homozygote clones #4 and #9 (**Figure 13A, B**). In the PCP pathway, the Scribble protein (SCRIB) acts to scaffold protein-complexes at the plasma membrane during epithelial cell apical-basal polarization[44]. Its N-terminal Leucine-Rich-Region (LRR) enables membrane localization, while its four PDZ domains, with the c.C3128T/p.P1043L mutation in its third PDZ domain, are reported to also effect membrane localization and PCP protein interactions[42,44](**Figure 13C**). Gene editing of the WA09 parent line yielded a heterozygous ($SCRIB^{P1043L(+/-)}$, #78), a homozygous ($SCRIB^{P1043L(-/-)}$,#52), and a knockout ($SCRIB^{KO}$, #17) clone. The knockout was caused by a downstream deletion yielding a nonsense frameshift (**Figure 13D-G**). All clones could generate rosette containing cultures in standard 6-well

forebrain NEC derivation experiments[45] (**Figure 13H-J**). Also, the parent and isogenic mutant lines had normal karyotypes with no mycoplasma detection (Analyzed by WiCell, results not shown).

(Next Page) Figure 13. Characterization of MTHFR and SCRIB gene-edited lines.
(A) Representation of coding regions in human MTHFR gene with C677T SNP labeled. (B) Sanger sequence of homozygous MTHFR-#4 and -#9 mutant clones and the heterozygous WA09 isogenic parent line. (C) Representation of human SCRIB protein isoforms with P1043L mutation labeled. (D) Sanger sequence of the (+/-), (-/-), and KO gene-edited clones for c.C3128T SNP. (E) Sequence representation of nonsense deletion in the SCRIB KO line with (F) qualitative protein expression from rosette-forming NECs from each mutant line and the WA09 parent line. (G) Raw western blot images. (H) Culture schema for 6-well plate E6 neural differentiation. (I, J) Representative immunostaining of NECs derived from MTHFR-4 and -9 and the SCRIB KO lines.

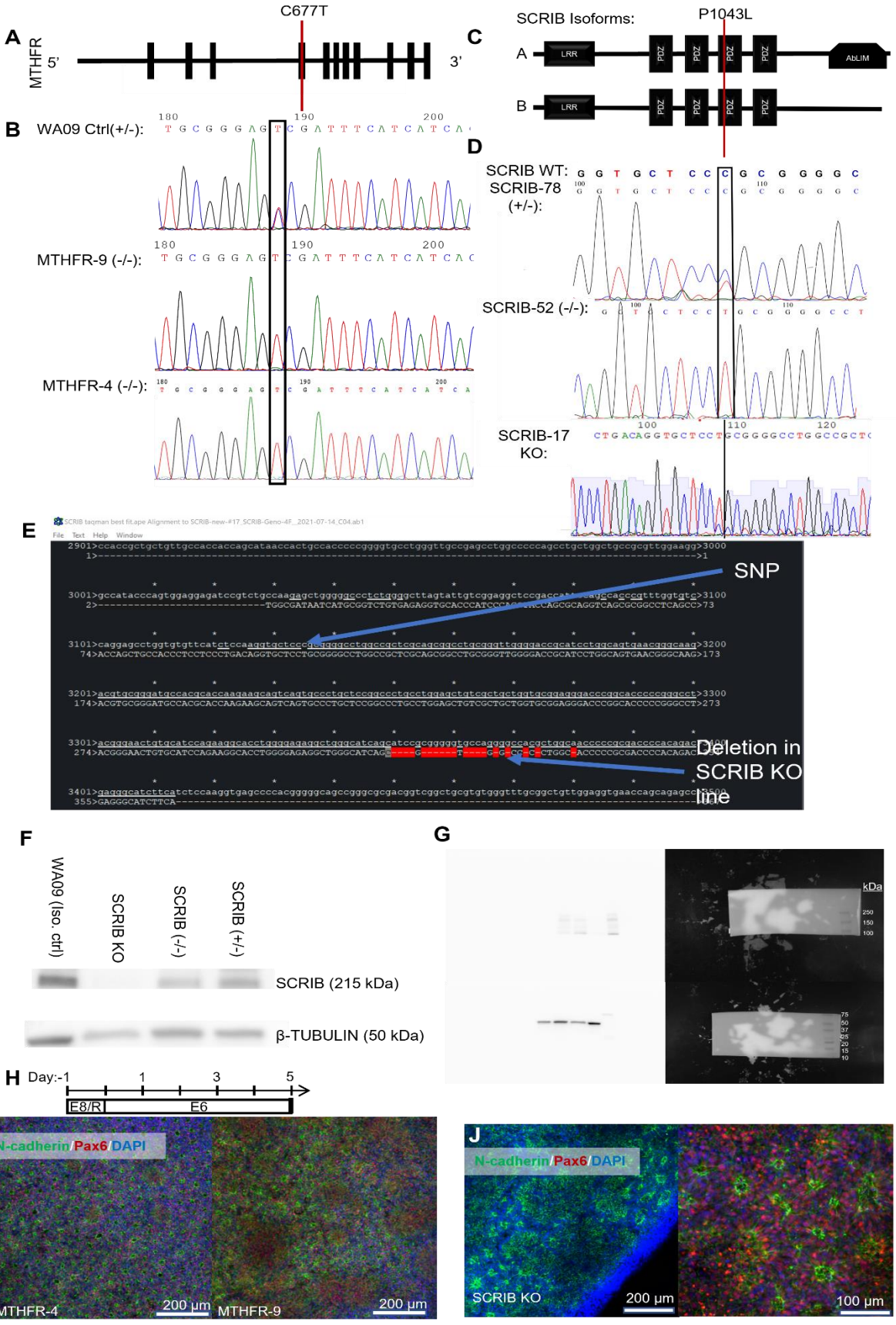
A
MTHFR
5'
C677T
3'
B
WA09 Ctrl(+/-):
MTHFR-9 (-/-):
MTHFR-4 (-/-):
C
SCRIB Isoforms:
P1043L
A
B
LRR
PDZ
AbLIM
D
SCRIB WT:
SCRIB-78 (+/-):
SCRIB-52 (-/-):
SCRIB-17 KO:
E
SNP
Deletion in SCRIB KO line
F
WA09 (Iso. ctrl)
SCRIB KO
SCRIB (-/-)
SCRIB (+/-)
SCRIB (215 kDa)
β-TUBULIN (50 kDa)
G
kDa
H
Day:-1
1
3
5
E8/R
E6
I
N-cadherin/Pax6/DAPI
MTHFR-4
200 µm
MTHFR-9
200 µm
J
N-cadherin/Pax6/DAPI
SCRIB KO
200 µm
100 µm

Discussion and Conclusions

In this chapter, we successfully translated the Rosette Array platform to the 96-well plate format, introduced a lumbar regionally defined assay to represent the spinal region most affected in human NTD disease, and generated hPSC lines containing clinically identified mutations from the two developmental pathways known to contribute to NTDs. These achieved objectives enable the Rosette Array to be utilized as an investigative tool that considers a comprehensive spectrum of R/C regional closure mechanisms within a human genetic background; a capability unmirrored in existing animal and cell disease models, yet crucial to understanding NTD formation risk[33].

The ability to conduct numerous pharmacologic dose-response experiments, compare gene edited lines to their isogenic controls, and conduct combinations of the pharmacologic/genetic paradigms to assess multifactorial risk requires a large experimental throughput. While the 12-well format of the Rosette Array allowed for proof-of-concept validation dose-response experiments (**Figure 8**), this type of volume was not feasible long term and did not allow for expanded experimental conditions. Therefore, we successfully translated the micropatterned arrays to the 96-well format while maintaining high single neural rosette emergence (**Figure 10D, L**). Concurrently, we were able to build an automated imaging and image analysis platform that enables accurate and efficient analysis of data generated from the increased scale (**Figures 10A, N-P, 11**).

Given the relatively low single neural rosette emergence of SC Rosette Arrays seen in early experiments (**Figures 5E, 10H**), we revisited the approach to their derivation (**Figure 12**). This resulted in the addition of a lumbar SC representing region with exceptional standardized tissue morphogenesis (**Figures 10L, 12J**). Interestingly, spinal NMPs representative of the

cervical or lumbar region displayed distinct abilities to form single rosettes (**Figure 12 B, C, F, J**). This indicates that even within the spinal region there are differing morphogenetic mechanisms, echoing what is known about human, and mammalian, development[33]. The optimized HoxD10^{+} lumbar SC Rosette Array facilitates the ability to study the specific region of most interest to spina bifida[2], distinguishing the assay from others that have, at best, represented the HoxC9^{+} cervical region[25,26].

While we had generally demonstrated the ability to conduct high throughput pharmacologic assessment of neural tube morphogenesis representative of multiple CNS regions, we had yet to explore genetic risk assessment. As such we set out to obtain hPSC lines with mutations or backgrounds that contribute to NTD risk. While other groups have generated iPSC lines from patients with spina bifida[27,28], these lines were impossible to obtain given collaborative restrictions and did not have identified risk contributing mutations, making comparative studies to an isogenic control impossible. Therefore, in collaboration with the UW Stem Cell Core, we edited the WA09 parent line to have mutations targeting proteins from either the folate metabolic (MTHFR) or planar cell polarity (SCRIB) pathways (**Figure 13**). The finding that the WA09 line contains a MTHFR$^{C677T(p.A222V)}$ heterozygous mutation is in line with the polymorphism's prevalence[46,47]. Given that functional and disease penetrance differences are most pronounced with two copies of the mutatation[47,48], we elected to continue with the creation of a homozygous mutant for later study (**Figure 13B**). The generation of a SCRIB edited line containing a truncated KO allows for the study of the effects of losing the spectrin binding motif at the c-terminus of the protein[49], in addition to the c.C3128T/p.P1043L PDZ domain mutation clinically correlated with spina bifida[42]. Lastly, while not obtained in time to be included in this writing, working with the UW Spina Bifida Clinic, we were able to successfully derive an iPSC

line from a spina bifida patient with high suspicion of a genetic risk contribution for future characterization and study. Overall, this collection of work establishes the novel ability to conduct multifactorial qHTS of NTD risk factors within a human genetic background, while considering the mechanistic heterogeneity of the CNS neuraxis.

Bibliography

1. Wallingford, J. B., Niswander, L. A., Shaw, G. M. & Finnell, R. H. The Continuing Challenge of Understanding, Preventing, and Treating Neural Tube Defects. *Science* **339**, (2013).

2. Iskandar, B. J. & Finnell, R. H. Spina Bifida. *New England Journal of Medicine* **387**, 444–450 (2022).

3. Zohn, I. E. Mouse Models of Neural Tube Defects. in *Animal Models of Human Birth Defects* (ed. Liu, A.) 39–64 (Springer, Singapore, 2020). doi:10.1007/978-981-15-2389-2_2.

4. Y, W., S, P., Rh, F. & Y, Z. Organoids as a new model system to study neural tube defects. *FASEB journal : official publication of the Federation of American Societies for Experimental Biology* **35**, (2021).

5. Blom, H. J., Shaw, G. M., den Heijer, M. & Finnell, R. H. Neural tube defects and folate: case far from closed. *Nature Reviews Neuroscience* **7**, 724–731 (2006).

6. Copp, A. J. & Greene, N. D. E. Neural tube defects – disorders of neurulation and related embryonic processes. *Wiley Interdiscip Rev Dev Biol* **2**, 213–227 (2013).

7. Williams, J. *et al.* Updated Estimates of Neural Tube Defects Prevented by Mandatory Folic Acid Fortification — United States, 1995–2011. *MMWR Morb Mortal Wkly Rep* **64**, 1–5 (2015).

8. Juriloff, D. M. & Harris, M. J. A consideration of the evidence that genetic defects in planar cell polarity contribute to the etiology of human neural tube defects. *Birth Defects Research Part A: Clinical and Molecular Teratology* **94**, 824–840 (2012).

9. Cao, X. *et al.* Excess folic acid intake increases DNA de novo point mutations. *Cell Discov* **9**, 1–5 (2023).

10. Patel, N. J. *et al.* Ancestral Folate Promotes Neuronal Regeneration in Serial Generations of Progeny. *Mol Neurobiol* **57**, 2048–2071 (2020).

11. Zash, R., Makhema, J. & Shapiro, R. L. Neural-Tube Defects with Dolutegravir Treatment from the Time of Conception. *N Engl J Med* **379**, 979–981 (2018).

12. Chouchana, L., Beeker, N. & Treluyer, J.-M. Is There a Safety Signal for Dolutegravir and Integrase Inhibitors During Pregnancy? *J. Acquir. Immune Defic. Syndr.* **81**, 481–486 (2019).

13. Cabrera, R. M. *et al.* The antagonism of folate receptor by dolutegravir: developmental toxicity reduction by supplemental folic acid. *AIDS* **33**, 1967–1976 (2019).

14. Tukeman, G. L. *et al.* Dolutegravir-induced neural tube defects in mice are folate responsive. *AIDS* **38**, 439–446 (2024).

15. Chen, Z. *et al.* Threshold for neural tube defect risk by accumulated singleton loss-of-function variants. *Cell Research* **28**, 1039–1041 (2018).

16. V, R. P., Finnell, R. H., Ross, M. E., Alarcón, P. & Suazo, J. Neural tube defects and epigenetics: role of histone post-translational histone modifications. *Epigenomics* (2024) doi:10.2217/epi-2023-0357.

17. Imbard, A., Benoist, J.-F. & Blom, H. J. Neural Tube Defects, Folic Acid and Methylation. *International Journal of Environmental Research and Public Health* **10**, 4352–4389 (2013).

18. Wolujewicz, P., Steele, J. W., Kaltschmidt, J. A., Finnell, R. H. & Ross, M. E. Unraveling the complex genetics of neural tube defects: From biological models to human genomics and back. *genesis* **59**, e23459 (2021).

19. Anderson, J. L. *et al.* Maternal Obesity, Gestational Diabetes, and Central Nervous System Birth Defects. *Epidemiology* **16**, 87–92 (2005).

20. Rasmussen, S. A., Chu, S. Y., Kim, S. Y., Schmid, C. H. & Lau, J. Maternal obesity and risk of neural tube defects: a metaanalysis. *American Journal of Obstetrics and Gynecology* **198**, 611–619 (2008).

21. J, B., Pk, T. & D, K. Diabetic Embryopathy. (2020).

22. Tidball, A. M. *et al.* Deriving early single-rosette brain organoids from human pluripotent stem cells. *Stem Cell Reports* **18**, 2498–2514 (2023).

23. Karzbrun, E. *et al.* Human neural tube morphogenesis in vitro by geometric constraints. *Nature* **599**, 268–272 (2021).

24. Miranda, C. C. *et al.* A scale out approach towards neural induction of human induced pluripotent stem cells for neurodevelopmental toxicity studies. *Toxicology Letters* **294**, 51–60 (2018).

25. Xue, X. *et al.* A Patterned Human Neural Tube Model Using Microfluidic Gradients. *Nature* (2024) doi:10.1038/s41586-024-07204-7.

26. Lee, J.-H. *et al.* Production of human spinal-cord organoids recapitulating neural-tube morphogenesis. *Nat. Biomed. Eng* 1–14 (2022) doi:10.1038/s41551-022-00868-4.

27. Bamba, Y. *et al.* Generation of Induced Pluripotent Stem Cells and Neural Stem/Progenitor Cells from Newborns with Spina Bifida Aperta. *Asian Spine J* **11**, 870–879 (2017).

28. Sahakyan, V. *et al.* Folic Acid Exposure Rescues Spina Bifida Aperta Phenotypes in Human Induced Pluripotent Stem Cell Model. *Scientific Reports* **8**, 2942 (2018).

29. Anand, G. M. *et al.* Controlling organoid symmetry breaking uncovers an excitable system underlying human axial elongation. *Cell* (2023) doi:10.1016/j.cell.2022.12.043.

30. Balashova, O. A. *et al.* Noncanonical function of folate through folate receptor 1 during neural tube formation. *Nat Commun* **15**, 1642 (2024).

31. Abdel Fattah, A. R. *et al.* Actuation enhances patterning in human neural tube organoids. *Nat Commun* **12**, 3192 (2021).

32. Birtele, M. *et al.* Non-synaptic function of the autism spectrum disorder-associated gene SYNGAP1 in cortical neurogenesis. *Nat Neurosci* **26**, 2090–2103 (2023).

33. Juriloff, D. M. & Harris, M. J. Insights into the Etiology of Mammalian Neural Tube Closure Defects from Developmental, Genetic and Evolutionary Studies. *Journal of Developmental Biology* **6**, 22 (2018).

34. Iyer, N. R. *et al.* Modular derivation of diverse, regionally discrete human posterior CNS neurons enables discovery of transcriptomic patterns. *Sci. Adv.* **8**, eabn7430 (2022).

35. Lippmann, E. S. *et al.* Deterministic HOX Patterning in Human Pluripotent Stem Cell-Derived Neuroectoderm. *Stem Cell Reports* **4**, 632–644 (2015).

36. Haeussler, M. *et al.* Evaluation of off-target and on-target scoring algorithms and integration into the guide RNA selection tool CRISPOR. *Genome Biol* **17**, 148 (2016).

37. Harkness, T. *et al.* High-Content Imaging with Micropatterned Multiwell Plates Reveals Influence of Cell Geometry and Cytoskeleton on Chromatin Dynamics. *Biotechnol J* **10**, 1555–1567 (2015).

38. Knight, G. T., **Lundin, B. F.,** *et al.* Engineering induction of singular neural rosette emergence within hPSC-derived tissues. *eLife* **7**, e37549 (2018).

39. Shum, A. S. & Copp, A. J. Regional differences in morphogenesis of the neuroepithelium suggest multiple mechanisms of spinal neurulation in the mouse. *Anat Embryol (Berl)* **194**, 65–73 (1996).

40. Li, Z., Liu, F., Yang, W., Peng, S. & Zhou, J. A Survey of Convolutional Neural Networks: Analysis, Applications, and Prospects. *IEEE Transactions on Neural Networks and Learning Systems* **33**, 6999–7019 (2022).

41. van der Put, N. M. *et al.* Mutated methylenetetrahydrofolate reductase as a risk factor for spina bifida. *Lancet* **346**, 1070–1071 (1995).

42. Lei, Y. *et al.* Mutations in Planar Cell Polarity Gene SCRIB Are Associated with Spina Bifida. *PLoS One* **8**, (2013).

43. Frosst, P. *et al.* A candidate genetic risk factor for vascular disease: a common mutation in methylenetetrahydrofolate reductase. *Nat Genet* **10**, 111–113 (1995).

44. Lesko, A. C., Keller, R., Chen, P. & Sutherland, A. Scribble mutation disrupts convergent extension and apical constriction during mammalian neural tube closure. *Developmental Biology* (2021) doi:10.1016/j.ydbio.2021.05.013.

45. Lippmann, E. S., Estevez-Silva, M. C. & Ashton, R. S. Defined Human Pluripotent Stem Cell Culture Enables Highly Efficient Neuroepithelium Derivation Without Small Molecule

Inhibitors. *STEM CELLS* 1032–1042 (2017) doi:10.1002/stem.1622@10.1002/(ISSN)1549-4918.SpecialNeuralStemCellsVirtualIssue.

46. Molloy, A. M., Brody, L. C., Mills, J. L., Scott, J. M. & Kirke, P. N. The search for genetic polymorphisms in the homocysteine/folate pathway that contribute to the etiology of human neural tube defects. *Birth Defects Research Part A: Clinical and Molecular Teratology* **85**, 285–294 (2009).

47. Zhang, T. *et al.* Genetic Variants in the Folate Pathway and the Risk of Neural Tube Defects: A Meta-Analysis of the Published Literature. *PLoS ONE* **8**, e59570 (2013).

48. van der Put, N. M. *et al.* Decreased methylene tetrahydrofolate reductase activity due to the 677C-->T mutation in families with spina bifida offspring. *J Mol Med (Berl)* **74**, 691–694 (1996).

49. Boëda, B. & Etienne-Manneville, S. Spectrin binding motifs regulate Scribble cortical dynamics and polarity function. *eLife* **4**, e04726 (2015).

50. **Brady F. Lundin** et al. RosetteArray® Platform for Quantitative High-Throughput Screening of Human Neurodevelopmental Risk. bioRxiv 2024.04.01.587605 (2024) doi:10.1101/2024.04.01.587605

Chapter 4: Quantifying Neural Tube Defect Risk Within a Human Genetic Background

Introduction

With the establishment of the Rosette Array's capacity to conduct CNS regionally defined qHTS within a human genetic background, the fundamental goal of quantifying clinically relevant NTD risk factors becomes feasible. Early results demonstrated the predictive potential of the assay when considering pharmacologic NTD risk factors (**Figures 8 and 9**). However, these results had several shortcomings. First, a rescue of the disrupted rosette phenotype observed after folate pathway perturbation was not shown. Also, the experiments did not take advantage of the optimized caudal spinal conditions, limiting the scope of their capacity to explore regionally dependent risk perturbations. Next, the assay's ability to predict genetic risk factors, or the more clinically relevant multifactorial risk situation, was not explored. This was remedied by the creation of hPSC lines containing mutations known to increase clinical NTD risk within the WA09 parent line (**Figure 13**). This made possible, to our knowledge for the first time, the ability to conduct experiments with the goal of quantifying the specific risk contribution of an identified polymorphism. As such, we set out to explore the full investigative potential of the Rosette Array.

Since disruption of folate metabolism is the best known NTD-risk factor[1,2], Rosette Array detection of folate antagonism, along with rescue by active folate supplementation, was shown. Then, the Rosette Array platform's ability to quantify genetic and multifactorial causes for NTD risk in a sensitive, pathway specific, and region-specific manner was observed. Collectively, these results support the Rosette Array platform's utility for qHTS of chemical DNT and factors that cause increased NTD risk. More broadly, they indicate that Rosette Arrays could enable

efficient investigation of multifactorial neurodevelopmental disorder etiology as well as screening to discover precision medicine prophylactic and therapeutic approaches.

Experimental Methods

Experimental Contribution

Brady Lundin (B.F.L), Gavin Knight (G.T.K.), and Randolph Ashton (R.S.A.) took part in conception and design of all Rosette Array experiments and jointly interpreted all data. **B.F.L.** and G.T.K. performed all Rosette Array experimentation unless otherwise noted. Nisha Iyer (N.R.I.) aided in derivation of WA09 and SCRIB mutant cell banks. **B.F.L.**, G.T.K., N.J.F., Jack Maher (J.E.M.), and Madeline Cicero (M.R.C.) assisted with data acquisition and data analysis. Nicholas Izban (N.R.Iz.) and J.E.M. assisted with platform manufacturing, immunostaining, and imaging. Joshua Robinson (J.F.R.) and Bermans Iskandar (B.J.I.) assisted with design and interpretation of DNT and NTD experiments. The majority of these findings can be found in this submitted manuscript (**Brady F. Lundin** et al. RosetteArray® Platform for Quantitative High-Throughput Screening of Human Neurodevelopmental Risk. bioRxiv 2024.04.01.587605 (2024) doi:10.1101/2024.04.01.587605).

Culture Substrate Fabrication

12-well Rosette Array culture substrates were generated as previously described. 96-well Rosette Array substrates were purchased or obtained from Neurosetta.

Cell Culture

WA09 (H9, XX) hESC were supplied by the WiCell Research Institute. WA09 hESCs and the gene edited derivates were maintained at 37°C in 5% CO2 in E8 medium under feeder-free conditions on Matrigel (WiCell)-coated 6-well plates (Corning). For maintenance and expansion,

the cells were subcultured in Versene every 5 days at a 1:12 ratio following ~85% confluency. For cell line authentication, each cell line (WA09 parent and 5 edited clones) was submitted to WiCell for karyotyping and mycoplasma testing and results returned validated.

NMP Derivation

WA09 hESCs and gene-edited mutants were differentiated into cervical and lumbar NMPs as previously described in Chapter Three.

Cryopreservation and Thaw of hESC and NMPs

Confluent monolayers of WA09 hESCs and the gene edited derivates in 6-well plates were prepared for cryopreservation through enzymatic dissociation in Accutase (ThermoFisher) and resuspend at ~6,000,000 cells/mL in E8 medium with 10 μM ROCK inhibitor Y-27632 and 10% DMSO. WA09-derived NMPs were similarly dissociated in Accutase and resuspended in E6 medium at ~6,000,000 cells/mL with 10 μM ROCK inhibitor and 10% DMSO. Cryopreservation was performed in Cryovials (Wheaton, Ref#: W985922) at 1mL/vial using a Thermo Scientific CryoMed Controlled-Rate Freezer (7450) set to lower temperature at the following rates; -10°C/min to 4°C, -1°C/min to -60°C, and -10°C/min to -100°C. Cryopreserved vials of cells were placed in liquid nitrogen dewars for extended storage. Cells were thawed at 37°C for 3-5 mins and resuspended in E8 medium with 10 μM ROCK inhibitor for hESC seeding or E6 medium with 10 μM ROCK inhibitor and 1 μM RA for NMP seeding.

Dose-Response Developmental Neurotoxicity and 5-MTHFA Supplementation Testing

Use of the 96-well culture platform for DNT screen validation involved supplementation of the culture medium with the compound of interest upon removal of ROCK inhibitor after 1 day of seeding. Chemical compounds stocks were solubilized in DMSO or water and prepared from dry stock fresh for each experiment. Dose-response medium formulations were prepared through

serial dilutions in culture medium. Compound concentrations were doubled to account for 50% medium changes. Compounds solubilized in DMSO were controlled to medium conditions containing DMSO supplementation matching the highest tested concentration of DMSO in the treatment groups. For 5-MTHFA rescue experiments, the base media was prepared with 1.0µM methotrexate and serial dilutions were made from the 5-MTHFA stock.

Immunocytochemistry

On the last day of culture, Rosette Arrays were fixed in 4% paraformaldehyde (PFA) in PBS for ~15 minutes. Micropatterned tissues were permeabilized and blocked with 0.1% Triton-X and 5% Donkey serum in PBS (PBS-DT) for 1 hour at room temperature. Primary antibodies listed in the Key Resource Table were incubated on the substrates at 4°C overnight and at a 1:200 dilution in PBS-DT. This was followed by 3 x 20-minute washes with PBS-DT. Next, secondary antibodies listed in Key Resources Table were incubated on the substrates at 4°C overnight and at a 1:500 dilution in PBS-DT. This was followed by 2 x 20-minute washes with PBS-DT, and cell nuclei were stained with DAPI for 10 minutes in the last PBS wash.

Image Acquisition

A Nikon AR-1 Scanning Confocal Microscope was used to acquire all fluorescent images. Tissues were randomly selected to be imaged from each rosette array. Image acquisition was performed with a 10, 20, or 60X objective (Nikon) at 512x512 pixels, sampling 5-7 vertical image planes with 1.5 µm vertical spacing.

Image Analysis of Tissue Viability and Neural Induction

Image segmentation (CellProfiler, Harvard) was used to quantify the number of $DAPI^+$ and $Pax6^+$ cells per vertical image plane for each rosette. To minimize double counting of cells

between vertical planes, a single, middle image plane was used to generate a relative number of cells (# of $DAPI^+$ cells) per tissue and $\%Pax6^+$ (# of $Pax6^+$ cells / # of $DAPI^+$ cells).

Manual Characterization of Neural Rosette Emergence and Morphology

Rosette emergence was quantified through manual image analysis. For each of the tissues randomly imaged per array, a binary determination of singular rosette or failed single rosette emergence (i.e., no rosette or 2+ polarization foci present) was made. Neural rosettes in micropatterned tissues were identified by the presence of a coherent N-cadherin ring structure. Percent neural rosette emergence was calculated as # singular rosette/tissues per array. In single rosette tissue, rosette morphological characteristics were measured by outlining the boundary of the N-cadherin ring.

Non-linear Regression of Dose-Response

GraphPad Prism was used to calculate parameters associated with the Logistic Regression Model, plot sigmoidal dose-response curves, and analyze the curves' fit for different parameters plus calculation of the 95% CIs and R^2 values.

Calculation of the lowest-observed-adverse-effect level (LOAEL)

In the MTX dose-response experiment, %single neural rosette averages for each dose were compared to the experimental condition's solvent control via a Student's T-test within Excel. The first dose that was significantly different from the solvent control at a level of $p<0.05$ was considered the lowest-observed-adverse-effect level (LOAEL).

Quantitative real-time polymerase (qPCR) chain reaction and expression analysis

Total RNA was isolated using a TRIzol reagent (Invitrogen), and complementary DNA (cDNA) was synthesized using the SuperScript IV First-Strand Synthesis System (Invitrogen) according to the manufacturer's instructions. TaqMan Gene Expression Assays and TaqMan Gene

Expression Master Mix (Applied Biosystems) were used on a Bio-Rad CFX96 thermocycler with the following protocol: 50°C for 2 min; 95°C for 10 min; 40 cycles of 95°C for 15 s and 60°C for 1 min. Target genes were normalized to RPS18 expression, and relative gene expression was calculated using the comparative ▲Ct method. When fold differences are calculated and compared, RNA for each condition was collected in biologic triplicate and assayed in technical replicate and fold change (2^-▲Ct) in relative mRNA expression levels of target genes. Values are reported for each gene with SDs after testing for the data's lognormal distribution. Statistical analysis was conducted using GraphPad Prism software. Significance was determined using a one-way analysis of variance (ANOVA) with Tukey-Kramer post hoc test for multiple comparisons at a 95% confidence threshold.

Statistical Analysis

GraphPad Prism (V10.2.1) was used for all statistical analysis. Error bars represent mean ± SD; * for $p<0.05$, ** for $p<0.01$, *** for $p<0.001$, **** for $p<0.0001$. Neural rosette emergence for single dose experiments were analyzed with t-tests and all other metrics were analyzed with One-way ANOVAs. Non-linear regression was performed to generate three (Hill Slope =1) or four (Hill Slope not restrained) parameter dose-response curves depending on whether data points were present at the curve's inflection point. Comparison of dose-response curves for different metrics analyzing the same compound were compared using a hypothetical dose-response curve for all metrics. The explanation of "n" and the number of technical or biological replicates completed per experiment, as well as tests done to determine if data met assumptions of statistical approaches, can be found in the figure legends and text.

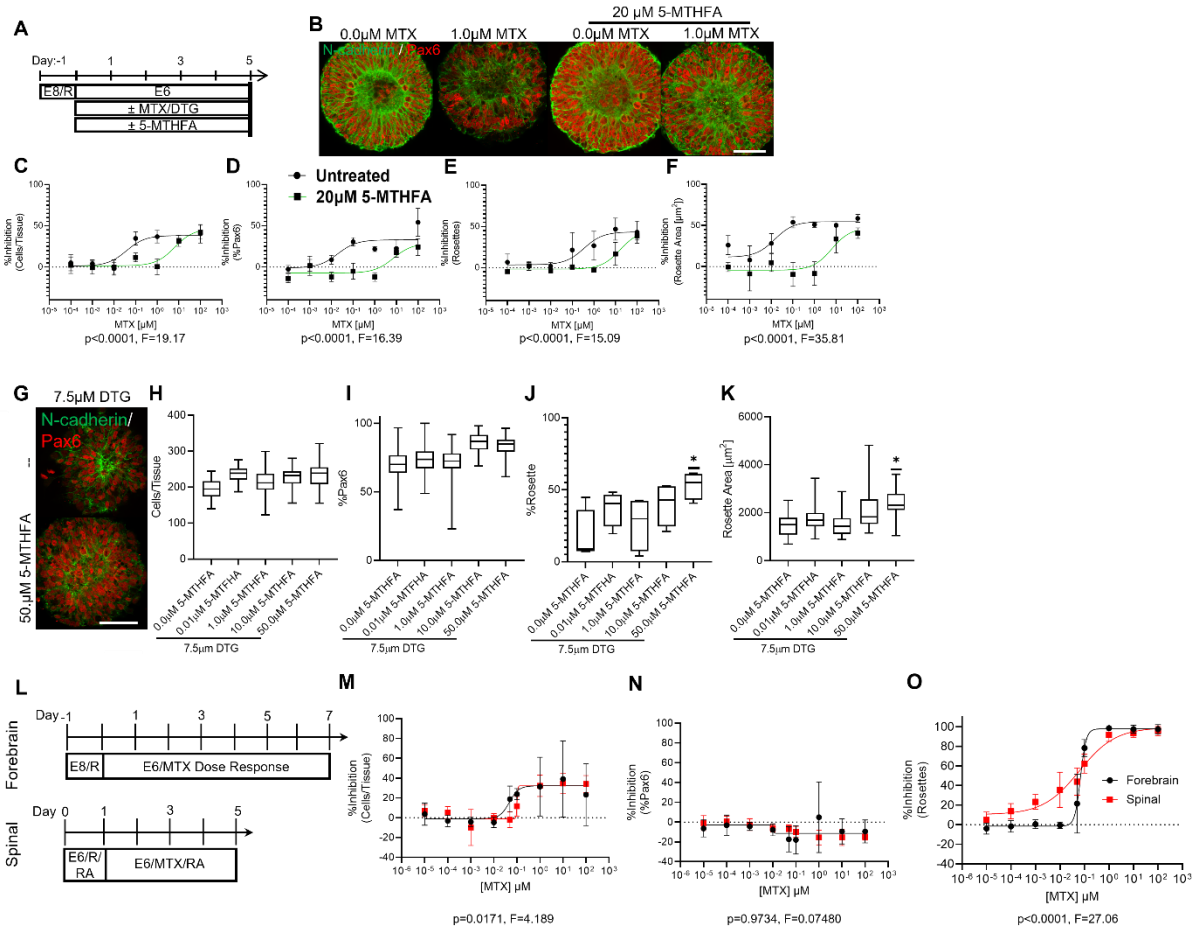

Figure 14. FB and SC Rosette Arrays detect folate metabolic pathway-specific risk with regional differences. (A) Culture schema for MTX/DTG exposure with 5-MTHFA rescue in 12-well FB RosetteArrays. (B) Inhibitory effect of 1.0 µM MTX on FB rosette emergence and rescue using concurrent 20.0 µM 5-MTHFA treatment. Quantification of MTX dose-response on 12-well FB Rosette Array derivation with 20.0 µM 5-MTHFA treatment across (C) cells/tissue, (D) neural induction, (E) single rosette emergence, and (F) rosette area metrics. Quantification of DTG's inhibitory effects on 12-well FB Rosette Array derivation with increasing 5-MTHFA supplementation across (H) cells/tissue, (I), neural induction, (J) single rosette emergence, and (K) rosette area metrics. (L) Culture schema for MTX dose-response comparison between 96-well FB and lumbar SC RosetteArrays. Dose-response curves of %inhibition of (M) cells/tissue (N) neural induction, and (O) single rosette emergence. (C-F, H-K) Each data point is the average of technical triplicate, n=50 tissues analyzed per well. (C-F) Three-parameter non-linear regression used to model and compare each metric. (H-K) Significance assessed using 1-way ANOVA with Tukey-Kramer post-hoc analysis, * $p \leq 0.05$. (M-O) Each data point is the average of two biological replicates, each dose in technical quadruplicate, n=40 tissues analyzed per well. Four-parameter non-linear regression used to model and compare each metric. If curves are statistically equivalent, then only one curve is displayed. Scale bars are 100 µm.

Results and Interpretation

Rosette Arrays detect chemical NTD risks specific to folate metabolic pathway inhibition

Of the NTD risk pathways surveyed in Figure 8, disruption of folic acid metabolism is the best known NTD risk factor[3]. Therefore, the Rosette Array platform's ability to detect folate metabolic pathway-specific NTD risk was interrogated further. First, we assessed the ability to rescue MTX inhibition of rosette emergence by supplementing with the metabolized form of folic acid, 5-methyltetrahydrafolic acid (5-MTHFA)[4]. 12-well FB Rosette Arrays were used to conduct a MTX dose-response in the absence and presence of 20μM 5-MTHFA (**Figure 14A-F and 15A, B**). In all metrics, the presence of 20 μM 5-MTHFA significantly shifted the dose-response curve to the right increasing IC_{50} values by greater >10-fold. This demonstrates folate metabolic pathway-specific rescue of MTX's Rosette Array inhibitory effects.

Next, the 12-well FB Rosette Assay was used to detect the NTD risk posed by Dolutegravir, a recently introduced HIV antiretroviral monotherapy. When taken periconceptionally, Dolutegravir has been shown to increase clinical NTD occurrence[5,6] presumably by antagonistically binding the folate receptor-1[4]. Moreover, its NTD risk effects can be negated by sufficient folate dietary supplementation[4,7]. In our FB Rosette Array dose-response, Dolutegravir inhibits all metrics similarly with a single rosette emergence IC_{50} of 3.19 μM (2.15-4.17μM, 95% CI), which is well within its therapeutic serum level of 3-10 μM[4] (**Figure 15C-G**). This is indicative of its presumed inhibition of folate receptor-1, which would inhibit vital folate metabolism required for basic cell physiology. Additionally, analogous to MTX, conducting the FB Rosette Array at 7.5 μM DTG with increasing 5-MTHFA concentrations showed a significant rescue in single rosette emergence and rosette area with non-

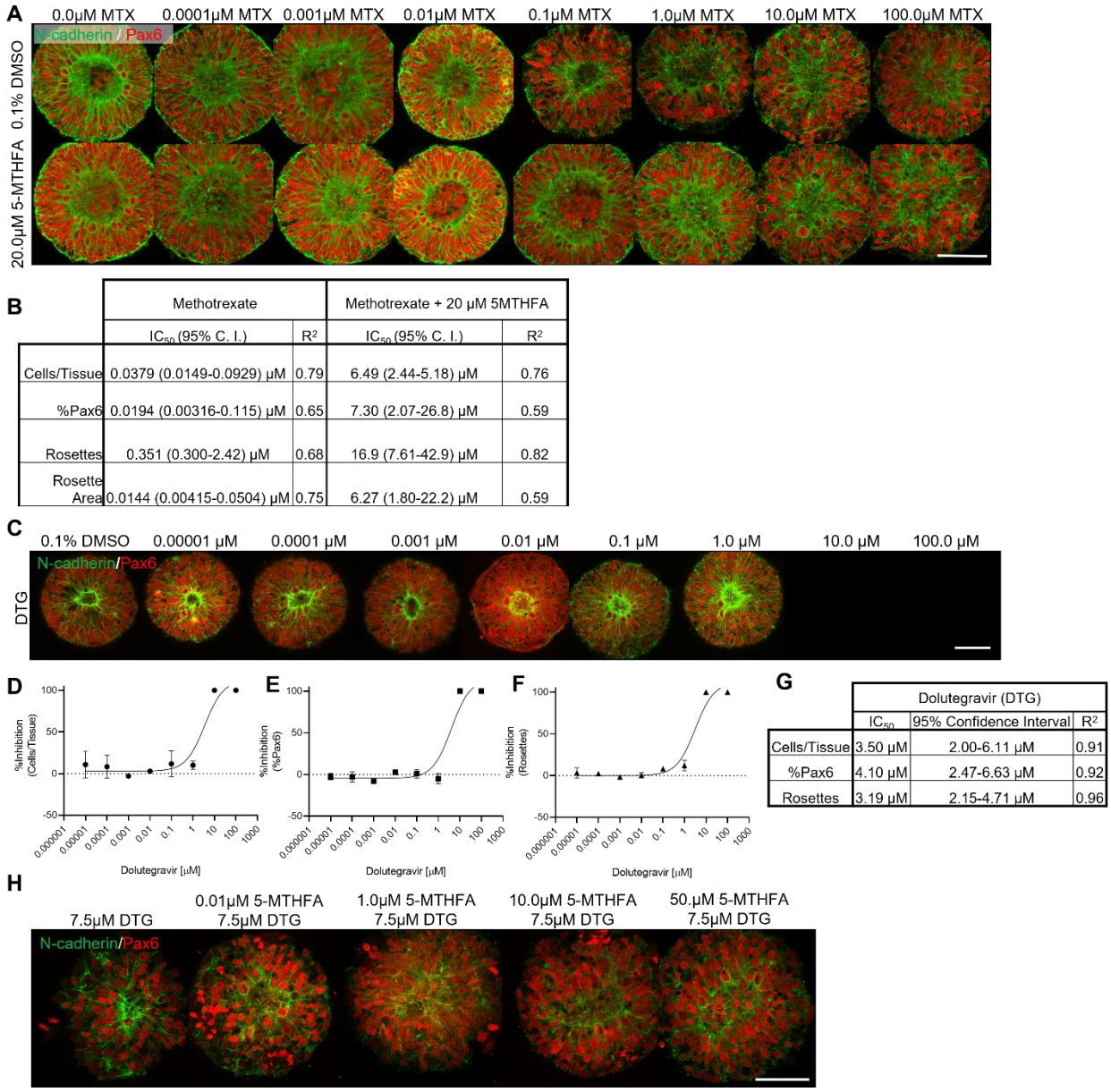

	Methotrexate		Methotrexate + 20 μM 5MTHFA	
	IC_{50} (95% C. I.)	R^2	IC_{50} (95% C. I.)	R^2
Cells/Tissue	0.0379 (0.0149-0.0929) μM	0.79	6.49 (2.44-5.18) μM	0.76
%Pax6	0.0194 (0.00316-0.115) μM	0.65	7.30 (2.07-26.8) μM	0.59
Rosettes	0.351 (0.300-2.42) μM	0.68	16.9 (7.61-42.9) μM	0.82
Rosette Area	0.0144 (0.00415-0.0504) μM	0.75	6.27 (1.80-22.2) μM	0.59

	Dolutegravir (DTG)		
	IC_{50}	95% Confidence Interval	R^2
Cells/Tissue	3.50 μM	2.00-6.11 μM	0.91
%Pax6	4.10 μM	2.47-6.63 μM	0.92
Rosettes	3.19 μM	2.15-4.71 μM	0.96

Figure 15. Folate metabolic pathway-specificity experimental images, dose-response curves, and descriptive stats.

(A) Confocal images of representative 12-well FB Rosette Array tissues at each MTX concentration with and without 5-MTHFA supplementation. (B) Descriptive stats for dose-response curves displayed in Figure 14C-F. (C) Representative images of DTG dose-response on 12-well FB Rosette Array derivation with %inhibition curves of (E) cells/tissue, (E) neural induction, and (F) single rosette formation with (G) descriptive statistics for each curve. Experiment conducted with technical triplicate, n=50 tissues analyzed per well. (H) Representative images of 7.5 μM DTG-exposed FB Rosette Array tissues with increasing 5-MTHFA concentrations. Each data point is the average of technical triplicates, n=50 tissues analyzed per well. Three-parameter non-linear regression used to model and compare each metric. Scale bars are 100 μm.

significant but increasing trends in cell viability/proliferation and neural induction metrics (**Figure 14G-K**). Collectively, these results demonstrate that the FB Rosette Array can detect folate metabolic pathway-specific NTD risk associated with both MTX's inhibition of the pathway's dihydrofolate reductase enzyme and DTG's inhibition of folate receptor-1 binding[4].

Due to previous regional differences in Rosette Array responses to VPA (**Figure 9**), FB and lumbar SC Rosette Array detection of MTX's NTD risk was compared using the 96-well plate format (**Figure 14L-O**). Relative to the 12-well assay, the 96-well FB Rosette Array showed increased sensitivity to MTX's inhibitory effects with a >5-fold decrease in the single rosette emergence IC50 value, i.e., 0.069 μM (0.062-0.076 μM, 95% CI) vs. 1.4 μM (0.61-3.83 μM, 95% CI) vs. 0.351 μM (0.3-2.42 μM, 95% CI) (**Figure 14O, 8O, 14E, respectively**). Also, maximal inhibition of single rosette emergence was observed at ~1 μM vs. >100 μM in the 96- vs. 12-well FB Rosette Array formats (**Figures 8O, 14O**). When evaluating the 96-well plate format's regional differences, the lumbar SC Rosette Array had a statically equivalent IC_{50}, i.e., 0.61 μM (0.035-0.10 μM, 95% CI), to the FB Rosette Array, i.e., 0.69 μM (0.062-0.76 μM, 95% CI). Yet, its Lowest Observed Adverse Effect Level (LOAEL) was 500-fold lower than the FB Rosette Array, i.e., 0.1 nM (SC) vs 0.5 μM (FB) (**Figure 14O**). Moreover, above the IC_{50}, MTX inhibited single rosette emergence in SC and FB Rosette Arrays similarly, but below the IC_{50}, SC tissues appeared more prone to form 2+ versus no rosettes per tissue in response to MTX (**Figures 16A-C**). Again, this highlights regional differences between rosette emergence mechanisms in FB vs. SC Rosette Arrays mirroring presumed differences between regional NTD mechanisms in vivo[8].

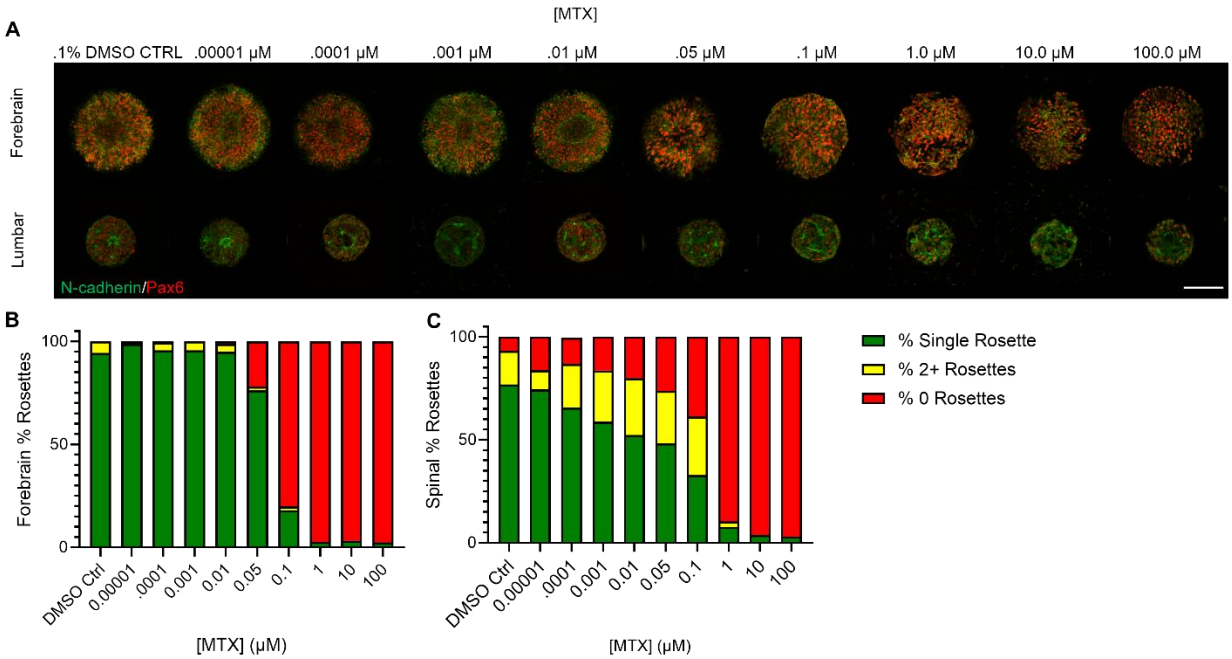

D

	Forebrain			Lumbar		
	IC_{50} (95% C. I.)	Hill Slope (95% C.I)	R^2	IC_{50} (95% C. I.)	Hill Slope (95% C.I)	R^2
Cells/Tissue	0.0474 (0.0228-0.0956) µM	2.131 (0.784-)	0.37	0.102 µM	--	0.69
%Pax6	0.4217 (--) µM		0.10	0.01044 (--) µM	--	0.10
Rosettes	0.0688 (0.0623-0.0762) µM	3.76 (2.84-4.97)	0.95	0.0612 (0.0345-0.1027) µM	0.589 (0.391-0.886)	0.91

Figure 16. 96-well FB and SC Rosette Array-MTX dose-response images and descriptive stats. (A) Confocal images of representative 96-well FB and lumbar SC Rosette Array tissues at each concentration of MTX. % rosette counts per tissue at each dose of MTX for (B) FB and (C) lumbar SC Rosette Arrays. Experiments conducted in technical quadruplicate, n=40 tissues analyzed per well. (D) Descriptive stats for curves displayed in Figure 14M-O. Scale bars are 100 µm.

Rosette Arrays detect genetic and multifactorial NTD risks within the folate pathway

To begin assessing the Rosette Array platform's sensitivity to NTD risk caused by the MTHFR$^{C677T(-/-)}$ variant, the MTHFR$^{C677T(+/-)}$ WA09 parent line and homozygous clones #4 and #9 were screened using 12-well FB Rosette Arrays. The media used in the assay already contains 9 µM folic acid. Therefore, this initial screen was run using control, 1 µM MTX, and 1 µM MTX plus 20 µM 5-MTHFA media conditions (**Figure 17A, B**). Of note, this experiment simulates a multifactorial NTD risk scenario, where the risk additive combination of the MTHFR^{C677T} genetic variant and MTX exposure simulating a folate stressed environment are being modeled.

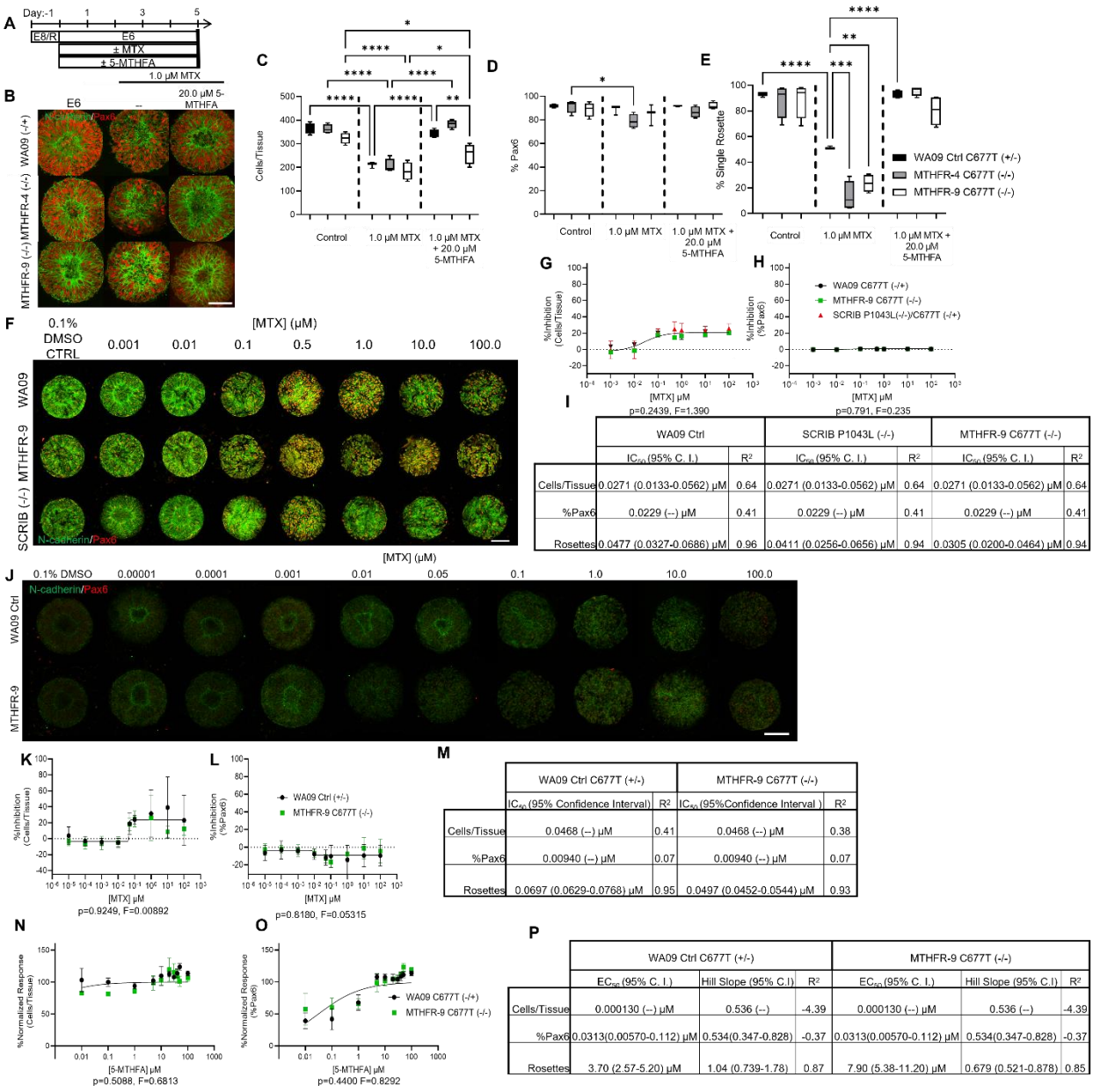

	WA09 Ctrl		SCRIB P1043L (-/-)		MTHFR-9 C677T (-/-)	
	IC_{50} (95% C. I.)	R^2	IC_{50} (95% C. I.)	R^2	IC_{50} (95% C. I.)	R^2
Cells/Tissue	0.0271 (0.0133-0.0562) µM	0.64	0.0271 (0.0133-0.0562) µM	0.64	0.0271 (0.0133-0.0562) µM	0.64
%Pax6	0.0229 (--) µM	0.41	0.0229 (--) µM	0.41	0.0229 (--) µM	0.41
Rosettes	0.0477 (0.0327-0.0686) µM	0.96	0.0411 (0.0256-0.0656) µM	0.94	0.0305 (0.0200-0.0464) µM	0.94

	WA09 Ctrl C677T (+/-)		MTHFR-9 C677T (-/-)	
	IC_{50} (95% Confidence Interval)	R^2	IC_{50} (95%Confidence Interval)	R^2
Cells/Tissue	0.0468 (--) µM	0.41	0.0468 (--) µM	0.38
%Pax6	0.00940 (--) µM	0.07	0.00940 (--) µM	0.07
Rosettes	0.0697 (0.0629-0.0768) µM	0.95	0.0497 (0.0452-0.0544) µM	0.93

	WA09 Ctrl C677T (+/-)			MTHFR-9 C677T (-/-)		
	EC_{50} (95% C. I.)	Hill Slope (95% C.I)	R^2	EC_{50} (95% C. I.)	Hill Slope (95% C.I)	R^2
Cells/Tissue	0.000130 (--) µM	0.536 (--)	-4.39	0.000130 (--) µM	0.536 (--)	-4.39
%Pax6	0.0313(0.00570-0.112) µM	0.534(0.347-0.828)	-0.37	0.0313(0.00570-0.112) µM	0.534(0.347-0.828)	-0.37
Rosettes	3.70 (2.57-5.20) µM	1.04 (0.739-1.78)	0.87	7.90 (5.38-11.20) µM	0.679 (0.521-0.878)	0.85

Legend at top of next page.

No difference between lines in any metric is observed under control FB Rosette Array conditions **(Figure 17C-E**). However, upon challenging with 1 µM MTX, all lines showed a statistically significant decrease in cell viability/proliferation and single rosette emergence metrics. Yet, both MTHFR$^{C677T(-/-)}$ clones demonstrated significantly increased MTX sensitivity in single rosette emergence, i.e., 13.62 ± 11.27% (Clone #4) and 23.47 ± 6.81% (Clone #9), compared to the MTHFR$^{C677T(+/-)}$ parent line, i.e., 51.50 ± 1.06%. This effect appears to be folate metabolic

Figure 17. FB Rosette Array detection of folate metabolic pathway-specific genetic NTD risk: preliminary multifactorial scenario data, data, experimental images, dose-response curves, and descriptive stats.

(A) Culture schema for FB Rosette Array 20mM 5-MTHFA rescue of MTHFR$^{C677T\ (-/-)}$ mutant lines and their MTHFR$^{C677T\ (+/-)}$ WA09 parent control under 1 mM MTX with (B) representative staining and quantification of (C) cells/tissue, (D) %Pax6, (E) %single rosette emergence. n=4 technical replicates, 50 tissues analyzed per well. Significance assessed using 1-way ANOVA with Tukey-Kramer post-hoc analysis. (F) Representative immunostaining, %inhibition curves of (G) Cells/Tissue and (H) %Pax6, and (I) descriptive stats for these curves and the %single rosette emergence curve from Figure 18B. (J) Representative immunostaining, %inhibition curves of (K) Cells/Tissue and (L) %Pax6, and (M) descriptive stats for these curves and the %single rosette emergence curve from Figure 18C. %Normalized response curves of (N) Cells/Tissue and (O) %Pax6, and (P) descriptive stats for these curves and the % normalized single rosette emergence curve from Figure 18F. Each data point on a dose-response curve is the average of technical quadruplicate, n=40 tissues analyzed per well. Four-parameter non-linear regression used to model and compare each metric. If curves are statistically equivalent, then only one curve is displayed. *$p \leq 0.05$, *** $p \leq 0.001$. Scale bars are 100 μm.

pathway specific since supplementation with 20 μM 5-MTHFA, in the presence of 1 μM MTX, rescued the risk phenotype in all lines.

To further clarify whether the prior results were due to a folate metabolic pathway-related sensitivity, a full MTX dose-response in a 96-well FB Rosette Array was conducted comparing the MTHFR$^{C677T(+/-)}$ parent line, MTHFR$^{C677T(-/-)}$ clone #9, the MTHFR$^{C677T(+/-)}$/ SCRIB$^{P1043L(-/-)}$ clone #52 (**Figures 17F-I and 18A,B**). Each lines' dose-response yielded statistically different curves with the MTHFR$^{C677T(-/-)}$ clone #9's IC_{50} of 0.0305 μM (0.0200-0.0464 μM 95% CI) being lower than the MTHFR$^{C677T(+/-)/}$ SCRIB$^{P1043L(-/-)}$ clone #52's and MTHFR$^{C677T(+/-)}$ parent line's IC_{50}s of 0.0411 μM (0.0256-0.0656 μM 95% CI) and 0.0477 μM (0.0327-0.0686 μM 95% CI), respectively. For increased accuracy, a second MTX dose-response between the MTHFR$^{C677T(-/-)}$ clone #9 and its MTHFR$^{C677T(+/-)}$ parent line was conducted with additional dosages around the previously observed IC_{50} values and in biological duplicate (**Figures 17J-M and 18C**). Again, each lines' dose-response yielded statistically different curves but now without overlapping IC_{50} values, i.e., Clone #9- 0.0497 μM (0.0452-0.0544 μM 95% CI) vs. WA09 parent- 0.0697 μM (0.0629-0.0768 μM 95% CI). Additionally, a 5-MTHFA rescue dose-response in the presence of

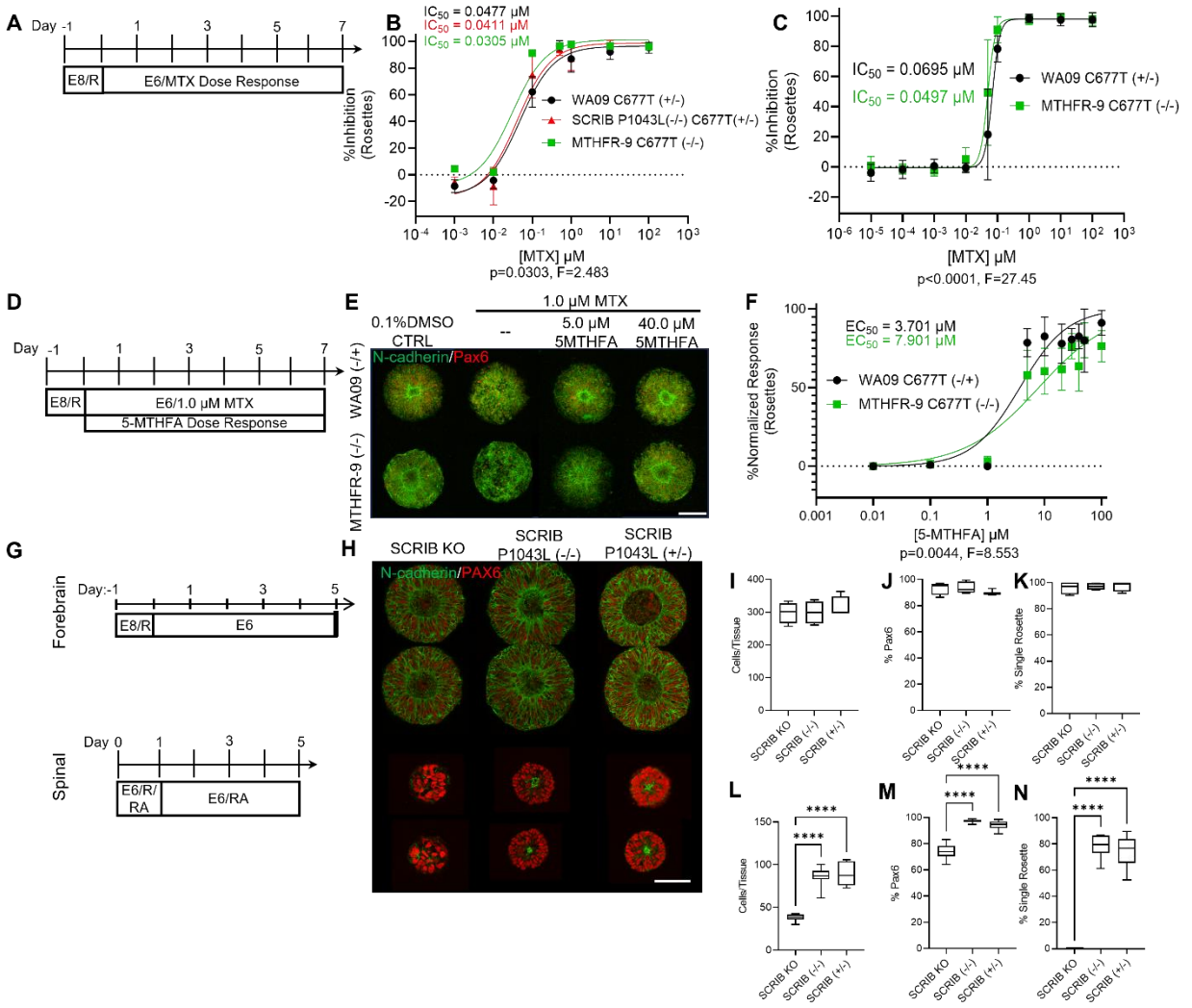

Figure 18. Rosette Arrays detect clinically relevant genetic and multifactorial NTD risks. (A) Culture schema for (B) initial and (C) secondary FB Rosette Array MTX dose-response comparison of single rosette emergence across MTHFR$^{C677T(-/-)}$ and SCRIB$^{P1043L(-/-)/C677T(+/-)}$ mutant lines and the WA09$^{C677T(+/-)}$ isogenic control. (D) Culture schema for 5-MTHFA dose-response rescue of MTHFR$^{C677T(-/-)}$ mutant line and the WA09$^{C677T(+/-)}$ isogenic control under 1mM MTX exposure with (E) representative staining and (F) quantification of %normalized single rosette emergence. Each data point on a dose-response curve is the average of technical quadruplicate, n=40 tissues analyzed per well. Four-parameter non-linear regression used to model and compare each metric. (G) Culture schema for FB and cervical SC RosetteArrays of SCRIB$^{P1043L(+/-)}$, SCRIB$^{P1043L(-/-)}$, SCRIB^{KO} mutant lines with (H) representative immunostaining and FB (I-K) and SC (L-N) quantification for cells viability/proliferation, neural induction, and % single rosette emergence. Data represents two biologic replicates with n=6-7 technical replicates total. Data is compared via a 1-way ANOVA with Tukey-Kramer post-hoc analysis. **** $p \leq 0.0001$. Scale bars are 100µm.

1 µM MTX showed that the MTHFR$^{C677T(-/-)}$ clone #9 required more folate supplementation, i.e., EC_{50} of 7.90 µM (5.38 -11.20 µM 95% CI), than the MTHFR$^{C677T(+/-)}$ parent line, i.e., EC_{50} of 3.70 µM (2.57 -5.20 µM 95% CI) to rescue its risk phenotype (**Figures 17N-P and 18D-F**).Thus,

it is clear that the MTHFR$^{C677T(-/-)}$ line's increased sensitivity to folate metabolic pathway perturbation is due to its additional c.C677T mutation compared to the MTHFR$^{C677T(+/-)}$ parent line. Moreover, this highlights the Rosette Array platform's ability to quantify a genetic NTD risk factor in a multifactorial scenario.

Rosette Arrays detect CNS region dependent NTD risk within the planar cell polarity pathway

To model PCP pathway-induced NTD risk, SCRIB$^{P1043L(+/-)}$, SCRIB$^{P1043L(-/-)}$, and SCRIB^{KO} lines were generated and cryopreserved as both hESC and cervical spinal NMP banks along with the WA09 parent line (**Figure 19A**). In 12-well FB Rosette Array assays, no difference was observed between the 3 mutant lines despite immunostaining showing FB rosette formation in the absence of SCRIB protein for the knockout mutant (**Figures 18G-K and 19B**). Yet, in the 12-well cervical SC Rosette Array, there was complete abrogation of rosette emergence accompanied by a significant decrease in cell viability/proliferation and neural induction in the SCRIB^{KO} line compared to the SCRIB$^{P1043L(+/-)}$ and SCRIB$^{P1043L(-/-)}$ lines (**Figure 18G, H, L-M**). This regional NTD risk phenomenon in the SCRIB^{KO} line comports with the SCRIB^{Crc} mouse[9] and human[10] presentation of craniorachischisis (CRN), which is a failure of neural tube closure across the neuraxis except for the rostral forebrain[11]. Also, despite SCRIB's p.P1043L mutation in its third PDZ domain, immunostaining showed apical co-localization of SCRIB and F-Actin (phalloidin) in both FB and cervical SC rosettes (**Figure 19B**). However, SCRIB^{KO} rosettes showed F-Actin apical polarization in FB Rosettes despite minimal-to-no SCRIB immunostaining, and no F-actin polarization in cervical SC rosettes. In mice, others have

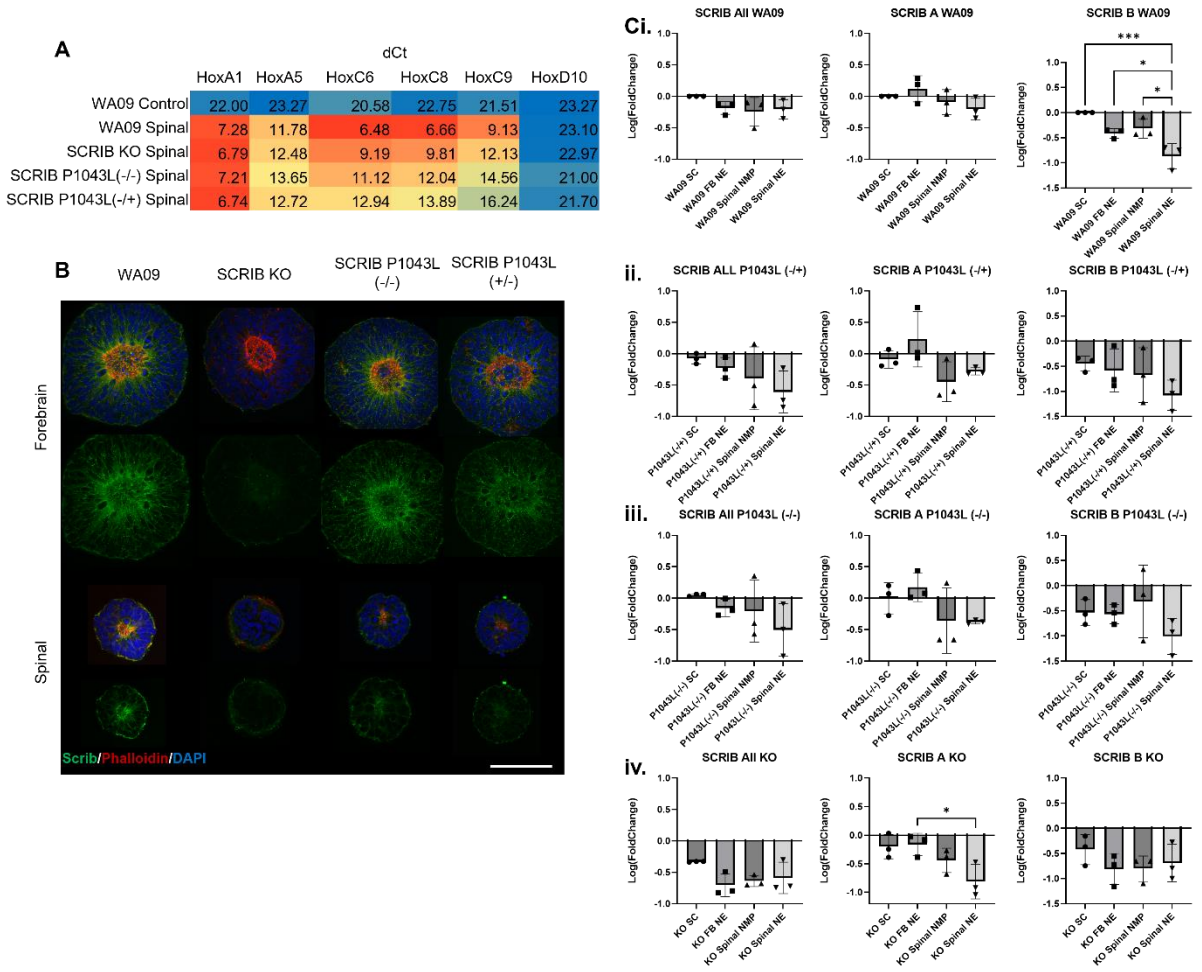

Figure 19. FB and cervical SC Rosette Array detection of PCP pathway genetic NTD risks: qPCR and immunostaining data.

(A) ▲-Ct values for HOX gene expression in cervical spinal NMPs used to generate Rosette Arrays in Figure 18G-N. (B) Additional representative immunostaining for SCRIB and F-actin (Phalloidin) in FB and SC rosette tissues. (C) qPCR of stem cell (SC), FB neuroectoderm (NE), spinal NMP, and spinal neuroectoderm (NE) cell states for total SCRIB and isoforms A/B expression across the (i) WA09 parent, (ii) $SCRIB^{P1043L(+/-)}$, (iii) $SCRIB^{P1043L(-/-)}$, and (iv) $SCRIB^{KO}$ lines normalized to WA09 SC expression levels. Data represents biologic triplicates each with technical duplicate, and distribution confirmed to be lognormal via GraphPad Prism analysis. Comparison via one-way ANOVA with Tukey-Kramer post-hoc analysis. Scale bar is 100 µm.

observed that SCRIB mutations, which lower expression ($SCRIB^{rumz/rumz}$), causing CRN, also cause decreased apical immunostaining of F-actin and other tight junction proteins in defect presenting regions[9].

This striking R/C regional difference led us to investigate expression of SCRIB isoforms in FB and cervical SC rosette tissues. In humans, SCRIB has two isoforms (A and B) with

SCRIB A containing a c-terminal AbLIM domain that links the protein to F-actin through binding b spectrins[12] (**Figure 13C**). Using qPCR for all SCRIB and its isoforms across the WA09 parent and the SCRIB mutant lines, we observed a decreasing trend in expression of all SCRIB and isoform B as cells transitioned from hESC to FB NEC and SC NMP and NEC states (**Figure 19C**). However, the SCRIB A isoform displayed a unique increase in FB NECs in all lines except for the $SCRIB^{KO}$, further confirming its knockout status. Overall, this data suggests a FB-SC regional difference in the importance of SCRIB for NEC apical-basal polarization that motivates further investigation. Additionally, it again highlights potential R/C regional differences in NTD mechanisms and motivates NTD risk assessment across the neuraxis as provided by the Rosette Array platform.

Discussion and Conclusions

The Rosette Array platform standardizes morphogenesis of hPSCs into forebrain and spinal single rosette tissues[13], thereby providing a predictable analogue of human neural tube emergence for screening applications. To our knowledge, it's the first hPSC-derived rosette/neural tube morphogenesis assay that can be generated using direct seeding of cryopreserved cells, thereby enabling an off-the-shelf assay[14–17] (**Figure 5**). Our results demonstrate its promise as a human neurodevelopmental risk assessment tool for modeling NTD risk factors. We showed that the platform, using both FB and SC Rosette Arrays, can reliably detect environmental/chemical, genetic, and multifactorial NTD risk factors (**Figures 8,9 14, 18**). Interestingly, some NTD risk factors demonstrated region-specific perturbations of rosette morphogenesis (**Figures 9, 14O, 18G-N**), indicating the importance of encompassing diverse neuraxial regions in neural tube formation screening assays. Lastly, with scaling to a 96-well

plate format plus AI-based image analysis (**Figure 10**), the Rosette Array platform enables off-the-shelf, qHTS of broad human neurodevelopmental risk as demonstrated here and elsewhere for Autism Spectrum Disorder[18].

NTDs are well known to have environmental, mono/polygenic, and multifactorial etiologies, which have historically been investigated using mouse models[19]. This approach has and continues to provide fundamental insights. Yet, it has inherent translational and experimental limitations. Translational limitations caused by differences between mice and humans include genomic sequence/architecture, number of neural tube closure points, and the fact that mouse models predominantly display cranial defects versus spina bifida defects being the majority of human cases[8,20]. Experimentally, the limited number of mouse strains used to create NTD models impedes exploration of how population variation affects polygenic etiology[8,21]. Also, experimental possibilities are limited by the sheer number of mice required to demonstrate the rate of NTD occurrence. For example, Tukeman et al. required the use of 169 dams/1302 fetuses in order to observe 7 NTD cases and demonstrate the folate-responsive NTD risk associated with periconceptional DTG administration[7].

The Rosette Array platform helps to address these limitations by providing a hPSC-derived analog of FB and SC neural tube emergence, which display regional differences in morphogenesis[13] (**Figures 5D, 10D, H, 12**) and NTD risk responses (**Figures 9, 14O, 16. 18G-N**) that may be indicative of known difference in neural tube closure mechanisms[8]. Using FB Rosette Arrays, DTG's folate-responsive NTD risk was detected at therapeutic serum levels (**Figure 14G-K, 15C-G**), further supporting clinical[6] and rodent studies[4]. Also, since the platform can be derived using iPSC lines[18], it could enable population variation studies to, for example, elucidate polygenic and multifactorial etiologies underlying $MTHFR^{C677T}$ penetrance in

NTD cases. Using just two FB Rosette Array 96-well plates (biological replicates), we observed an increased NTD risk (TC vs. TT IC_{50} ratio = 1.40) associated with $MTHFR^{C677T}$ homo- vs. heterozygosity in the WA09 genetic background (**Figure 18C**). A finding recapitulated in meta-analysis of 19 different clinical studies with ~6438 participants that yielded a TC vs. TT odds ratio of 1.427 (1.247-1.634, 95% CI)[22]. While IC_{50} ratios and odds ratios are not comparable, it does support further use of the Rosette Array platform for conducting NTD etiology studies to investigate population variance. Coupled with the platform's facilitation of novel in vitro observation of $SCRIB^{KO}$'s R/C region-specific NTD risk phenomena, which is clinically associated with CRN[10], Rosette Array technology could have a transformative impact on investigating human NTD etiology, despite lacking non-neural components that surround the emergent neural tube in vivo (**Figure 8Q-T**)[15,23]. Moreover, its scalable application to elucidating the etiology of other NDDs and for qHTS of precision medicine therapeutics to prevent or mitigate such diseases warrants further exploration.

Bibliography

1. Copp, A. J., Greene, N. D. E. & Murdoch, J. N. The genetic basis of mammalian neurulation. *Nat Rev Genet* **4**, 784–793 (2003).

2. Prevention of neural tube defects: results of the Medical Research Council Vitamin Study. MRC Vitamin Study Research Group. *Lancet* **338**, 131–137 (1991).

3. Fleming, A. & Copp, A. J. Embryonic folate metabolism and mouse neural tube defects. *Science* **280**, 2107–2109 (1998).

4. Cabrera, R. M. *et al.* The antagonism of folate receptor by dolutegravir: developmental toxicity reduction by supplemental folic acid. *AIDS* **33**, 1967–1976 (2019).

5. Zash, R., Makhema, J. & Shapiro, R. L. Neural-Tube Defects with Dolutegravir Treatment from the Time of Conception. *N Engl J Med* **379**, 979–981 (2018).

6. Zash, R. *et al.* Neural-Tube Defects and Antiretroviral Treatment Regimens in Botswana. *N. Engl. J. Med.* **381**, 827–840 (2019).

7. Tukeman, G. L. *et al.* Dolutegravir-induced neural tube defects in mice are folate responsive. *AIDS* **38**, 439–446 (2024).

8. Juriloff, D. M. & Harris, M. J. Insights into the Etiology of Mammalian Neural Tube Closure Defects from Developmental, Genetic and Evolutionary Studies. *Journal of Developmental Biology* **6**, 22 (2018).

9. Lesko, A. C., Keller, R., Chen, P. & Sutherland, A. Scribble mutation disrupts convergent extension and apical constriction during mammalian neural tube closure. *Developmental Biology* (2021) doi:10.1016/j.ydbio.2021.05.013.

10. Robinson, A. *et al.* Mutations in the planar cell polarity genes CELSR1 and SCRIB are associated with the severe neural tube defect craniorachischisis. *Hum Mutat* **33**, 440–447 (2012).

11. Jones, V. J., Greene, N. D. E. & Copp, A. J. Genetics and Developmental Biology of Closed Dysraphic Conditions. in *Occult Spinal Dysraphism* (eds. Tubbs, R. S., Oskouian, R. J., Blount, J. P. & Oakes, W. J.) 325–344 (Springer International Publishing, Cham, 2019). doi:10.1007/978-3-030-10994-3_21.

12. Boëda, B. & Etienne-Manneville, S. Spectrin binding motifs regulate Scribble cortical dynamics and polarity function. *eLife* **4**, e04726 (2015).

13. Knight, G. T. , **Lundin, B. F.,** *et al.* Engineering induction of singular neural rosette emergence within hPSC-derived tissues. *eLife* **7**, e37549 (2018).

14. Tidball, A. M. *et al.* Deriving early single-rosette brain organoids from human pluripotent stem cells. *Stem Cell Reports* **18**, 2498–2514 (2023).

15. Karzbrun, E. *et al.* Human neural tube morphogenesis in vitro by geometric constraints. *Nature* **599**, 268–272 (2021).

16. Xue, X. *et al.* A Patterned Human Neural Tube Model Using Microfluidic Gradients. *Nature* (2024) doi:10.1038/s41586-024-07204-7.

17. Dreser, N. *et al.* Development of a neural rosette formation assay (RoFA) to identify neurodevelopmental toxicants and to characterize their transcriptome disturbances. *Arch Toxicol* **94**, 151–171 (2020).

18. Birtele, M. *et al.* Non-synaptic function of the autism spectrum disorder-associated gene SYNGAP1 in cortical neurogenesis. *Nat Neurosci* **26**, 2090–2103 (2023).

19. Wallingford, J. B., Niswander, L. A., Shaw, G. M. & Finnell, R. H. The Continuing Challenge of Understanding, Preventing, and Treating Neural Tube Defects. *Science* **339**, (2013).

20. Y, W., S, P., Rh, F. & Y, Z. Organoids as a new model system to study neural tube defects. *FASEB journal : official publication of the Federation of American Societies for Experimental Biology* **35**, (2021).

21. Chen, Z. *et al.* Threshold for neural tube defect risk by accumulated singleton loss-of-function variants. *Cell Research* **28**, 1039–1041 (2018).

22. Tabatabaei, R. S. *et al.* Association of Fetal MTHFR C677T Polymorphism with Susceptibility to Neural Tube Defects: A Systematic Review and Update Meta-Analysis. *Fetal Pediatr Pathol* 1–17 (2020) doi:10.1080/15513815.2020.1775734.

23. Pai, Y.-J. *et al.* Epithelial fusion during neural tube morphogenesis. *Birth Defects Research Part A: Clinical and Molecular Teratology* **94**, 817–823 (2012).

24. **Brady F. Lundin** et al. RosetteArray® Platform for Quantitative High-Throughput Screening of Human Neurodevelopmental Risk. bioRxiv 2024.04.01.587605 (2024) doi:10.1101/2024.04.01.587605

Chapter 5 – Perspectives and Future Work

Our understanding of human neural tube defect formation, and more broadly human neurodevelopment, remains incomplete. This is in large part due to the inherent difficulty of studying the nascent human CNS. Animal models and genome wide association studies (GWAS) of the human population have greatly aided our understanding of the many intricate pathways at play during normal and perturbed development, yet their inefficiency at identification of causative mechanisms of human NTDs highlights a recognized limitation of our current investigative approaches[1]. As such, many understand that another generated mouse NTD model, a more encompassing GWAS, or widespread whole genome sequencing of affected patients, will likely not result in the identification of singular causative genes, previously unrecognized contributory linear pathways, or a ubiquitous environmental antagonist that completes our understanding of persisting NTD occurrences.

Instead, medicine and developmental biology have broadly identified the phenomenon that the "many intricate pathways at play" are highly interdependent and sensitive to disruption from a medley of risk factors, with an undefined critical threshold of disruption resulting in disease and/or developmental failure. The combinatorial environmental and genetic risk factors that contribute to this critical threshold and result in a characterized disease and/or collection of diseases have received an umbrella term: "multifactorial etiologies". Collectively, the encompassing effect of an individual's environment on their inherited genetic machinery and the resultant impact on gene and protein expression and function, and subsequent whole organ development and function, describes a disease's multifactorial etiology. This understanding of disease formation has developed in conjunction with our understanding of the vast spatiotemporal gene expression changes that occur during embryonic development, and the

impact that not only metabolic and genomic, but also epigenomic[2], factors have on this orchestrated expression landscape. Neural tube defects and their unclear multifactorial etiologies present an interesting case study of this phenomenon, and an argument for why human specific models provide promising alternative investigative approaches.

As previously stated, 400+ NTD causing candidate genes have been identified from model organisms, however only genes affecting the folate metabolic and planar cell polarity (PCP) pathways are known to contribute to human disease[1]. Additionally, no single gene has been identified that consistently causes isolated human neural tube defects[3], yet 200+ different genes in mice cause NTDs when individually inactivated[4]. Furthermore, disruptions to the candidate genes that do cause murine and human disease often present differently, i.e. rostral exencephaly versus isolated caudal spina bifida[4]. Some have argued that this presentation difference is academic, and that to study the genesis of NTDs between species is to study equivalent phenomenon. The evidence, including evidence generated in this thesis, seems to suggest otherwise.

The morphogenetic differences in R/C regions of the developing neural tube was first described in mice[5]. Regional differences of neuroectodermal morphology, cell behavior, and expressed genes have since been studied extensively[6], including recent single cell RNA sequencing of cells that represent the developing neuraxis in mice[7] and hPSC-derived human NMPs[8]. These results make clear the existence of regionally distinct transcriptional programs that create the vast diversity of the CNS. The activation of these unique programs can be employed by *in vitro* differentiation techniques[8,9] to generate regionally distinct tissues[10,11] which are the morphogenetic origins of the more matured CNS[12,13]. Harnessing this capability, our results clearly demonstrate the differential sensitivity these regionally distinct tissues exhibit to

multiple environmental and genetic risk factors. Interestingly, PCP perturbation predicted regional defects congruent with mice models[14], while folate disruption suggested a greatly increased sensitivity within the spinal region, mirroring clinical spina bifida presentation[15], but in direct contrast to rostral defects seen in folate disrupted mice.[16,17] . Thus, the question becomes what critical threshold of disruption is met that causes these defects to occur, and why do species differences arise for one investigated pathway, but not another.

While the NTD field has been focused on answering this line of questioning for over three decades, definitive answers remain elusive. However, the existence of two categories of NTD formation scenarios have been recognized: folate-responsive versus folate-resistant, regarding a defect's ability to be abrogated with proper folate supplementation[18]. Notably, despite the widespread recognition that a healthy folate status is important for proper CNS development, the rescue mechanism remains unclear. Our results seem to represent both scenarios, providing a new tool for consideration.

First, considering the PCP results, we seem to see a folate-resistant phenotype that is in congruence with mouse models containing similar mutations[14] and clinical craniorachischisis[19]. Where, perhaps unsurprisingly, if you take a symbolic sledgehammer to the highly conserved cytoskeletal machinery present during mammalian neural tube development by knocking out a key PCP protein, you quickly reach the critical threshold and cause irreversible developmental failure[20]. In this context, the ability of mouse models to correctly recapitulate failure with regional fidelity to human *in vitro* and clinical cases becomes understandable, and their utility to study relatively rare, uniformly lethal, neurulation failures in the context of human disease is preserved[14]. Yet, future experiments utilizing platforms like the Rosette Array could provide divergence from mouse models by investigating the risk potential of more subtle changes to the

cytoskeletal machinery, like the SCRIB^{P1043L} mutation that has been linked in human patients to an increased risk of developing isolated caudal spina bifida[21], a scenario nearly impossible to reproduce in mice. Therefore, the effect the mutation has on lumbar identifying arrays, multifactorial risk scenarios utilizing folate (MTX) and non-folate (Rock inhibition) antagonists, and folate supplementation response should be investigated. Once such example from our preliminary results demonstrate that the P1043L$^{(-/-)}$ clone was slightly more disrupted than the WA09 control, but not the MTHFR$^{C677T(-/-)}$ mutant, in a folate stressed environment, exhibiting the interesting multifactorial investigations now made feasible by such a qHTS platform. Still, this once again encounters the seemingly fundamental NTD question of our time, why do folate-sensitive defects form, and furthermore, is the discordant presentation between humans (both clinically and modeled) and mice obscuring further investigative efforts.

As the immense dynamic complexities of the spatiotemporal gene expression landscape present during neurodevelopment have been realized during the epigenetic revolution[22], the folate pathway's direct link to critical epigenetic regulatory mechanisms have been noted[23], including its impact on DNA methylation[24] and related epigenetic markers. While the total impact of methylation and/or other epigenetic mechanisms on the cellular, molecular, and genetic mechanisms of neural tube formation remains unclear, it introduces another variable to consider when tallying the critical threshold of NTD formation. Thus, when considering the regionally distinct transcriptional programs present within the developing CNS[7,8], and the fact that over half of all human genes differ from mouse orthologs in their temporal trajectories during neurodevelopment[25], one must realize that further investigation of factors that have known global effects on this transcriptional landscape require control for human specific regulation. Only then

can meaningful conclusions be drawn about a risk factor's metabolic, genetic, and/or epigenetic effects on human neural development.

Herein lies the true potential of utilizing a human-based platform like the Rosette Array for further investigative studies. The transcriptional regulatory networks present during neural differentiation and development are activated[26], in a reproducible manner, by the ability to control hPSCs' innate capacity to spontaneously form biomimetic CNS tissues. Excitingly, observed disruption of these networks at the earliest stage of rosette formation has already been shown to have important downstream consequences related to clinical neurodevelopmental disease[13]. As such, future experiments that further characterize the demonstrated folate-sensitive phenotypes, shown both between Rosette Array CNS regions, and *MTHFR* mutant and isogenic control cell lines, should utilize toolsets[27] that are able to discern influences these experimental variables have on these regulatory networks. When done in conjunction with experiments that investigate the utility of patient-derived iPSC lines for capturing the impact of the genetic and epigenetic variation *within* the human population, it is my personal belief that we will one day refer to NTD formation scenarios not as "folate" sensitive, but *epigenetically* sensitive or resistant, signaling a more comprehensive approach to our understanding of disease presentation and prevention.

As a final note, this discussion does of course not capture the full translational potential the development of the Rosette Array platform achieves, however that is largely demonstrated by the venture of Neurosetta LLC into the realm of neurotoxicology screening and its collaborations with a broader community of neurodevelopmental disease modeling. With certainty, the ability to reproducibly simulate and characterize the formation mechanisms of the early human CNS will have widespread implications for the study of neurodevelopment and related disease.

Bibliography

1. Wallingford, J. B., Niswander, L. A., Shaw, G. M. & Finnell, R. H. The Continuing Challenge of Understanding, Preventing, and Treating Neural Tube Defects. *Science* **339**, (2013).

2. Mirabella, A. C., Foster, B. M. & Bartke, T. Chromatin deregulation in disease. *Chromosoma* **125**, 75–93 (2016).

3. Iskandar, B. J. & Finnell, R. H. Spina Bifida. *New England Journal of Medicine* **387**, 444–450 (2022).

4. Harris, M. J. & Juriloff, D. M. An update to the list of mouse mutants with neural tube closure defects and advances toward a complete genetic perspective of neural tube closure. *Birth Defects Research Part A: Clinical and Molecular Teratology* **88**, 653–669 (2010).

5. Shum, AlisaS. W. & Copp, AndrewJ. Regional differences in morphogenesis of the neuroepithelium suggest multiple mechanisms of spinal neurulation in the mouse. *Anat Embryol* **194**, (1996).

6. Juriloff, D. M. & Harris, M. J. Insights into the Etiology of Mammalian Neural Tube Closure Defects from Developmental, Genetic and Evolutionary Studies. *Journal of Developmental Biology* **6**, 22 (2018).

7. Osseward, P. J. *et al.* Conserved genetic signatures parcellate cardinal spinal neuron classes into local and projection subsets. *Science* **372**, 385–393 (2021).

8. Iyer, N. R. *et al.* Modular derivation of diverse, regionally discrete human posterior CNS neurons enables discovery of transcriptomic patterns. *Sci. Adv.* **8**, eabn7430 (2022).

9. Lippmann, E. S. *et al.* Deterministic HOX Patterning in Human Pluripotent Stem Cell-Derived Neuroectoderm. *Stem Cell Reports* **4**, 632–644 (2015).

10. Knight, G. T. , **Lundin, B. F.,** *et al.* Engineering induction of singular neural rosette emergence within hPSC-derived tissues. *eLife* **7**, e37549 (2018).

11. Xue, X. *et al.* A Patterned Human Neural Tube Model Using Microfluidic Gradients. *Nature* (2024) doi:10.1038/s41586-024-07204-7.

12. Eiraku, M. *et al.* Self-Organized Formation of Polarized Cortical Tissues from ESCs and Its Active Manipulation by Extrinsic Signals. *Cell Stem Cell* **3**, 519–532 (2008).

13. Birtele, M. *et al.* Non-synaptic function of the autism spectrum disorder-associated gene SYNGAP1 in cortical neurogenesis. *Nat Neurosci* **26**, 2090–2103 (2023).

14. Lesko, A. C., Keller, R., Chen, P. & Sutherland, A. Scribble mutation disrupts convergent extension and apical constriction during mammalian neural tube closure. *Developmental Biology* (2021) doi:10.1016/j.ydbio.2021.05.013.

15. Tabatabaei, R. S. *et al.* Association of Fetal MTHFR C677T Polymorphism with Susceptibility to Neural Tube Defects: A Systematic Review and Update Meta-Analysis. *Fetal Pediatr Pathol* 1–17 (2020) doi:10.1080/15513815.2020.1775734.

16. Skalko, R. G. & Gold, M. P. Teratogenicity of methotrexate in mice. *Teratology* **9**, 159–163 (1974).

17. Zhao, J. *et al.* Influence of the antifolate drug Methotrexate on the development of murine neural tube defects and genomic instability. *J Appl Toxicol* **33**, 915–923 (2013).

18. Blom, H. J., Shaw, G. M., den Heijer, M. & Finnell, R. H. Neural tube defects and folate: case far from closed. *Nature Reviews Neuroscience* **7**, 724–731 (2006).

19. Robinson, A. *et al.* Mutations in the planar cell polarity genes CELSR1 and SCRIB are associated with the severe neural tube defect craniorachischisis. *Hum Mutat* **33**, 440–447 (2012).

20. Juriloff, D. M. & Harris, M. J. A consideration of the evidence that genetic defects in planar cell polarity contribute to the etiology of human neural tube defects. *Birth Defects Research Part A: Clinical and Molecular Teratology* **94**, 824–840 (2012).

21. Lei, Y. *et al.* Mutations in Planar Cell Polarity Gene SCRIB Are Associated with Spina Bifida. *PLoS One* **8**, (2013).

22. Roth, T. L. Epigenetics of neurobiology and behavior during development and adulthood. *Dev Psychobiol* **54**, 590–597 (2012).

23. Meethal, S. V., Hogan, K. J., Mayanil, C. S. & Iskandar, B. J. Folate and epigenetic mechanisms in neural tube development and defects. *Childs Nerv Syst* **29**, 1427–1433 (2013).

24. Imbard, A., Benoist, J.-F. & Blom, H. J. Neural Tube Defects, Folic Acid and Methylation. *International Journal of Environmental Research and Public Health* **10**, 4352–4389 (2013).

25. Cardoso-Moreira, M. *et al.* Developmental Gene Expression Differences between Humans and Mammalian Models. *Cell Reports* **33**, 108308 (2020).

26. Xie, W. *et al.* Epigenomic Analysis of Multilineage Differentiation of Human Embryonic Stem Cells. *Cell* **153**, 1134–1148 (2013).

27. Siahpirani, A. F. *et al.* Dynamic regulatory module networks for inference of cell type–specific transcriptional networks. *Genome Res.* **32**, 1367–1384 (2022).

Appendix A: KEY RESOURCES TABLE

REAGENT or RESOURCE	SOURCE	IDENTIFIER
Antibodies		
SCRIB primary	Invitrogen	(Thermo Fisher Scientific Cat# PA5-54821, RRID:AB_2647030)
N-cadherin primary	BD Biosciences	(BD Biosciences Cat# 610920, RRID:AB_2077527)
Pax6 primary	BioLegend	(BioLegend Cat# 901301 (also 901302), RRID:AB_2565003)
β-tubulin primary	Biolegend	(Cat# 802001, RRID:AB_2564645
Brachyury primary	R&D	Cat# AF2085, RRID:AB_2200235
Sox2 primary	Millipore	Cat# MAB4423, RRID:AB_11213224
Donkey anti-Rabbit IgG 488	Invitrogen	(Thermo Fisher Scientific Cat# A-21206 (also A21206), RRID:AB_2535792)
Donkey anti-Mouse IgG 488	Invitrogen	(Thermo Fisher Scientific Cat# A-21202, RRID:AB_141607)
555 Donkey anti-Rabbit	Invitrogen	(Thermo Fisher Scientific Cat# A-31572 (also A31572), RRID:AB_162543)
Donkey anti-Mouse IgG 555	Invitrogen	(Thermo Fisher Scientific Cat# A-31570, RRID:AB_2536180)
horseradish peroxidase-conjugated goat anti-rabbit	Jackson ImmunoResearch Laboratories	(Jackson ImmunoResearch Labs Cat# 111-035-003, RRID:AB_2313567)
Chemicals, Peptides, and Recombinant Proteins		
ROCK Inhibitor (Y27632)	Tocris	Cat#: 1254
FGF8b	PeproTech	Cat#: 100-25
CHIR99021	Tocris	Cat#: 4423
GDF11	PeproTech	Catalog Number:120-11
Dorsomorphin	Tocris	Cat#: 3093/10
Retinoic Acid	Sigma-Aldrich	Cat#: R2625
Penicillin-Streptomycin	Invitrogen	Cat#: 15140122
TRIzol	Invitrogen	Cat#: 15596026
Triton X-100	Sigma-Aldrich	Cat#:A16046.AE
DAPI	Invitrogen	Cat#: D1306
Alexa Fluor 488 Phalloidin	Invitrogen	Cat#: A12379

ω-mercaptoundecyl bromoizobutyrate	ProChimia	Cat#: FT 015-m11-0.2
PEGMEMA	Sigma-Aldrich	Cat#: 447935
sodium ascorbate	Sigma-Aldrich	Cat#: 1613509
2,2'-Bipyridine	Sigma-Aldrich	Cat#: D216305
Copper (II) Bromide	Sigma-Aldrich	Cat#: 221775
human S9 liver fraction	Sigma-Aldrich	Cat#: S2442
CloneR	StemCell Technologies	Cat#: 05889
TrueCut Cas9 Protein V2	Thermo Fisher Scientific	Cat#: A36498
QuickExtract DNA Extraction Solution 1.0	Thermo-Fisher	Cat#: NC9904870
protease inhibitors	Thermo-Fisher	Cat#: 78429
Glycolic Acid	Sigma-Aldrich	Cat#: 124737
Benomyl	Sigma-Aldrich	Cat#: 45339
Valproic Acid Sodium Salt	Sigma-Aldrich	Cat#: P4543
Methotrexate	Sigma-Aldrich	Cat#: 1414003
Novobiocin	Sigma-Aldrich	Cat#: N6160
Dabigatran	Sigma-Aldrich	Cat#: SML2351
Acetaminophen	Sigma-Aldrich	Cat#: A7085
Acetochlor	Sigma-Aldrich	Cat#: 33379
Pymetrozine	Sigma-Aldrich	Cat#: 46119
Clodinafop	Sigma-Aldrich	Cat#: 31676
Fenoxycarb	Sigma-Aldrich	Cat#: 34343
Thalidomide	Sigma-Aldrich	Cat#: T151
Butyl benzyl pthalate	Sigma-Aldrich	Cat#: 36927
Heptadecafluorooctane-sulfonic acid	Sigma-Aldrich	Cat#: 77282
Methyl mercury	Sigma-Aldrich	Cat#: 442534
Verapamil	Sigma-Aldrich	Cat#: V4629
Carbamazepine	Sigma-Aldrich	Cat#: C4024
Propiconazole	Sigma-Aldrich	Cat#: 45642
Abamectin	Sigma-Aldrich	Cat#: 31732
Benzylcetyldimethyl Ammonium Chloride	Sigma-Aldrich	Cat#: B4136
Spirodiclofen	Sigma-Aldrich	Cat#: 33654
Thiram	Sigma-Aldrich	Cat#: 45689

Triadimefon	Sigma-Aldrich	Cat#: 45693
Epoxiconazole	Sigma-Aldrich	Cat#: 36848
Desmedipham	Sigma-Aldrich	Cat#: 45426
Fenhexamid	Sigma-Aldrich	Cat#: 31713
Cyproconazole	Sigma-Aldrich	Cat#: 46068
Chlorpyrifos	Sigma-Aldrich	Cat#: 45395
Propyzamide	Sigma-Aldrich	Cat#: 45645
Thiacloprid	Sigma-Aldrich	Cat#: 37905
Aspirin	Sigma-Aldrich	Cat#: A2093
Permethrin	Sigma-Aldrich	Cat#: 45614
Rotenone	Sigma-Aldrich	Cat#: 45656
5-methyltetrahydrofolic acid, disodium salt	Sigma-Aldrich	Cat#: M0132
Dolutegravir	Sigma-Aldrich	Cat#: 10313
Critical Commercial Assays		
RPS18 Taqman Gene Expression Assay	Thermo-Fisher	Cat#Hs01375212_g1
SuperScript IV First-Strand Synthesis System	Invitrogen	Cat#: 18091050
Neon™ Transfection System	Invitrogen	Cat#: MPK10096
Zymoclean Gel DNA Recovery Kit	Zymo Research	Cat#: D4007/D4008
DC Protein Assay	Bio-rad	Cat#: 5000111
Experimental Models: Cell Lines		
WA09 hESC line (parent of all edited lines)	WiCell	(RRID:CVCL_9773)
Oligonucleotides		
HoxA1 Taqman Gene Expression Assay	Thermo-Fisher	Cat#Hs00939046_m1
HoxA5 Taqman Gene Expression Assay	Thermo-Fisher	Cat#Hs00430330_m1
HoxC6 Taqman Gene Expression Assay	Thermo-Fisher	Cat#Hs00171690_m1
HoxC8 Taqman Gene Expression Assay	Thermo-Fisher	Cat#Hs00224073_m1
HoxC9 Taqman Gene Expression Assay	Thermo-Fisher	Cat#Hs00396786_m1

HoxD10 Taqman Gene Expression Assay	Thermo-Fisher	Cat#Hs00157974_m1
All SCRIB Taqman Gene Expression Assay	Thermo-Fisher	Cat#Hs00363005_m1
SCRIB Iso A Taqman Gene Expression Assay	Thermo-Fisher	Cat#Hs01034954_g1
SCRIB Iso B Taqman Gene Expression Assay	Thermo-Fisher	Cat#Hs01040361_g1
Software and Algorithms		
CellProfiler	Harvard	v4.2.6
GraphPadPrism	GraphPad Prism	v10.2.1
Nikon NIS-Elements (Acquisition)	Nikon	v5.42.01
Nikon NIS-Elements AR (Analysis)	Nikon	v5.02.00
RosetteDetect™	Neurosetta LLC	v0.1.0.0
Other		
CryoMed controlled rate freezer	Thermo Fisher Scientific	Cat#: TSCM17PA
Prolong Gold Antifade Reagent	Invitrogen	Cat#: P36930
Nikon A1R confocal microscope	Nikon	n/a
4–20% Mini-PROTEAN® TGX™ Precast Gel	Bio-rad	Cat#: 4561094